

PROBING THE METAL OXIDE LOCAL ENVIRONMENT FOR THERMOCHROMIC AND
PHOTOVOLTAIC APPLICATIONS

Taylor Hennessey Moot

A dissertation submitted to the faculty at the University of North Carolina at Chapel
Hill in partial fulfillment of the requirements for the degree of Doctor of Philosophy in the
Department of Chemistry.

Chapel Hill
2017

Approved by:

James F. Cahoon

Thomas J. Meyer

Gerald J. Meyer

Scott Warren

Yosuke Kanai

© 2017
Taylor Hennessey Moot
ALL RIGHTS RESERVED

ABSTRACT

Taylor Hennessey Moot: Probing the Metal Oxide Local Environment for Thermo-chromic and Photovoltaic Applications
(Under the direction of James F. Cahoon)

Energy demand is predicted to increase by 28% between 2015 and 2040, placing strain on the current reserves of petroleum, coal and natural gas. There are two different approaches to alleviating the demand on Earth's natural resources: increase energy efficiency or utilize renewable resources. Vanadium dioxide (VO_2) thermo-chromic windows passively modulate infrared (IR) transparency, aiding in reducing undesirable heat exchange from outside to indoors. This occurs through a semiconductor to metal transition upon heating which is coupled with an optical change from IR transparent to IR absorbing, respectively. The metallic phase exhibits a plasmon resonance and we can control the local environment by embedding the VO_2 nanoparticles in a high refractive index material (i.e. a polymer) where the plasmon absorption intensity increases as does the overall device performance.

Alternatively, to increase the production of renewable energy, p-type dye sensitized solar cells (DSSCs) are studied as a precursor to tandem devices for solar fuel production. A novel p-type semiconductor (photocathode), lead titanate was identified through a material informatics approach and utilized in fundamental studies of the semiconductor-electrolyte interaction. By tuning the electrolyte composition to increase the concentration of an efficient electron scavenger, I_2 , the photocurrent and fill factor approximately doubled resulting in a four-fold increase in power conversion efficiency. Simply changing the concentration of I_2 , and electron

scavenger, in the electrolyte allows for more efficient charge separation at the semiconductor-chromophore-electrolyte interface, which improves two of the most problematic device performance metrics in p-type DSSCs, low photocurrent and low fill factor.

ACKNOWLEDGEMENTS

Thank you to my friends and family for always being supportive. Special thanks to my advisor Jim Cahoon for the funding and allowing me to explore new research areas. Thanks to Rene Lopez for helping me along the way in all capacities, and thanks to all of my other unofficial mentors for the support. A huge thank you to all of my collaborations, the UNC EFRC and my group members for all of the scientific support. Finally, a shout out to MRS for all of the great experiences and free meals.

TABLE OF CONTENTS

| | |
|--|-----|
| LIST OF FIGURES..... | ix |
| LIST OF TABLES..... | xi |
| LIST OF EQUATIONS..... | xii |
| LIST OF SYMBOLS AND ABBREVIATIONS..... | xiv |
| Chapter 1: INTRODUCTION..... | 1 |
| 1.1 Energy Demand and Sustainability..... | 1 |
| 1.2 Thermochromic Windows..... | 2 |
| 1.3 Photovoltaic Devices and Parameters..... | 5 |
| 1.4 p-Type Dye Sensitized Solar Cells..... | 10 |
| Chapter 2: METHODS..... | 16 |
| 2.1 General Analytical Characterization Techniques..... | 16 |
| 2.2 Vanadium Dioxide Nanoparticle Synthesis..... | 17 |
| 2.3 Thermochromic Window Fabrication..... | 17 |
| 2.4 Thermochromic Window Infrared Modulation Analysis..... | 18 |
| 2.5 Mie Scattering Simulations..... | 18 |
| 2.6 Lead Titanate Synthesis and Paste Preparation..... | 19 |
| 2.7 Nickel Oxide Paste Preparation..... | 19 |
| 2.8 Fabrication of Dye Sensitized Solar Cell..... | 19 |
| 2.9 Photovoltaic Characterization..... | 20 |
| 2.10 Incident Photon to Current Conversion Efficiency..... | 20 |
| 2.11 Electrochemical Impedance Spectroscopy..... | 21 |
| 2.12 Semiconductor Electrochemical Analytical Methods..... | 21 |
| 2.13 Density Functional Theory..... | 22 |

| | | |
|---|--|-----|
| 2.14 | Material Fingerprints and Similarity Search..... | 23 |
| Chapter 3: DESIGNING PLASMON-ENHANCED THERMOCHROMIC FILMS USING A VANADIUM DIOXIDE NANOPARTICLE ELASTOMERIC COMPOSITE..... | | |
| 3.1 | Introduction..... | 25 |
| 3.2 | Experimental..... | 27 |
| 3.3 | Results and Discussion..... | 27 |
| 3.4 | Conclusions..... | 37 |
| 3.5 | Acknowledgements..... | 38 |
| Chapter 4: PROBING THE VALENCE BAND DENSITY OF STATES OF NIO: UNDERSTANDING THE IMPACT OF DEFECT STATES ON TRANSPORT, CHARGE INJECTION AND RECOMBINATION..... | | |
| 4.1 | Introduction..... | 39 |
| 4.2 | Experimental..... | 41 |
| 4.3 | Results and Discussion..... | 41 |
| 4.4 | Conclusions..... | 56 |
| 4.5 | Acknowledgements..... | 57 |
| Chapter 5: MATERIAL INFORMATICS DRIVEN DESIGN AND EXPERIMENTAL VALIDATION OF LEAD TITANATE AS AN AQUEOUS SOLAR PHOTOCATHODE..... | | |
| 5.1 | Introduction..... | 58 |
| 5.2 | Experimental..... | 60 |
| 5.3 | Results and Discussion..... | 61 |
| 5.4 | Conclusions..... | 84 |
| 5.5 | Acknowledgements..... | 85 |
| Chapter 6: THE BENEFICIAL ROLE OF IODINE ON INTERFACE RECOMBINATION IN P-TYPE DYE SENSITIZED SOLAR CELLS AND ITS IMPLICATIONS FOR AQUEOUS ELECTROLYTES..... | | |
| 6.1 | Introduction..... | 87 |
| 6.2 | Experimental..... | 89 |
| 6.3 | Results and Discussion..... | 89 |
| 6.4 | Conclusions..... | 102 |

| | |
|-----------------------------|-----|
| 6.5 Acknowledgements..... | 102 |
| Chapter 7: CONCLUSIONS..... | 104 |
| APPENDIX..... | 106 |
| REFERENCES..... | 109 |

LIST OF FIGURES

| | |
|--|----|
| Figure 1.1. Thermochromic windows..... | 4 |
| Figure 1.2. Photoelectrochemical device designs..... | 6 |
| Figure 1.3. Standard current-voltage (<i>J-V</i>) curve with denoted performance metrics | 8 |
| Figure 3.1. Optical simulation data of PDMS embedded with spherical VO ₂ nanoparticles ranging in diameter from 10 nm to 200 nm..... | 29 |
| Figure 3.2. Characterization of VO ₂ nanoparticles..... | 31 |
| Figure 3.3. Optical properties of representative films..... | 32 |
| Figure 3.4. Performance values for films varying in thickness from ~15 to ~75 μm..... | 34 |
| Figure 3.5. Effect of elastomeric properties of the film on thermochromic performance..... | 35 |
| Figure 4.1. NiO V _{fb} measured by Mott-Schottky as compared to DOS map..... | 43 |
| Figure 4.2. Change in 450-NiO bandgap with applied bias..... | 44 |
| Figure 4.3. Percent of total current arising from faradaic current for 450-NiO..... | 44 |
| Figure 4.4. Characterization of NiO..... | 45 |
| Figure 4.5. XPS of NiO..... | 47 |
| Figure 4.6. Identification of the trap state character..... | 48 |
| Figure 4.7. NiO DOS and DSSC performance analysis..... | 54 |
| Figure 5.1. General knowledge-driven workflow..... | 62 |
| Figure 5.2. Construction of materials fingerprints from the band structure (B-fingerprints)..... | 63 |
| Figure 5.3. Assessment of similarity between NiO, PbTiO ₃ and SrTiO ₃ | 64 |
| Figure 5.4. Characterization of porous PbTiO ₃ films..... | 67 |
| Figure 5.5. Profilometry of PbTiO ₃ films..... | 68 |
| Figure 5.6. Absorbance spectra of PbTiO ₃ films dye-loaded with the chromophore P1 | 68 |
| Figure 5.7. Photovoltaic characteristics of PbTiO ₃ in water/acetonitrile solutions..... | 70 |
| Figure 5.8. P1 chromophore desorption..... | 72 |
| Figure 5.9. Average performance <i>J-V</i> curves of PbTiO ₃ devices..... | 73 |
| Figure 5.10. Representative <i>J-V</i> curve hysteresis for 100% PbTiO ₃ devices..... | 73 |
| Figure 5.11. Cyclic voltammetry of the acetonitrile and water electrolyte solutions..... | 74 |
| Figure 5.12. Percent of ideal fill factor..... | 75 |

| | |
|---|-----|
| Figure 5.13. Photoresponse of dye-loaded PbTiO ₃ films and devices..... | 76 |
| Figure 5.14. Photovoltaic characteristic of PbTiO ₃ in 100% water without any chromophore... | 77 |
| Figure 5.15. Photoactive species analysis for water electrolyte solutions with 1.0 M LiI and with 0.01 M I ₂ , 0.10 M I ₂ , and 0.50 M I ₂ | 78 |
| Figure 5.16. Absorbed photon to current efficiency (APCE) spectra..... | 78 |
| Figure 5.17. Mott-Schottky analysis of PbTiO ₃ with various solvents..... | 79 |
| Figure 5.18. Analysis of the PbTiO ₃ DSSC performance..... | 81 |
| Figure 5.19. Electrochemical impedance spectroscopy (EIS) measurements of DSSC devices at V _{OC} under 1-sun illumination..... | 82 |
| Figure 6.1. Average p-DSSC <i>J-V</i> curves of PbTiO ₃ | 90 |
| Figure 6.2. PbTiO ₃ p-DSSC performance mechanism..... | 93 |
| Figure 6.3. Average PbTiO ₃ p-DSSCs fabricated without any chromophore | 94 |
| Figure 6.4. Average p-DSSC <i>J-V</i> curves of NiO and TAD Al NiO..... | 96 |
| Figure 6.5. IPCE and device resistance of NiO and TAD Al NiO..... | 99 |
| Figure 6.6. Average NiO and TAD Al NiO p-DSSCs fabricated without any chromophore.... | 100 |

LIST OF TABLES

| | |
|---|----|
| Table 1.1. Iodine based electrolyte redox couples in acetonitrile..... | 14 |
| Table 5.1. Average and champion ^a photovoltaic characteristics for different electrolyte water percentages..... | 71 |
| Table 5.2. Average and champion ^a dark curve characteristics for different electrolyte water percentages..... | 71 |
| Table 5.3. Current density values calculated from incident photon to current efficiency spectra..... | 77 |
| Table 5.4. Electrochemical impedance spectroscopy extracted parameters using a simplified Randles model..... | 83 |
| Table 5.5. Beta values calculated from differential resistance values versus applied bias..... | 83 |
| Table 6.1. Electrolyte compositions..... | 90 |
| Table 6.1. Average PbTiO ₃ p-DSSC device performance metrics..... | 91 |
| Table 6.2. Average NiO p-DSSC device performance metrics..... | 97 |
| Table 6.3. Average TAD Al NiO p-DSSC device performance metrics..... | 98 |

LIST OF EQUATIONS

| | |
|---|----|
| Equation 1.1. Experimental fill factor..... | 9 |
| Equation 1.2. Power conversion efficiency..... | 9 |
| Equation 1.3. Ideal diode equation..... | 9 |
| Equation 1.4. Effect of R_s on ideal diode equation..... | 10 |
| Equation 1.5. Effect of R_{sh} on ideal diode equation..... | 10 |
| Equation 1.6. Ideal fill factor..... | 10 |
| Equation 1.7. Effect of R_s on fill factor..... | 10 |
| Equation 1.8. Effect of R_{sh} on fill factor..... | 10 |
| Equation 1.9. Iodine electrolyte reaction..... | 14 |
| Equation 1.10. I_3^- one electron reaction..... | 14 |
| Equation 1.11. I_2 one electron reaction..... | 14 |
| Equation 1.12. I_3^- two electron reaction..... | 14 |
| Equation 1.13. I_2 two electron reaction..... | 14 |
| Equation 1.14. I_2^- one electron reaction..... | 14 |
| Equation 1.15. I_3^- two electron reaction.... | 14 |
| Equation 1.16. I^- one electron reaction... .. | 14 |
| Equation 2.1. Mott Schottky flatband potential..... | 21 |
| Equation 2.2 Conductance..... | 22 |
| Equation 2.3. Tanimoto similarity..... | 24 |
| Equation 3.1. Theoretical transmittance spectra | 28 |
| Equation 3.2. Visible transmittance figure of merit..... | 28 |
| Equation 3.3. IR modulation figure of merit..... | 28 |
| Equation 3.4. Visible transmittance affected by stretching | 36 |
| Equation 4.1. Density of states..... | 42 |
| Equation 4.2. Nickel hydroxide/oxyhydroxide redox couple..... | 46 |
| Equation 4.3. Conduction via defect to band hopping..... | 51 |
| Equation 4.4. Conduction via defect hopping..... | 51 |

| | |
|--|----|
| Equation 5.1. Device recombination differential resistance..... | 84 |
| Equation 6.1. Effect of R_s on fill factor..... | 94 |

LIST OF SYBMOLS AND ABBREVIATIONS

| | |
|------------------------|---|
| A | Amps |
| A_r | Area |
| AFLOW | Automatic FLOW |
| ALD | Atomic Layer Deposition |
| APCE | Absorbed Photon to Current Efficiency |
| C | Capacitance |
| °C | Degrees Celsius |
| CBE | Conduction Band Edge |
| CCA | Chromophore Catalyst Assembly |
| chrom. | Chromophore |
| C.F.O. | Cohen, Fritzsche and Oshinsky |
| cm | Centimeter |
| cp | Centipoise |
| d | Decrease in Film Thickness |
| DFT | Density Functional Theory |
| DOS | Density of States |
| DSC | Differential Scanning Calorimetry |
| DSPEC | Dye Sensitized Photoelectrosynthesis Cell |
| DSSC | Dye Sensitized Solar Cell |
| EDS | Energy Dispersive X-Ray Spectroscopy |
| E_b | Band Edge Energy |
| E_f | Fermi level |
| E_{gap} | Bandgap Energy |

| | |
|-------------------------------------|--|
| EIA | Energy Information Administration |
| EIS | Electrochemical Impedance Spectroscopy |
| Eq. | Equation |
| eV | Electron Volts |
| F | Farads |
| FF | Fill Factor |
| FF_{max} | Maximum Theoretical Fill Factor |
| FF_s | Fill Factor (as affected by series resistance) |
| FF_{sh} | Fill Factor (as affected by shunt resistance) |
| FTO | Fluorine Doped Tin Oxide |
| g | Gram |
| G | Conductance |
| GGA | Generalized Gradient Approximation |
| GuSCN | Guanidinium Thiocyanate |
| hr | Hour |
| Hz | Hertz |
| [I₂]_{eq} | Equilibrium I ₂ Concentration |
| I | Current |
| I_{sc} | Short Circuit Current |
| ICSD | Inorganic Crystal Structure Database |
| IDA | Interdigitated Array Electrode |
| IPCE | Incident Photon to Current Efficiency |
| IR | Infrared |
| J | Current Density |
| J_L | Light Generated Current Density |

| | |
|------------------------|---|
| J₀ | Dark Saturation Current Density |
| J_{sc} | Short Circuit Current Density |
| J-V | Current Density-Voltage |
| K | Kelvin |
| k_b | Boltzmann's Constant |
| K_{eq} | Equilibrium Constant |
| L | Film Thickness |
| M | Molar |
| M_o | Monoclinic |
| mA | Milliamps |
| mL | Milliliter |
| mM | Millimolar |
| MO_x | Metal Oxide |
| mS | Millisiemens |
| mV | Millivolt |
| N | Number (of nanoparticles per unit volume) |
| n | Ideality Factor |
| η | Power Conversion Efficiency |
| N_D | Doping Level |
| n-DSSC | n-Type Dye Sensitized Solar Cell |
| NHE | Normal Hydrogen Electrode |
| NIR | Near Infrared |
| N_{max} | Maximum Number (of particles per unit volume) |
| nm | Nanometer |

| | |
|------------------------|--|
| n_o | Number (of devices in a set) |
| P | Porosity |
| P_{max} | Maximum Power Point |
| P_{in} | Input Power |
| p-DSSC | p-Type Dye Sensitized Solar Cell |
| PAW | Projector-Augmented Wavefunction |
| PBE | Perdew-Burke-Ernzerhof |
| PCE | Power Conversion Efficiency |
| PDMS | Polydimethylsiloxane |
| PEC | Photoelectrochemical |
| q | Elemental Charge |
| Q_{ext} | Extinction efficiency |
| R | Rutile |
| r | Radius of Nanoparticle |
| R₀ | Pre-exponential term related to dark saturation resistance |
| R_{CT} | Charge Transfer Resistance |
| R_{rec} | Recombination Differential Resistance |
| r_s | Normalized Series Resistance |
| R_s | Series Resistance |
| R_{is} | Interfacial Series Resistance |
| r_{sh} | Normalized Shunt Resistance |
| R_{sh} | Shunt Resistance |
| S | Siemens |
| s | Seconds |

| | |
|--|---|
| SECU | Secondary Electron Cutoff |
| SEM | Scanning Electron Microscope |
| STEM | Scanning Transmission Electron Microscope |
| SMT | Semiconductor to Metal Transition |
| ΔT | IR Modulation |
| %T | Transmittance |
| T | Temperature |
| TA | Transient Absorbance |
| TAD | Targeted atomic deposition |
| T_c | Tanimoto Coefficient |
| T_{cr} | Critical Temperature |
| TCO | Transparent Conducting Oxide |
| TEM | Transmission Electron Microscope |
| TGA | Thermogravimetric Analysis |
| T_M | Transmittance figure of merit in the monoclinic phase |
| T_M^{IR} | IR transmittance figure of merit in the monoclinic phase |
| T_R | Transmittance figure of merit in the rutile phase |
| T_R^{IR} | IR transmittance figure of merit in the rutile phase |
| T_{vis} | Visible transmittance figure of merit |
| T_{vis}^{Stretch} | Visible transmittance figure of merit for stretched films |
| UPS | Ultraviolet Photoelectron Spectroscopy |
| U.S. | United States of America |
| UV | Ultraviolet |
| V | Voltage |

| | |
|--------------------------|--|
| V_{app} | Applied Bias |
| VBE | Valence Band Edge |
| VEG | Vanadyl Ethylene Glycolate |
| V_{fb} | Flatband Potential |
| V_{oc} | Open Circuit Potential |
| vol | Volume |
| Vis | Visible |
| w | Weight Percent |
| wt. | Weight |
| ΔW_{h,db} | Defect to Band Hopping Barrier |
| ΔW_{h,d} | Defect Only Hopping Barrier |
| XC | Exchange Correlation |
| XPS | X-Ray Photoelectron Spectroscopy |
| XRD | X-Ray Diffraction |
| φ | AM1.5G solar irradiance |
| β | Beta |
| σ_b | Bulk Conductivity |
| σ | Conductance |
| ° | Degree |
| Δ | Delta, change in |
| ε | Dielectric Constant |
| ε₀ | Permittivity of Free Space |
| ε_R | Dielectric Constant of the Semiconductor |
| μm | Micron |

| | |
|-----------|------------|
| Ω | Ohms |
| θ | Theta |
| λ | Wavelength |

Chapter 1: INTRODUCTION

1.1 Energy Demand and Sustainability

The U.S. Energy Information Administration (EIA) predicts that world energy consumption will increase 28% between 2015 and 2040.¹ Non-renewable energy sources (petroleum, coal and natural gas) make up the vast majority of energy currently produced, but the percentage of renewable energy created is predicted to increase by an average of 2.8% per year to a predicted 31% of total energy production by 2040.^{1,2} In the United States (U.S.), 36% of generated electricity comes from renewable sources (solar, nuclear, hydropower, wind and geothermal) where nuclear accounts for the majority of renewable electricity at 63%.² Solar energy makes up 2% of electricity generated from renewable sources and only a mere 0.9% of electricity generated overall. However, in the U.S. over 66% of electricity is wasted and accounts for the majority of all energy rejected as compared to residential, commercial, industrial and transportation.²

This increase in energy consumption coupled with significant energy waste places a strain on non-renewable sources of energy such as petroleum, coal and natural gas. Finite resources of petroleum, coal and natural gas have consequential ramifications for energy supply security and foreign energy dependency.³ To combat the depleting energy resources and bolster national security there must be significant change in the current energy production sources and usage. There are two separate but complementary methods to combat an increase in energy demand: increase the efficiency of energy usage and to create energy from renewable sources.

1.2 Thermochromic Windows

In the U.S. a total of 66% of all energy is unused, wasted through various mechanisms, such as electricity transport through the grid or through heat losses.² Minimizing the wasted energy through more efficient processes or technologies is equivalent to increasing the overall amount of energy generated. Buildings are a major contributor to the overall growth in world energy usage, where building energy consumption is projected to increase by 32% between 2015 and 2040.² The residential sector is a useful market to focus on because of the trend towards more energy efficient building materials and the regular construction of new houses allows for quick incorporation of new energy efficient technologies. In U.S. homes, 48% of energy consumption occurs through indoor heating and cooling and it is estimated that as much as one third of heat loss occurs through windows and doors.⁴ This accounts for 46% of all energy losses in the residential sector, thus creating energy efficient windows would drastically improve the energy efficiency of the residential sector.

There are a wide variety of energy efficient windows currently for sale and being researched. The commercially available energy efficient windows can be broken down into two categories: re-designed window structures or window coatings.^{5,6} To redesign the window structure, companies have added more glass panes or included a high resistance to heat flow gas between the panes to minimize heat losses. Various types of coating technologies are also available, such as heat absorbing tints, low-emissivity coatings, reflective coatings and spectrally selective coatings and all minimize the amount of sunlight via different mechanisms.^{5,6}

These window technologies are only useful for keeping a house cool instead of warm, limiting their year round use and relevance in cold climates. Ideally, a window would be 'smart' and self-regulate the heat transferred into the house depending on the external temperature. For

example, if it was hot out, the windows would minimize heat transferred indoors, whereas when it was cold heat transfer would be maximized. To this end, electrochromic window technologies, among others, have been developed.⁷ Electrochromic windows are based on materials which, under an applied bias, change their optical properties. Nickel oxide (NiO) and tungsten oxide (WO₃) are common electrochromic window metal oxide semiconductors, where upon application of a negative applied bias the black material turns white, likely due to Li⁺ intercalation.⁷⁻⁹

However, electrochromic windows require an energy input and can be difficult to retro-fit onto currently installed windows, minimizing their practical applications. Thermochromic windows change optical properties upon a change in temperature, making them a better window design than electrochromic windows because no input is necessary to modulate the heat transfer based on fluctuations in the external temperature. The most promising material for thermochromic windows is a metal oxide, vanadium dioxide (VO₂). Vanadium dioxide has a semiconductor to metal transition (SMT) at 68 °C coupled with an optical transition.^{10,11} Specifically, at room temperature the semiconductor monoclinic (M_o) phase is infrared (IR) transparent, whereas the high temperature metal rutile (R) phase is IR opaque. This modulates the heat transfer into the building based on the outside temperature.¹¹ This change in IR opacity upon a temperature change makes VO₂ an ideal material for smart window applications.

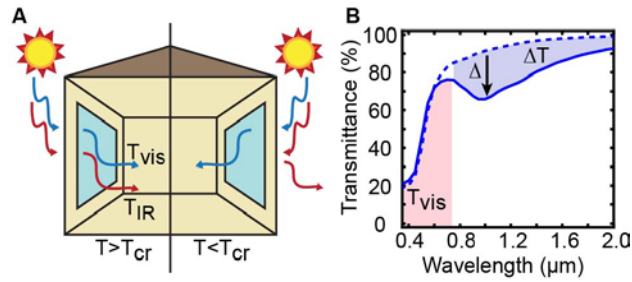


Figure 1.1. Thermochromic windows. **A)** Schematic of an ideal thermochromic window, where (left) at cool temperatures below the critical temperature (T_{cr}) of the semiconductor to metal transition (SMT), $T > T_{cr}$ allows all visible light (T_{vis}) and all IR light (T_{IR}) in. Right, at warm temperatures ($T < T_{cr}$), all IR light is reflected. **B)** Schematic of the performance parameters for thermochromic windows where T_{vis} (red shaded) is the percent of visible light transmitted and the change in IR transmittance (ΔT) from cool (dashed line) to warm (solid line) temperatures upon heating (Δ).

To realize a VO_2 based thermochromic smart window there are three main problems to overcome. First, a SMT of $68\text{ }^\circ\text{C}$ is too high for most commercial residential applications, and ideally should be $\sim 25\text{ }^\circ\text{C}$. To this end significant work has been spent studying the effect of various dopants (W, Mg, Mo, etc.) on tuning the SMT, where W doping can tune the SMT to $35\text{ }^\circ\text{C}$.^{10–13} Second, the orange tint of VO_2 , which originates from a d-d transition, must be minimized for aesthetic purposes.¹¹ Various dopants tune the visible absorption profile, such as Mg, and the addition of antireflection coatings have been used to minimize the orange tint.^{14–16} Finally, the IR modulation must be increased. The majority of research into VO_2 smart windows has investigated how to increase the visible transmittance (T_{vis}) while simultaneously increasing the IR modulation (ΔT). Typically thin films of VO_2 have been used and by simply increasing the film thickness, the ΔT increases. However, this method decreases the T_{vis} such that the T_{vis} is less than 50% at high ΔT values. To this end, various methods of optical tuning have been tried, such as antireflective coatings, increased scattering through nanoparticle size modulation or highly reflective hierarchical microstructures.^{17–32}

In **Chapter 3** a method to develop high efficiency and easily processable VO₂ nanoparticle based thermochromic smart windows is proposed. Exploiting the high temperature VO₂ (R) metallic character allows for the IR absorption profile to be tuned through specific, wavelength dependent interactions between light and the nanoparticles free electrons, creating a highly absorbing plasmon resonance. By using the sensitivity of the plasmon absorption profile to the nanoparticle shape and local environment, we calculate the highest performance to date is possible simply through synthesizing small nanoparticles (>30 nm) and using a high refractive index polymer matrix.

1.3 Photovoltaic Devices and Parameters

To increase the amount of sustainable energy produced, more renewable sources must be used in high efficiency devices. The sun offers limitless energy to be captured and converted into energy, where photovoltaic devices are often the device of choice to absorb and convert sunlight to usable electricity. There are many different types of photovoltaics, but they can be generalized into two different categories, solid state devices and photoelectrochemical (PEC) devices. Solid state devices are made exclusively of solid materials whereas PEC devices add a liquid electrolyte to the solid state structure. Solid state multijunction devices, with concentrators have produced the highest efficiencies to date, at 46.0%, or 37.9% without concentrators.³³ Silicon and cadmium selenide solid state photovoltaics, among others, are currently commercialized.

However, PEC devices offer some unique advantages over solid state devices, namely the ability to do catalysis.³⁴⁻³⁶ A prime example of the strengths of PEC devices is the dye sensitized photoelectrosynthesis cell (DSPEC). The DSPEC harnesses sunlight which is then used to convert water and carbon dioxide to oxygen and formate or methane, i.e. solar fuels, which can then be isolated for used similarly to natural gas or petroleum.³⁵ The proposed DSPEC design

utilizes many different components to achieve the production of solar fuels, as shown in **Figure 1.2 A**. Specifically, a chromophore creates photoexcited charges, where on the oxidation side the hole is transferred to a catalyst to oxidize water and the electron is injected into a transparent, wide bandgap n-type semiconductor (photoanode). The resulting protons are used on the reduction side to be used in the catalytic cycle, where the photoexcited chromophore transfers electrons to the carbon dioxide (CO₂) reduction catalyst and the hole is injected into a transparent, wide bandgap p-type semiconductor (photocathode).³⁵

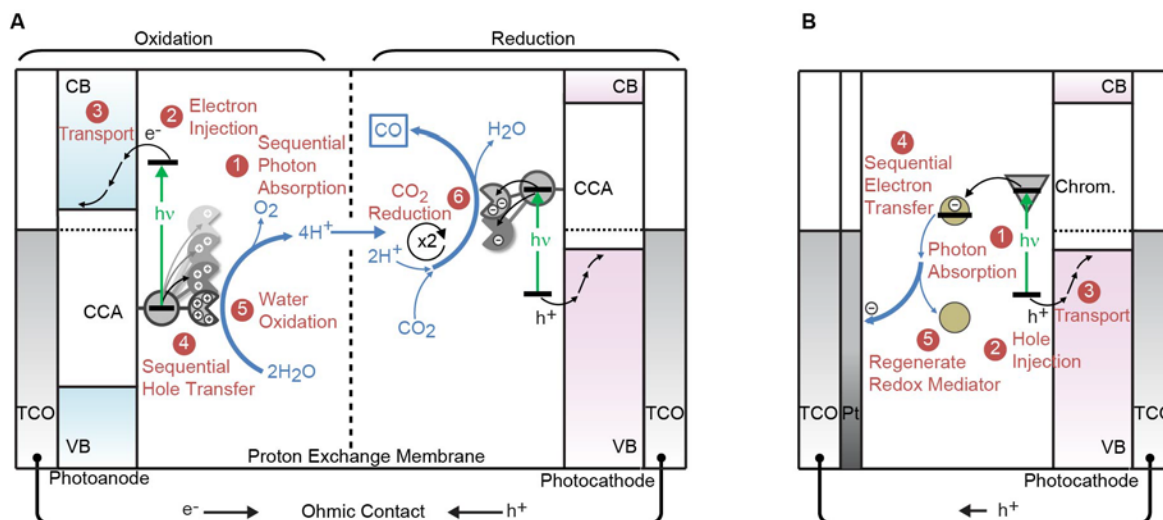


Figure 1.2. Photoelectrochemical device designs. **A**) DSPEC consisting of an n-type semiconductor (photoanode) and a p-type semiconductor (photocathode) in series with the denoted valence band (VB), conduction band (CB) and Fermi level (dashed line) with a chromophore-catalyst assembly (CCA) bonded to the semiconductor surface. Finally, the transparent conducting oxide (TCO) connects the circuit. **B**) A p-type dye sensitized solar cell where instead of a CCA there is simply a chromophore (chrom.) and a platinum (Pt) counter electrode replaces the photoanode. In each device the numbers denote the steps in the functioning of the device.

The success of the DSPEC device performance is based on the performance of each individual component, making it an extremely complicated device to realize but can be very efficient once every component works succinctly in concert. To understand the fundamental

chemistry and physics behind the performance of each component in the DSPEC in detail, the dye-sensitized-solar cell (DSSC) is a useful model system namely because it is a much simpler device design which allows for each component to be isolated and studied. Additionally, studying the DSPEC through two DSSCs, a p-type and an n-type in tandem, allows for optimization of individual components to be pursued in parallel. The oxidation side and the n-DSSC has been studied extensively, leading to improvements in photoanode, chromophore and catalysis design which have translated to efficient water oxidation. However, there has been significantly less work on the reduction side, and consequently it is the limiting factor to achieving high performance or even creating solar fuels. Thus, the thrust of this thesis is to improve efficiency of the reduction side through understanding the performance of the p-DSSC.

The DSSC consists of a wide bandgap semiconductor (working electrode) which is either a photocathode (p-type DSSC) or a photoanode (n-type DSSC) loaded with a chromophore and placed in a liquid electrolyte solution with a counter electrode, typically made up of platinum, to complete the circuit.³⁷⁻⁴⁰ The DSSC device (**Figure 1.2 B**) function is similar to that of a DSPEC (**Figure 1.2 A**). Briefly, the photoexcited chromophore creates an excited state where the hole is first injected into a photocathode material and then the electron reduces the iodide/triiodide electrolyte, which is ultimately regenerated at the counter electrode. To measure the performance of the DSSC, current voltage (J - V) curves are used.

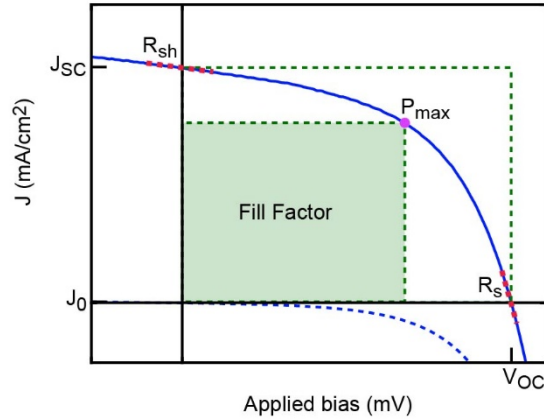


Figure 1.3. Standard current-voltage (J - V) curve with denoted performance metrics. The J - V curve under one sun illumination (solid blue) and in the dark (dashed blue) have seven different relevant parameters, short circuit current (J_{SC}), open circuit voltage (V_{OC}), dark saturation current (J_0), shunt resistance (R_{sh}), series resistance (R_s), and fill factor which is the ratio of the area of a rectangle intersecting the J_{SC} and V_{OC} (green dashed) and a maximum size rectangle that fits underneath the J - V curve (green dashed and shaded) with the maximum power point (P_{max} , purple dot).

Typically, device performance is measured through a J - V curve in the dark and under stimulated one sun illumination. From the J - V curve there are 7 key parameters that can be used to parametrize performance, as shown in **Figure 1.3**. The short circuit current density (J_{SC}) and the open circuit voltage (V_{OC}) are where the J - V curve (solid blue) intersects with the y-axis and the x-axis, respectively and the dark saturation current density (J_0) is where the dark curve (dashed blue) intersects with the y-axis. The J_{SC} is typically related to the absorption profile and extinction coefficient, and loading of the chromophore, although it can be affected by significant recombination within the semiconductor, or at the semiconductor electrolyte interface.³⁸ The open circuit voltage is the voltage difference between the Fermi level of the semiconductor and the Nernst potential of the electrolyte, and is also negatively affected by recombination.³⁸ The J_0 arises from current occurring through various recombination pathways that do not require illumination to activate, and ideally is minimized.³⁸ The fill factor (FF) is the ratio of the area of

a rectangle intersecting the J_{SC} and V_{OC} (green dashed) and a maximum size rectangle that fits underneath the J-V curve (green dashed and shaded), which represents the maximum power point (P_{max}) and is calculated by:

$$FF = \frac{P_{max}}{V_{OC}J_{SC}} \quad (1.1)$$

The fill factor is impacted by all recombination metrics that occur in the semiconductor and at the semiconductor electrolyte interface, allowing it to be a relative measure of overall recombination. To achieve a high efficiency device the fill factor, J_{SC} and V_{OC} all must be maximized, where the power conversion efficiency (PCE) (η) is calculated by:

$$\eta = \frac{V_{OC}J_{SC}FF}{P_{in}} \quad (1.2)$$

where I_{SC} is the short circuit current, which is J_{SC} multiplied by the active area of the photovoltaic and P_{in} is the input power.

In an ideal photovoltaic the J-V curve can be modeled through the ideal diode equation:

$$J = J_0 \left[\exp\left(\frac{qV}{nk_bT}\right) - 1 \right] - J_L \quad (1.3)$$

where J_L is the light generated current density, q is the elemental charge, V is voltage, n is the ideality factor, k_b is the Boltzmann constant and T is temperature. However, in reality the photovoltaic performance deviates from ideal behavior through either alternate charge transport pathways or through high resistances. The shunt resistance (R_{sh}) and the series resistance (R_s) are denoted with red dashed lines and are the values of the inverse of the slopes of the J-V curve intersects with the y axis and the x axis, respectively. The shunt resistance is the resistance to charge transport through various alternate pathways and should be maximized in an ideal device.

The series resistance is the resistance of all components (working electrode, electrolyte, counter electrode) in series and should be minimized in an ideal device. To understand how these resistances affect the device performance, they can be modeled by modified ideal diode equations:

$$J = J_L - J_0 \left[\exp \left(\frac{q(V+IR_s)}{nk_bT} \right) \right] \quad (1.4)$$

$$J = J_L - J_0 \exp \left(\frac{qV}{nk_bT} \right) - \frac{V}{R_{sh}} \quad (1.5)$$

The series and shunt resistances can minimize the photocurrent but as well as affect the fill factor. In general, the maximum theoretical fill factor (FF_{max}) is dictated by the V_{OC} :

$$FF_{max} = \frac{V_{OC} - \ln(V_{OC} + 0.72)}{V_{OC} + 1} \quad (1.6)$$

The effects of the shunt resistance and series resistance on fill factor are as follows:

$$FF_s = FF_{max} (1 - 1.1r_s) + \frac{r_s^2}{5.4} \quad (1.7)$$

$$FF_{sh} = FF_{max} \left(1 - \frac{V_{OC} + 0.7}{V_{OC}} \frac{FF_{max}}{r_{sh}} \right) \quad (1.8)$$

Where r_s and r_{sh} are the normalized series and shunt resistances, respectively which are equal to the given resistance divided by the characteristic resistance of the photovoltaic device.

These set of parameters and the ideal diode equation, its derivations or resulting empirical formulas help understand the specific cause to any deviation from ideality in device performance.

1.4 p-Type Dye Sensitized Solar Cells

The first reported mesoporous DSSC was by Gratzel and O'Regan in 1991 using a titanium dioxide (TiO_2) photoanode and a ruthenium(II)tris(bipyridine) (RuBPY) chromophore.⁴¹ Currently, the record PCE is over 14% due to intensive research efforts into novel chromophores and electrolyte designs. In 1999 the first p-type DSSC was reported, using a nickel oxide (NiO) as the photocathode with a laser dye, erythrosine B and the same iodide/triiodide electrolyte.⁴² Since that first report, significant research efforts have been spent on understanding and re-designing the chromophore and the photocathode, and recently there has been some effort to redesign the electrolyte.⁴³⁻⁴⁹ However, the standard and champion devices achieve a PCE an order of magnitude lower than that of the n-DSSCs and are plagued with low photocurrents and low fill factors.^{46,50-52} To understand the factors limiting device performance it is imperative to understand the three main components of the p-DSSC: the photoanode, the chromophore and the electrolyte.

NiO is the standard photocathode material used in p-DSSCs. It is a wide bandgap semiconductor; however all typical preparation methods result in a black material, indicative of large amounts of trap states and/or impurities.^{53,54} Significant research efforts have been spent understanding the identity, magnitude of the trap states and their effect on device performance. Current literature suggests that the trap states are some combination of Ni^{3+} , Ni vacancy and Ni^0 and those are causing the dark color of NiO, either through $\text{Ni}^{2+}/\text{Ni}^{3+}$ charge transfer or through the innate dark color of Ni^0 .⁵³⁻⁵⁵ The most remarkably device characteristic of NiO DSSCs is the low fill factor, which is on average ~35%. The low fill factor occurs from a low shunt resistance, indicative of significant recombination pathways, likely between the semiconductor and the chromophore.⁵² Despite this, NiO p-DSSCs have achieved the highest PCE.⁴⁶ Further detailed

discussion of the trap state identity, magnitude and effect on device performance can be found in **Chapter 4**.

To minimize the trap states and their detrimental impact on performance, various modification and passivation techniques have been used to treat NiO. Doping NiO by lithium or cobalt have shown small improvements in performance, namely by improving the open circuit voltage.⁵⁵⁻⁵⁷ Surface modification and passivation techniques include an aluminum oxide atomic layer deposition (ALD) layer, high temperature annealing and a modified ALD surface passivation called targeted atomic deposition (TAD).^{54,58} These methods have all shown improvements in either the short circuit current or the V_{OC} but have shown minimal improvements in the fill factor.

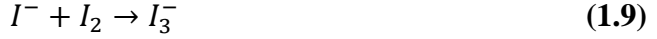
Other research efforts focus on replacing NiO, but the parameter constraints on the new potential photocathode materials are such that there are not many obvious candidates. The semiconductor must be wide bandgap with the valence band edge above 1 V vs Ag/AgCl to have efficient injection from the most oxidative chromophore, P1.^{40,43} Currently, the delafossite class of semiconductors have been investigated as a replacement photocathode for NiO based upon the expected higher hole mobility that arises from the partially metal character valence band edge.⁵⁹ To this end, delafossites have been investigated with a few standout materials, such as $CuBO_2$, $CuGaO_2$, $CuAlO_2$, which have shown high fill factors and high open circuit voltages.^{44,47-49} A novel approach to identifying an alternate photocathode material, and experimental validation is discussed in **Chapter 5**.

The absorption profile of the chromophore directly dictates the resulting photocurrent and consequently substantial research efforts have been spent on designing novel chromophores with broad absorption profiles and/or high extinction coefficients. Organic chromophores based off of

triphenylamine, perylene, squarene, and porphyrin units have been developed.⁶⁰ More recently, donor-acceptor chromophores have been designed for p-DSSCs in attempts to increase hole lifetime by physically separating the electron and hole onto the acceptor and donor, respectively. To this end, various chromophore base groups have been studied and the length and identity between the donor and acceptor has been modified.^{43,61,62} Based on this model one most commonly used chromophore, P1 was designed. P1 reached photocurrent values of 1.52 mA/cm² and incident photon to current efficiency (IPCE) values of 18%.⁴³ Additionally, the photocurrent record of 7.4 mA/cm² was achieved by the chromophore BH4 which has a similar extended structure to that of P1.⁴⁵ Despite the major improvements, the fill factors achieved in these devices are still low, indicating that there are major recombination pathways that are not affected by the hole lifetime.

There is little research into the electrolyte specifically for p-DSSCs, where the majority of discussion occurs around the photocurrent contribution of the electrolyte. It was determined that I₃⁻ can efficiently inject into NiO p-DSSCs and has been shown in other materials as well.^{39,63} Although this increases the photocurrent and therefore the overall PCE, it is an unwanted side reaction and in the ideal case all photocurrent is created exclusively from the chromophore. The recent record for p-DSSCs was achieved using the iron based electrolyte, where the increase in performance was driven by the improvement in the V_{OC} from 243 mV to 645 mV based on the change in the Nernst potential of the electrolyte.⁴⁶ To understand the role of the typical iodide/triiodide electrolyte used in p-DSSCs, the literature from the n-DSSC field will be reviewed.

The iodide/triiodide electrolyte is created through mixing a cation iodine salt (XI) and I₂, where the cation is typically Li, in a solvent, usually acetonitrile. The equilibrium constant for:



is $5 \times 10^6 \text{ M}^{-1}$ in acetonitrile which results in a solution that has the below 7 redox couples, in addition to the cation.⁶⁴

Table 1.1. Iodine based electrolyte redox couples in acetonitrile.⁶⁴

| Eq. | Reaction | Redox Couple | Potential (V vs NHE) |
|-------------|---------------------------------------|---------------|----------------------|
| 1.10 | $I_3^- + e^- \rightarrow I_2^- + I^-$ | I_3^-/I_2^- | -0.64 |
| 1.11 | $I_2 + e^- \rightarrow I_2^-$ | I_2/I_2^- | -0.34 |
| 1.12 | $I_3^- + 2e^- \rightarrow 3I^-$ | I_3^-/I^- | -0.19 |
| 1.13 | $I_2 + 2e^- \rightarrow 2I^-$ | I_2/I^- | -0.07 |
| 1.14 | $I_2^- + e^- \rightarrow 2I^-$ | I_2^-/I^- | 0.36 |
| 1.15 | $3I_2 + 2e^- \rightarrow 2I_3^-$ | I_2/I_3^- | 0.46 |
| 1.16 | $I + e^- \rightarrow I^-$ | I/I^- | 0.75 |

First, the cation in solution (Li, Mg, H, etc.) affects the band edge position by creating a dipole at the surface of the semiconductor.⁶⁵ This has been studied extensively and, by modulating the band edge position, affects the V_{OC} , and even the J_{SC} thus can significantly affect the overall PCE.⁶⁶ The Nernst potential is set by the 2 electron reaction between the electrolyte and the platinum counter electrode, and in p-DSSCs is the I_3^-/I^- redox couple (**Equation 1.12**). All of the other redox couples can affect device performance through recombination pathways between the semiconductor or chromophore and the electrolyte or through chromophore regeneration, however little research has investigated this area in p-DSSCs. In n-DSSCs, I^- aids in chromophore regeneration and either I_3^- or I_2 acts as an electron scavenger and causes recombination between the chromophore and the electrolyte.^{67,68} The specific effect of the additives is still being debated, but it is known that the guanidinium thiocyanate both shifts the band edge and minimizes interaction between I_2 and the chromophore.^{69,70} Based on the extensive amount of literature on the effect of the electrolyte on n-DSSC performance, it is

imperative that the effect of the electrolyte on p-DSSC performance is equally well understood and is investigated in **Chapter 6**.

There is no clear picture on how to achieve high performance p-DSSCs that can rival n-DSSC performance and this limits the ability for tandem devices, such as the DSPEC to be realized. There are questions into how to design a high performance photocathode, what is and how does the electrolyte affect device performance. To understand these questions, we focus on investigating the semiconductor and electrolyte in reference to the interface and how it affects recombination.

Chapter 2: METHODS

2.1 General Analytical Characterization Techniques

Powder x-ray diffraction (XRD) was carried out on a Rigaku Multiflex X-Ray Diffractometer with Cu source, typically using a scan rate of $2^\circ 2\theta/\text{min}$, unless otherwise specified. Differential scanning calorimetry (DSC) was done using a TA Instruments DSC Q200, where the data was taken using a ramp of $5^\circ\text{C}/\text{min}$ and cool $10^\circ\text{C}/\text{min}$ from 0 - 100°C in a zero hermetic aluminum pan. Thermogravimetric analysis (TGA) was done from room temperature to 550°C in air, using a TA instruments Q5000. Film thicknesses were measured by a Bruker DektakXT profilometer. Scanning electron microscopy (SEM) images were taken using a Hitachi S-4700 Cold Cathode Field Emission Scanning Electron. Transmission electron microscopy (TEM) and scanning TEM (STEM) images were obtained with an FEI Tecnai Osiris operating at 200 kV with a sub-nanometer probe and equipped with a Super-X EDS system. This system was used to acquire drift-corrected energy dispersive x-ray spectroscopy (EDS) elemental maps of metal oxide (MO_x) particles using the Bruker Esprit software, and standardless Cliff-Lorimer analysis was performed on the deconvoluted EDS spectra for elemental quantification. Absorption, transmittance and reflectance spectra were taken in a Cary 5000 UV-Vis-NIR from Agilent with integrating sphere attachment, or for solution absorbance a Hewlett-Packard UV-Vis-NIR absorption spectrometer HP 8453 was used. The fluorescence of chromophore loaded MO_x was compared to chromophore loaded glass slide as a standard using a 532 nm laser coupled to a Nikon D-Eclipse C1 SI microscope with a CCD detector. Raman spectroscopy on the MO_x was obtained using a 488 nm excitation source from an Ar+ laser in the Renishaw

inVia confocal Raman microscope. X-ray photoelectron spectroscopy (XPS) was collected using a Kratos Axis Ultra DLD spectrometer. All XPS data was corrected to the C 1s peak and background corrected. The Kratos Axis Ultra DLD spectrometer also has ultraviolet photoelectron spectroscopy capability (UPS) and all UPS data was collected from samples of the MO_x on fluorine doped tin oxide (FTO) substrates. Conductivity measurements were taken using a Keithley semiconductor characterization system 4200-SCS four point probe with the Keithley interactive test environment version 7.2 software modified with a TE Tech peltier stage for high temperature measurements. All MO_x samples were made on 1 cm² glass substrates. All microscale optical pictures were taken using a Nikon D-Eclipse C1 si darkfield microscope (100 x zoom) and all macroscale pictures were taken using either a Nikon DSLR camera or an iPhone 5c.

2.2 Vanadium Dioxide Nanoparticle Synthesis

Nanoparticle synthesis was adopted and modified slightly.⁷¹ Briefly 0.5 g ammonium metavanadate (Fisher Scientific) was added to 10 mL ethylene glycol (Fisher Scientific) at 160 °C and heated with vigorous stirring for 2 hours. The dark purple vanadyl ethylene glycol (VEG) precipitate was collected by vacuum filtration and washed with ethylene glycol. Two drying steps of 30 minutes at 250 °C in a petri dish followed with additional wash and rinse in between. The resulting dark blue VO₂ (M₀) powder was collected.

2.3 Thermochromic Window Fabrication

0.012 g of the VO₂ was added to a 0.79 wt. % solution of PDMS (Sylgard 184, Dow Corning) in heptane with 7.7 wt. % curing agent. The solution was sonicated for 1 hour and then left to settle for 4 days until the solution changed from a dark blue/grey opaque solution to an

orange/brown transparent solution. 50 μl -200 μl (in 25 μl steps) of resulting solution was dropcast onto 1.5 cm x 1.5 cm glass slides. After 12 hours of drying, the films were transferred dried in an oven at 150 $^{\circ}\text{C}$ for an additional 12 hr. Upon removal the films were entirely dry and cured. To make pure PDMS films, the PDMS was peeled off the glass substrate using a razor blade.

2.4 Thermochromic Window Infrared Modulation Analysis

Optical properties of each film were measured in a Cary 5000 UV– vis– NIR from Agilent with integrating sphere attachment. Data was normalized against a glass standard to reduce effect of background spectra on the curvature of experimental data. High temperature data was collected using a homebuilt heating stage with a TE Tech peltier stage that was attached to the UV-vis-NIR. Data was taken at room temperature (25 $^{\circ}\text{C}$) and above the SMT temperature, 75-80 $^{\circ}\text{C}$.

2.5 Mie Scattering Simulations

Extinction efficiency values for spherical VO_2 (M_0) and VO_2 (R) nanoparticles ranging in diameter from 10 nm to 200 nm in a PDMS matrix (refractive index=1.4) were obtained using Mie Theory Calculator program with previously reported optical data.^{72,73} Introduction of air pockets was simulated by a 2.5 nm – 20 nm thick shell of air around a VO_2 90 nm particle, all embedded in a PDMS matrix. The resulting extinction efficiency values were used to calculate transmittance spectra for VO_2 (M_0) and VO_2 (R) at 40 Lw values ranging from 0.0005-0.15. These transmittance curves were used to calculate visible transmittance and IR modulation figures of merit at each Lw value, for each particle size.

2.6 Lead Titanate Synthesis and Paste Preparation

All reagents were purchased from Fisher Scientific and used without further purification unless noted otherwise. In an inert, dry atmosphere lead acetate anhydrous (0.075 g) was combined with glacial acetic acid (2 mL). Then, titanium isopropoxide (0.05 mL) was combined with anhydrous ethanol (8 mL). The two solutions were combined and the resulting sol was capped and removed from the glove box. To create structured films, 10 wt. % ethyl cellulose (22 cp) was added to the precursor sol solution. A drop of the sol gel solution was wiped across a FTO glass substrate. To make thin films, 5 layers of the sol solution were spun onto FTO glass substrate, with a 1 minute 150 °C heat treatment between each layer. All films were then annealed in air for 70 minutes at 600 °C then cooled to room temperature.

2.7 Nickel Oxide Paste Preparation

NiO nanoparticles were bought commercially from Inframat Advanced Materials and then mixed with ethyl cellulose, ethanol and terpineol which was then homogenized by horn sonication, mechanical dispersion and ball milling as reported in literature.⁷⁴ TAD treatment was done using Aluminum ALD as discussed in literature. For all experiments 5 cycles were used, except for where specified.⁵⁴

2.8 Fabrication of Dye Sensitized Solar Cell

Fluorine doped tin oxide (FTO) glass substrates ($12-14 \Omega/\text{cm}^2$) purchased from Hartford glass (TEC15) and cleaned with typical organic solvents and sonication. MO_x was deposited on the FTO as noted in **Methods section 2.6 and 2.7** Processed films were submerged in a 0.5 mM P1 (Dynamo) in acetonitrile solution for 20 minutes. Pt counter electrodes were fabricated by

drop-casting H_2PtCl_6 in isopropanol solution onto an FTO glass slide, which included a powder-blasted pinhole, and annealing for 30 minutes at 380 °C. The DSSC was fabricated by sandwiching a 20 μm Surlyn polymer gasket (Solaronix) between the working dyed MO_x electrode and the Pt counter electrode using a custom-built heating apparatus. Electrolyte solutions were prepared by mixing 1.0M LiI and 0.1M I_2 in acetonitrile, unless otherwise noted. The devices were backfilled with electrolyte using a custom-built vacuum chamber. The pinhole was sealed with a microscope coverslip and additional Surlyn polymer.

2.9 Photovoltaic Characterization

DSSC performance was investigated using a Newport Oriel 150W class ABB solar simulator with an AM1.5G filter. The light intensity was calibrated to 1-sun using a certified reference solar cell (Newport 91150 Vs), which was calibrated in June, 2011. A Keithley 2636A SourceMeter was used for all electrical measurements. All photovoltaic performance measurements were done in air at room temperature with a step size of +1 mV in the increasing forward bias direction (except where explicitly stated otherwise in **Figure 5.10**) and a 0.1 second delay. Average values and standard deviations for DSSC photovoltaic device metrics represent measurements on n separate devices, as noted. The active area of each device was equivalent to the size of the gaskets used to hold the liquid electrolyte; thus, no aperture or mask was used during illumination.

2.10 Incident Photon to Current Conversion Efficiency

Incident photon-to-current efficiency (IPCE) measurements were obtained by illuminating devices with a Newport Instruments tungsten lamp coupled to a Princeton Instruments SP-2300 spectrometer with 1200 g/mm grating.

2.11 Electrochemical Impedance Spectroscopy

Gamry Reference 600 electrochemical impedance spectrometer. Data was collected on DSSCs under 1-sun illumination at an applied bias using 1-sun illumination, and the resulting curves were fit to a simplified Randles circuit using the Gamry Software.

2.12 Semiconductor Electrochemical Analytical Methods

All techniques utilized a standard three electrode cell configuration that consists of a MO_x working electrode, a Pt mesh counter electrode and an Ag/AgCl reference electrode in a 0.1 M LiClO_4 acetonitrile solution. Any deviation from this setup will be noted.

To obtain Mott Schottky data, spectra were taken at a given frequency (Hz) in the standard electrolyte solution with varying water percentages using a Gamry Reference 600 electrochemical impedance spectrometer. The large linear portion of $1/C^2$ was fit with a linear function, where the x -intercept was determined to be the V_{fb} , and the slope was converted to doping level as follows from the equation:

$$\frac{1}{C^2} = \frac{2}{\epsilon_0 \epsilon_R A^2 q N_D} \left(V - V_{fb} - \frac{k_B T}{q} \right). \quad (2.1)$$

Cyclic voltammetry (CV) curves were obtained either on a Pine WaveNow Potentiostat (solution) with a glassy carbon working electrode or a Gamry Reference 600 electrochemical impedance spectrometer (MO_x) using a scan rate of 20 mV/s, unless otherwise noted. Applied bias conductance measurements were taken on a CH instruments 760E bi-potentiostat. Here, the working electrode is a platinum interdigitated array electrode (IDA) obtained from CH

instruments with NiO spincast on it. Silver paste was used to connect the IDA electrode to copper wires to collect the current from IDA electrode 1 (I_1) and from IDA electrode 2 (I_2). A small applied bias of 5 mV was applied between the IDA electrodes while the potential was swept from -1 to 2 V vs Ag/AgCl at a scan rate of 20 mV/s using linear sweep voltammetry. The conductance (G) was calculated by:

$$G = (I_1 - I_2)/(2 * bias) \quad (2.2)$$

To obtain photocurrent values in a three electrode setup, chronoamperometry was done using a Gamry Reference 600 electrochemical impedance spectrometer. The MO_x working electrode was loaded with chromophore for ~20 minutes and then held at a given bias for 2-4 minutes while being manually cycled between being under 1-sun illumination, or in the dark by blocking the incident beam. The photocurrent values were obtained by calculating the difference between the resulting photocurrent values in the dark and upon one sun illumination. Spectroelectrochemistry of the NiO film was performed in the standard three electrode cell using a 0.1 M tetrabutylammonium hexafluorophosphate acetonitrile electrolyte which was degassed with N_2 for 30 min before experimentation. Spectral changes of NiO under bias applied by a CHI 601D potentiostat were monitored with an Agilent HP 8453 UV-Visible Spectrophotometer after 20 min polarization time for each potential step.

2.13 Density Functional Theory

Collaborators Lesheng Li and Yosuke Kanai ran the first-principles calculations, which closely follow the computational details previously reported.⁷⁵ Density functional theory (DFT) calculations were performed with the Hubbard correction using the Quantum Espresso code.⁷⁶ The interaction of the valence electrons with ionic cores was described by Vanderbilt ultrasoft

pseudopotentials, and the Kohn–Sham wave functions were represented in a planewave basis set, where the energy cutoffs of the wave functions and the density were 48 and 300 Ry, respectively.⁷⁷ The Brillouin zone integration was performed with a $4 \times 4 \times 4$ Monkhorst–Pack k-point grid. Spin-polarized calculations were carried out in this present work because of the antiferromagnetic nature of NiO.⁷⁸ In our calculations, the Hubbard U correction approach was applied to the generalized-gradient approximation (GGA) of Perdew, Burke, and Ernzerhof (PBE), because of the strong electron correlation of the partially filled *d*-shells in Ni atoms.^{79–83} The Hubbard parameter *U* and exchange parameter *J* are not considered separately, but they are combined as an effective parameter U_{eff} ($U_{eff} = U - J$).⁸⁴ The value of U_{eff} was set to 5.4 eV, as in previous works.^{54,75,85–89} To simulate the NiO structure, a 64-atom supercell was used, modeling the ideal bulk NiO. The Ni vacancy and OH[−]/H₂O-doping structures were modeled using this bulk NiO structure by removing or substituting one nickel atom with an OH[−]/H₂O group.

2.14 Material Fingerprints and Similarity Search

Collaborators Olexandr Isayev and Alexander Tropsha encoded the electronic structure diagram for each material as band structure fingerprints as previously reported.⁹⁰ Along every special *k*-point along the wave-vector, the energy diagram was discretized into 32 bins serving as our fingerprint array. It is worth emphasizing that each of the 14 different Bravais lattices has a unique set of *k*-points. The comparison of a set of *k*-points belonging to a single Bravais lattice type will be considered a symmetry-dependent band structure fingerprint. To name a few examples, the Brillouin zone path of a Cubic Lattice (Γ –*X*–*M*– Γ –*R*–*X*|*M*–*R*) will be encoded with just four points (*Γ*, *M*, *R*, *X*) giving rise to a fingerprint array of length 128. Body-centered orthorhombic lattice is much more complex (Γ –*X*–*L*–*T*–*W*–*R*–*X*₁–*Z*– Γ –*Y*–*S*–*W*|*L*₁–*Y*|*Y*₁–*Z*) and represented by 13 points (Γ , *L*, *L*₁, *L*₂, *R*, *S*, *T*, *W*, *X*, *X*₁, *Y*, *Y*₁, *Z*) or fingerprint array of length

416. Conversely, the comparison of identical k -points not specifically belonging to any Bravais lattice is always possible when considering the Γ point as it is common to all lattice types. In present work, we limited our models only to the Γ point of the band structure fingerprint.

Among many chemical similarity metrics used in cheminformatics, Tanimoto similarity coefficient, T_c , between chemicals A and B is the most widely used.⁹¹ It is calculated as shown in eq. 2

$$T_c = \frac{\sum_{j=1}^n x_{jA} x_{jB}}{\left(\sum_{j=1}^n (x_{jA})^2 + \sum_{j=1}^n (x_{jB})^2 - \sum_{j=1}^n x_{jA} x_{jB}\right)} \quad (2.3)$$

where x_j is the value of the j^{th} descriptor and n is the total number of descriptors. Tanimoto similarities range from 0.0 (no similarity between chemicals A and B) to 1.0 (A and B are identical). The known p-type photocathodes NiO, Co₃O₄, Cu₂O, CuI, CuAlO₂, CuGaO₂, NiCo₂O₄, and ZnCo₂O₄ were used as reference query materials.

The band structure data was extracted for 46,936 materials from the AFLOWLIB repository, which represents approximately 60% of known stoichiometric inorganic materials listed in the Inorganic Crystal Structure Database (ICSD).^{92,93} All referenced DFT calculations were performed with the generalized gradient approximation (GGA) PBE exchange-correlation (XC) functional and projector-augmented wavefunction (PAW) potential according to the AFLOW standard for high-throughput computing.⁹⁴ This standard ensures reproducibility of the data, as well as provides visibility and reasoning for any parameter set used in calculations, such as accuracy thresholds, calculation pathways, and mesh dimensions.

Chapter 3: DESIGNING PLASMON-ENHANCED THERMOCHROMIC FILMS USING A VANADIUM DIOXIDE NANOPARTICLE ELASTOMERIC COMPOSITE

Reprinted with permission from Moot, T.; Palin, C.; Mitran, S.; Cahoon, F. J.; Lopez, R; *Adv. Opt. Mater*, **2016**, (4), 578-583. Copyright Wiley 2016

3.1. Introduction

Approximately 40% of worldwide energy consumption is used to heat and cool interior climates.⁹⁵ Much of this energy usage is wasted through windows, placing an unnecessary strain on an energy supply that will need to increase 56% by 2040.⁹⁶ In order to mitigate losses through windows, an efficient thermochromic ‘smart’ window that passively reduces heat exchange by altering its infrared opacity based on temperature is needed. To-date, the most promising material for this application is vanadium dioxide (VO₂), a well-known thermochromic material whose key properties were discovered in 1959.⁹⁷ VO₂ passively switches from an infrared-transparent semiconductor monoclinic (M₀) phase to an infrared-opaque metal rutile (R) phase when heated above 68 °C.^{11,98} This semiconductor-to-metal transition (SMT), with its coupled change in optical properties, allows VO₂ to facilitate heating at low temperatures with VO₂ (M₀) and minimize radiative heating at high temperatures with VO₂ (R). Until recently, most studies on the thermochromic properties of this material have been focused on pure VO₂ thin films, which have reached top performance values of 47.2% visible transmittance and 15.1% infrared (IR) modulation with the use of an anti-reflective overcoating.^{16,17,23,24,99} The main drawback of thin films is that in order to reach a reasonable IR modulation a sufficiently thick film must be used, and the necessary thickness results in low visible transmittance. Additionally, VO₂ thin-film

fabrication usually requires high annealing temperatures and does not lend itself well to manufacturing on the industrial scale or to retrofitting of existing windows.

The ideal thermochromic coating would be capable of high visible transmittance as well as high IR modulation and would be processed on a flexible substrate using a facile, low-temperature synthesis and fabrication method. A viable path towards this goal is VO₂ nanoparticles suspended in polymer thin films.¹⁰ In fact, the use of various VO₂ nanoparticle composites have given impressive results, with many designs already outperforming the traditional thin films.^{19,21,22,100,101} For instance, a VO₂ nanoparticle hydrogel composite currently outperforms all other methods at a performance of 62.6% visible transmittance and an IR modulation of 34.7%, although the window does not allow clear imaging in its high-temperature form.²⁸ Nevertheless, progress has been hampered by the difficulty of synthesizing monodisperse, high-crystallinity nanoparticles using a low-temperature, ambient-atmosphere, simple technique. Two main synthetic methods that have been studied, each with their own drawbacks. Hydrothermal synthesis can produce a nanoparticle powder, although it requires prolonged reaction times of 24 hours or more under high pressures. Sol gel, on the other hand, requires high temperatures, and the particles must be formed directly on the desired surface, hindering the use of a flexible low-temperature polymer substrate. Despite these synthetic and nanofabrication drawbacks, simulations suggest that the VO₂ composite path is essentially the most promising route to enhance the performance metrics and augment the potential for large scale use of VO₂ in thermochromic windows.²⁰

In this paper, we present simulations that suggest that taking advantage of the tunability of the plasmon resonance in metallic VO₂ could lead to the highest performing thermochromic windows to date. We demonstrate the feasibility of this approach by creating VO₂ nanoparticle

composites in a flexible elastomer. A high-yield, low-temperature, ambient-pressure reaction was used to create quality VO₂ nanoparticles, which were then mixed with polydimethylsiloxane (PDMS) in a simple film fabrication method. We were able to achieve an 11.9% IR modulation at 50.7% clear visible transmittance. This method is substrate independent and has tunable performance while requiring no temperatures higher than 250 °C for either nanoparticle synthesis or film preparation. The optical and elastomeric properties of the VO₂ colloidal films were thoroughly investigated, including the beneficial effect of stretching the elastomeric matrix on the thermochromic performance of the composite.

3.2. Experimental

For details on nanoparticle synthesis and film fabrication see **Methods 2.2** and **Methods 2.3**, respectively. VO₂ particle morphology, identity and quality were measured with SEM, XRD, and DSC. XRD spectra was taken from 10°-60° 2θ at a scan rate of 2° 2θ/min where the powder was spread on a no background sample holder. Film thickness was measured by profilometry where the heights from 5 different line scans evenly spaced across the film were averaged together using the Vision 64 program. Optical pictures and macroscale pictures were taken. See **Methods 2.1** for details. Thermochromic window infrared modulation analysis – see **Methods 2.4**. Simulation details are discussed in **Methods 2.5**.

3.3 Results and Discussion

Simulations exploring the optical properties of VO₂ nanoparticles have noted the importance of the surface plasmon of metallic VO₂ (R) with a resulting absorption peak around ~1.2 μm.¹³ The effect of the particle size and shape on the plasmon resonance has also been studied, noting the changes in spectral location and width of this resonance by tuning the size and the aspect ratio.¹⁰² However, the ability to tune the plasmon resonance spectral position has

not been fully utilized to enhance IR modulation.¹⁰³ In order to maximize performance, the plasmon resonance must be tuned to the IR spectral range with the highest solar irradiance, which is concentrated between 0.8 and 1.2 μm . To understand the relationship between nanoparticle size and plasmon resonance position, and to predict the potential performance of VO₂ elastomer colloidal films, Mie scattering simulations were employed. The diameter of the VO₂ spherical nanoparticle was varied from 10 nm to 200 nm within a PDMS matrix. The resulting extinction efficiency, $Q_{ext}(\lambda)$, for each particle was calculated as a function of wavelength, λ , and converted into a transmittance spectrum, $\%T(\lambda)$, using:

$$\%T(\lambda) = \exp(-NL\pi r^2 Q_{ext}(\lambda)) \quad (3.1)$$

where N is the number of nanoparticles per unit volume, L is the film thickness, and r is the radius of the nanoparticle for calculating the geometrical cross section, πr^2 .¹⁰⁴ N can be parameterized to depend on the weight percent, w , of nanoparticles as $N = N_{max}w$, where N_{max} is the maximum number of particles per unit volume assuming a close-packed simple cubic lattice of VO₂ nanoparticles. The visible transmittance figure of merit, T_{vis} , was calculated separately for VO₂ (M₀) and VO₂ (R) using:

$$T_{vis} = \frac{\int \%T(\lambda)\phi(\lambda)d\lambda}{\int \phi(\lambda)} \quad (3.2)$$

where $\phi(\lambda)$ is the AM1.5G solar irradiance and the integral runs from $\lambda = 350$ to 750 nm and then the two values were averaged values. The IR modulation, ΔT , was calculated using **Equation 3.2** with an integral from $\lambda = 750$ nm to 2000 nm for both VO₂ (M₀) and VO₂ (R) and taking the difference:

$$\Delta T = T_{IR}^{Mo} - T_{IR}^R \quad (3.3)$$

The experimentally tunable parameters L and w in **Equation 3.1** were varied such that their product, Lw , ranged from 0.0005 to 0.15 and then T_{vis} and ΔT were calculated using **Equations 3.2** and **3.3** to obtain the possible performance values at each particle diameter.

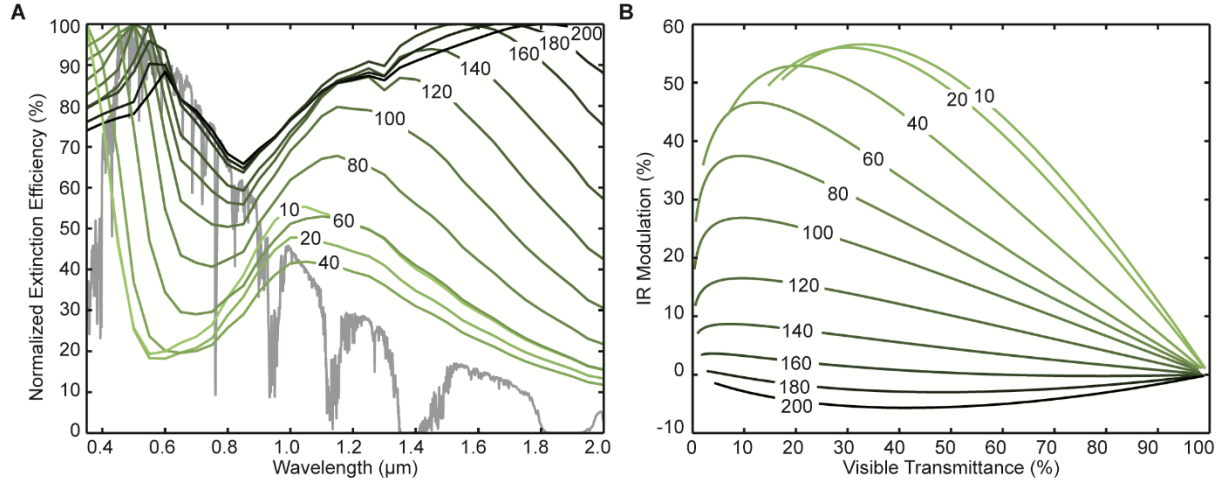


Figure 3.1. Optical simulation data of PDMS embedded with spherical VO_2 nanoparticles ranging in diameter from 10 nm to 200 nm. **A**, Normalized extinction efficiencies, Q_{ext} , (green curves) for VO_2 in the metallic R phase with various nanoparticle diameters. Gray curve depicts the AM1.5G solar irradiance. **B**, Correlation of IR modulation, ΔT , with visible transmittance, T_{vis} , for each particle diameter. Curves at each diameter correspond to the product lw ranging from 0.15 on the far left to 0.0005 on the far right. All labels in panels A and B are in units of nanometers.

The Q_{ext} spectra in **Figure 3.1 A** show a distinct peak at near-infrared wavelengths that red shifts with increasing particle diameter from less than 1 μm to nearly 2 μm . The use of a dielectric matrix, as opposed to air, enhances the plasmon resonance by changing the permittivity, boosting overall performance.¹⁰² The spectral position of the plasmon resonance with respect to the solar irradiance intensity dictates the performance values achievable. A 10 nm VO_2 nanoparticle colloidal film can achieve a performance of 50% IR modulation at a visible

transmittance of 50% because of the placement of the plasmon resonance at $\sim 1 \mu\text{m}$, where there is strong IR solar irradiance. On the other hand, a 200 nm particle cannot achieve any IR modulation at any visible transmittance because the plasmon resonance is tuned to approximately $2 \mu\text{m}$, where there is negligible solar irradiance. Intelligently using the nanoparticle size to tune the plasmon resonance within a transparent dielectric matrix could enhance the performance of VO₂ windows to achieve significantly higher performances than those reported to date.

The simplicity of a colloidal film design coupled with potentially impressive performance, as suggested by the simulations, are the impetus to experimentally pursue VO₂ colloidal films. There are a few requirements for the synthesis and film fabrication if it is to be a simple and economically viable option for widespread adoption of thermochromic windows. First, all procedures must be carried out at low temperature and in ambient atmosphere to ensure industrial scalability of resulting films. Second, the synthesis must produce nanoparticles in solution that can be dried to a powder in order to be incorporated into a polymer solution and deposited on arbitrary substrates. Here, a slight modification of a facile, low-temperature, ambient-condition synthesis was used to achieve a high yield of VO₂ nanoparticles.⁷¹ This synthesis relies on the conversion of vanadyl ethylene glycolate (VEG) to VO₂ through thermolysis, which affords a high yield of nanoparticles with an average diameter of $45 \pm 25 \text{ nm}$ (**Figure 3.2 A**). By synthesizing VO₂ through thermolysis, the preferential rod crystal growth is bypassed.¹⁰⁵ Based on our simulations, the spherical shape and sub-100 nm size selection provided by this synthesis is essential for the performance of the VO₂ films. X-ray diffraction (XRD) spectra (**Figure 3.2 B**) confirm full conversion of VEG to VO₂ by the strong peak at 27.8° (JCPDS card no. 44-0252). The direct conversion to VO₂ (M₀) ensures that there are no other VO₂ crystal phases present. Finally, differential scanning calorimetry (DSC) in **Figure 3.2**

C shows the SMT occurs at a temperature of $\sim 66^\circ\text{C}$ upon heating and $\sim 57^\circ\text{C}$ upon cooling, with a hysteresis of 9°C . The transition temperature and wide hysteresis is typical of VO_2 nanoparticles.¹⁰⁶

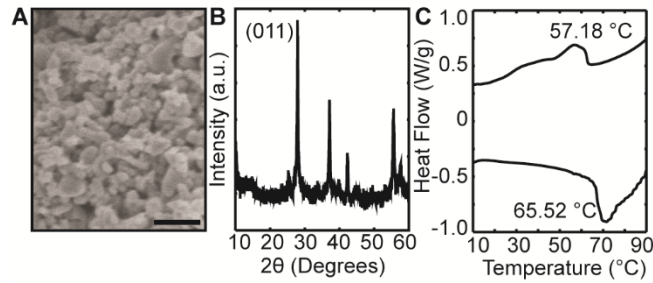


Figure 3.2. Characterization of VO_2 nanoparticles. **A**, SEM image of nanoparticles with average size of 45 nm. Scale bar 200 nm. **B**, XRD pattern of as-synthesized nanoparticles. **C**, DSC of nanoparticles shows SMT temperatures of $\sim 66^\circ\text{C}$ and $\sim 57^\circ\text{C}$.

The as-synthesized nanoparticles were suspended in a dilute PDMS solution and varying film thicknesses were achieved via drop-casting on glass substrates. This simple fabrication method created high-quality films with thicknesses ranging from ~ 15 to $\sim 75\ \mu\text{m}$.

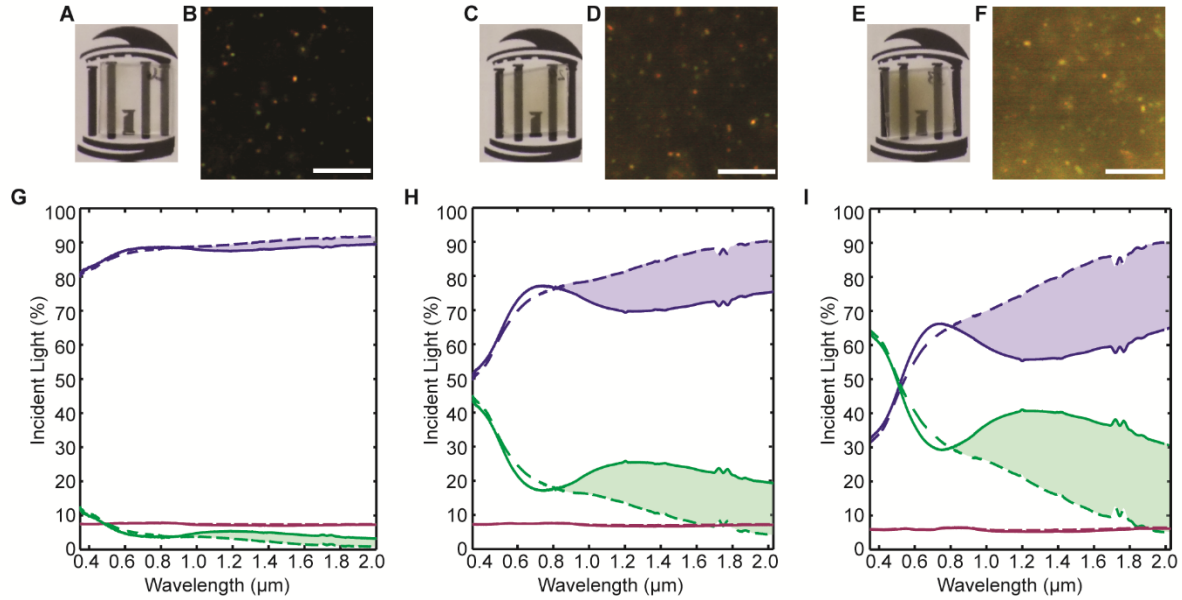


Figure 3.3. Optical properties of representative films where the left column (**A, B, G**) is an ~ 15 μm thick film, the middle column (**C, D, H**) is an ~ 40 μm thick film and right column (**E, F, I**) is an ~ 75 μm thick film. **A, C, E**, Macroscale images of respective films. **B, D, F**, Dark-field images of respective films, showing an increase in particle concentration via color change as well as high dispersity of nanoparticles. Scale bar 8 μm . **G, H, I** Optical properties of individual VO_2 films, where blue is transmittance, green is absorptance, and pink is reflectance. The dashed line indicates room-temperature optical measurements for each color, and thick line indicates high-temperature optical measurements.

Figure 3.3 A, C, E shows the visible film quality with varying thicknesses, with an example of the thinnest, thickest and an intermediate film. There is a slight brownish tint to the films, and the relatively minimal scattering makes the background design clearly visible through the films. **Figure 3.3 B, D, F** shows dark-field microscopy images, where the increase in background color with film thickness shows the increase in number of small nanoparticles, and the overall lack of bright dots suggests a minimal number of particle aggregates or large nanoparticles. The uniform dispersion of nanoparticles within the film is essential for obtaining high performance because it minimizes large scattering centers that do not exhibit the

desired plasmon resonance (*cf.* **Figure 3.1**). Finally, the optical properties of each film were studied at room temperature and above the SMT temperature, at 80 °C, as shown in **Figure 3.3 G, H, I**. The high transmittance at long wavelengths shows the high quality of the films, as there should be negligible scattering or absorptance. The high absorptance at short wavelengths, giving the films their color, is expected due to the inter- and intra-band absorptions of VO₂.^[6] At high temperature, the metallic VO₂ nanoparticle plasmon resonance absorbs most predominantly around 1.2 μm, which causes the decrease in infrared transmittance at the same spectral position.¹³ This observation is qualitatively in agreement with simulations; however, simulations predict the absorptance peak at the plasmon resonance should be more intense and narrower than the broad peak observed experimentally. This discrepancy can be reasonably explained by the large size distribution of synthesized nanoparticles within the film, effectively averaging over a distribution of plasmon resonances. A small number of rod-shaped particles within the sample may also contribute to broadening of the plasmon resonance.¹⁰⁷ The visible transmittance decreases with an increase in film thickness, offset by an equal increase in absorptance, as expected.²⁶ The reflectance is consistently low for each film thickness across all wavelengths.

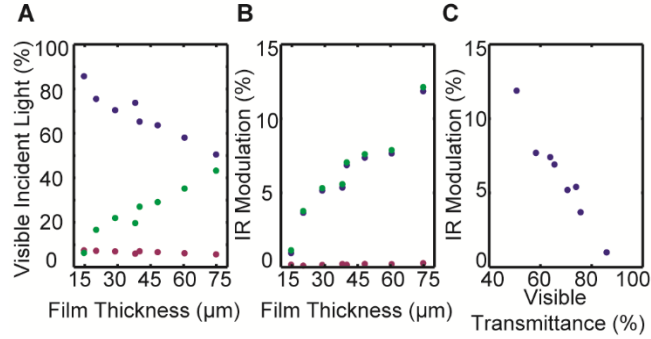


Figure 3.4. Performance values for films varying in thickness from ~15 to ~75 μm . **A**, Percentage of visible light transmitted (blue), absorbed (green), and reflected (pink). **B**, Percentage of IR light modulated by transmittance (blue), absorptance (green), and reflectance (pink) for the same films. **C**, Range of performances achievable by modulating the thickness of the film.

The performance of VO_2 films as a function of film thickness is summarized in **Figure 3.4**. The IR modulation for absorptance and transmittance nearly overlap, showing that the performance is solely due to the increase in absorptance, which ultimately relies on the metallic VO_2 plasmon resonance. This result is in contrast to what is seen in VO_2 thin films, where the change in reflectance and absorptance both contribute to the IR modulation.¹³ The performance was tuned from an IR modulation of 0.97 % at a visible transmittance of 85.8% to an IR modulation of 11.9% at a visible transmittance of 50.7%.

We also examined the elastomeric properties of the colloidal films and the influence on the optical properties and thermochromic performance. The elastomer matrix allows the thickness of the films to be modulated simply by stretching. The film was simply peeled from the glass substrate on which it was prepared, stretched, and measured for visible and IR transmittance as before. For the film shown in **Figure 3.5**, the performance values achieved were 45.6% visible transmittance and an IR modulation of 7.6%. The film was then stretched ~36% and the transmittance was measured again, producing a visible transmittance of 55.4% and an IR

modulation of 8.1%. The general shape of the transmittance spectra of both the stretched and un-stretched films are similar to the films on the glass substrate, and the broad resonance is still clearly present.

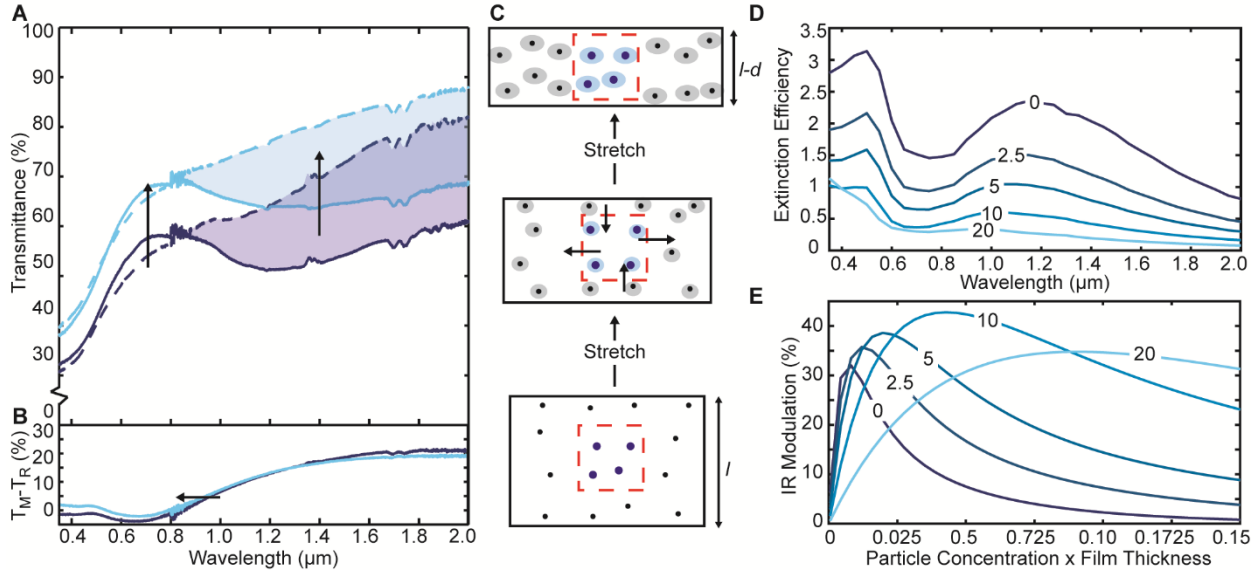


Figure 3.5. Effect of elastomeric properties of the film on thermochromic performance. **A**, Transmittance spectrum of the un-stretched film (dark blue) and the stretched film (light blue), where the dashed line indicates room-temperature transmittance and full line indicates high-temperature transmittance. **B**, $T_M - T_R$ spectrum of the stretched (dark-blue curve) and un-stretched (light-blue curve), showing the slight blue shift of the stretched film. **C**, Schematic of the change in film morphology and volumetric concentration upon stretching. **D**, Extinction efficiency, Q_{ext} , of a 90 nm VO_2 nanoparticle with varying shell thicknesses of air from 0 to 20 nm, all embedded in a PDMS matrix. **E**, Resulting IR modulation values at varying LW values ranging from 0.0005 to 0.15.

Remarkably, the overall performance for both visible and infrared figures of merit improved upon stretching the film. The $T_{M_0} - T_R$ spectrum (**Figure 3.5 B**) was calculated by taking the difference between the high-temperature transmittance curve and the low-temperature transmittance curve, and it shows a slight blue shift of the stretched film. This effect can be explained by a change in the morphology of the film upon stretching (**Figure 3.5 C**). As the film is stretched, the film thickness decreases, but the volume concentration of nanoparticles stays

constant because the Poisson ratio of PDMS is 0.5 and the film is effectively incompressible. Stretching the film induces strain onto the composite film, which is localized into high-stress regions centered around the nanoparticles. Voids are then likely to form at these high-stress areas due to the ease of delamination at the interface of PDMS (hydrophobic) and the VO₂ nanoparticles (hydrophilic). Similar effects have been observed in other elastomer composites.¹⁰⁸ The decrease in thickness by $L-d$ is the primary reason for the increase of visible transmittance upon stretching the composite film, as can be seen through the modification of **Equation 3.1** to

$$T_{vis}^{Stretch} = T_{vis} + dN\pi r^2 Q_{ext} \quad (3.4)$$

where the decrease in film thickness (d) is small. Mie scattering simulations (**Figure 3.5 D**) show that the introduction of a shell of air, which represents the presence of a void in the near-field of the particle, positively contributes to both the visible transmittance and IR modulation. The air shell decreases the extinction efficiency intensity because of the introduction of a lower refractive index material. This decrease in intensity increases the visible transmittance of the films overall. The plasmon resonance spectral position is also affected, changing from $\sim 1.2 \mu\text{m}$ to $\sim 1 \mu\text{m}$ with the introduction of an air shell. This beneficial shift to a higher solar irradiance intensity region occurs because the plasmon resonance spectral position of VO₂ in air is closer to the visible spectrum. The experimentally observed blueshift of the stretched T_M-T_R spectrum does support the overall shift of plasmon resonances expected upon stretching.

The possible IR modulation was then calculated at Lw values of 0.0005 to 0.15 and it can be seen (**Figure 3.5 E**) that the IR modulation does increase by introducing a shell of air up to a shell thickness of 20 nm, caused by the improved position of the plasmon resonance relative to the solar spectrum. The introduction of a small air shell at a constant w while decreasing l should

give a large increase in IR modulation. Experimentally, the effect we observe is consistent with this expectation but is somewhat smaller than expected, probably again due to the large distribution of nanoparticle sizes and therefore air shell thicknesses. The ability to improve visible transmittance and simultaneously improve IR modulation simply through stretching the elastomeric colloidal film is a unique way to increasing performance. This improvement introduced by air pockets opens the door to different potential avenues for improving the performance by designing thermochromic films with enhanced performance.

Simulations demonstrated that VO₂ PDMS colloidal films had the potential of outperforming all current thermochromic windows, and we have shown that this approach is experimentally viable. Reasonable performance values well within the range of top performing thermochromic windows have been achieved. The optical properties have been rigorously analyzed. The impact of the plasmon resonance on performance is clear, and it can be shifted to a more optimal spectral position by stretching the elastomer colloidal films. In order to improve performance overall, the synthesis must be improved by both decreasing the nanoparticle size and the size distribution. Additionally, this approach can be used in tandem with other known methods for improving overall performance, such as doping the nanoparticles to lower SMT temperature, or placing it in temperature sensitive performing polymers.

3.4. Conclusion

We have fabricated VO₂ elastomer colloidal films, all while using a low temperature, scalable synthesis and fabrication method. Performances were ranged from an 0.97 % IR modulation at 85.8% visible transmittance to an 11.9 % IR modulation at 50.7 % visible transmittance by tuning the thickness. Optical extinction analysis elucidated the importance of plasmon resonance in the IR modulation, thus the performance of the thermochromic window.

Upon stretching, the performance increases from 45.58 % visible transmittance and an IR modulation of 7.6 % to 55.43 % visible transmittance and an IR modulation of 8.1 %. We have demonstrated the viability of these films for real application experimentally and we have shown through simulations that by tuning the nanoparticle size and thus the plasmon resonance it is possible to achieve 50 % IR mod and 50 % visible transmittance within this framework.

3.5 Acknowledgements

This work was funded in part by the Research Corporation for the Science Advancement (#22371) and in part by a Packard Fellowship for Science and Engineering (J.F.C.). The authors thank the Chapel Hill Analytical and Nanofabrication Facilities (CHANL), Energy Frontier Research Center (EFRC), chemistry department x-ray facility and the Ashby lab for providing expertise and access to fabrication and analytical equipment.

Chapter 4: PROBING THE VALENCE BAND DENSITY OF STATES OF NIO: UNDERSTANDING THE IMPACT OF DEFECT STATES ON TRANSPORT, CHARGE INJECTION AND RECOMBINATION

To be submitted by: Moot, T.; Li, L.; Shan, B.; Donley, C. L.; McCullough, S. M.; Taggart, A. D.; Meyer, T. J.; Kanai, Y.; Cahoon, J. F.

4.1 Introduction

In any photovoltaic or solar fuel device the fundamental parameters of the semiconductor, such as the band edge position, dopant type, defect density, and Fermi level (E_f) must be known in order to design efficient devices and effectively interpret results. Within photoelectrochemical (PEC) devices such as a dye sensitized solar cell (DSSC), the energetic difference between the E_f and the Nernst potential set the theoretical maximum open circuit voltage (V_{OC}), significantly affecting the overall device power conversion efficiency (PCE).⁴⁰ In tandem devices for solar fuel generation, such as a dye sensitized photoelectrochemical cell, the conduction and valence band edges inform which materials are viable candidates for H_2O oxidation and CO_2 reduction.¹⁰⁹

In highly doped, low defect density semiconductors, the E_f lies close to either the conduction band edge (CBE) for an n-type semiconductor or to the valence band edge (VBE) for a p-type semiconductor. This has allowed researchers investigating metal oxides for PEC applications to use measurements of the E_f as an approximation of the band edge position which is preferable because the E_f is typically easier to measure experimentally in an electrolyte environment (solvent, cation, pH) which can significantly alter the band edge position.^{65,110} Mott Schottky is the most commonly used techniques to measure the E_f in solution, or more

specifically the flatband potential (V_{fb}).¹¹¹⁻¹¹³ This measurement of V_{fb} as an approximation for the band edge has proved fruitful to understand device results for low defect density n-type semiconductors like TiO_2 , ZnO and SnO_2 commonly used in PEC applications.⁶⁶

However, the p-type semiconductor most commonly used for PEC applications, NiO , does not have a low defect density. Although NiO is a wide band gap material (E_{gap} 3.6-4.0), the nanoparticle material is black when synthesized or bought commercially.⁵⁴ This dark color is indicative of a large trap state density above the VBE. Significant effort has been devoted to understanding the defect density magnitude and character within NiO , as it deleteriously affects the device performance.^{53,54,114-116} It is currently believed that the trap states are due to a combination of Ni^0 , Ni^{3+} , and Ni vacancy defects.^{53-55,117} In terms of devices, NiO DSSCs have reached fill factors at only ~40 %, whereas TiO_2 DSSCs have reached ~80%, which contributes to the 7 times lower PCE of p-DSSCs as compared to n-DSSCs.^{45,46,51,118} This lowering of fill factor is largely due to the low shunt resistance in NiO , indicative of undesired trap-mediated electron transfer.⁵² Furthermore, the current understanding of the VBE position and defect density for NiO has not allowed for complete removal of the defect states without decreasing device PCE.^{54,55,74} For example, passivation techniques such as targeted atomic deposition (TAD) or high annealing conditions result in a white colored material and show improvements in the V_{OC} , suggesting a passivation of states. However, the photocurrent drops precipitously minimizing the expected improvements in performance. This suggests that the current understanding of the trap state density is incomplete.

Due to the large amount of trap states reported in NiO , it is not clear if the assumption that the E_f is a valid approximation for the VBE is true. The Anderson localization theory for non-crystalline solids and the Cohen, Fritzsche and Ovshinsky (C.F.O.) model state that for low

crystallinity materials with large amounts of defects the E_f can be shifted far from the band edge.¹¹⁹ By re-assessing the assumption that the $E_f \approx \text{VBE}$, we are able to more accurately probe the E_f and the VBE position which allows for a more complete understanding of the magnitude and identity of the defect density, and finally how it affects device performance. Although our focus is on the impact of the defect states on the photovoltaic performance of NiO, we expect that these findings will be relevant to those using NiO for other applications, such as catalysis or electrochromic applications.

To be consistent with as much of the literature as possible, the commercially available NiO inframat nanoparticle powder was used in all studies. We employ a multitude of electrochemical and material characterization techniques in conjunction with DFT+U first principles calculations to understand the magnitude and identity of the trap states. Subsequently, we probe the effects of the defects on charge injection, recombination and transport using a p-type DSSC as a model system. We find that the E_f is 1.5 eV above the VBE and that the defect states exclusively control charge injection, recombination and transport through NiO.

4.2 Experimental

For information of NiO paste preparation and DSSC fabrication see **Methods 2.7** and **2.8**, respectively. All characterization methods are discussed in **Methods 2.1**, **2.9**, **2.12** and **2.13**.

4.3 Results and Discussion

Mott-Schottky is one of the most commonly used techniques for probing the E_f of semiconductors in a solution by measuring the V_{fb} , although is often reported as VBE. The measurement is based in the change of capacitance from the band gap to the band edge, where a high capacitance in the band gap drops by $1/C^2$ to a low capacitance in the band as the density of states increases.^{111–113} Surprisingly, there are only a few electrochemical measurements of V_{fb}

values reported for NiO, and all of them are consistent, regardless of solvent used.^{39,40,46,74,116,120}

The values should not be consistent given the effect of solution on the V_{fb} is well known and can modulate the TiO_2 V_{fb} by up to 1 volt.^{65,66,110} In order to thoroughly probe the E_f and VBE, we use two different annealing conditions of the NiO inframat, one as typically prepared at 450 °C for 0.5 hour (450-NiO) and at 600 °C for 1 hour (600-NiO).

In **Figure 4.1 A** the measured Mott-Schottky curve at 100 Hz shows a V_{fb} of -0.12 V vs Ag/AgCl for 450-NiO and 0.36 V vs Ag/AgCl for 600-NiO. Similarly, we see that the E_f shifts 460 mV upon annealing (**Figure 4.1 D**) through changes in the secondary electron cutoff (SECU) value. This is remarkably similar to the measured change in V_{fb} of 480 mV with annealing. If NiO was defect free, there should be no change in the E_f with annealing temperature, however we see a change in V_{fb} of 0.48 V with annealing. Additionally, we note that the value for 450-NiO is different from the typically reported value of between 0.3 V vs Ag/AgCl and 0.5 V vs Ag/AgCl, but is expected because these values were measured in a water based electrolyte.¹²⁰

Next, to understand the magnitude of trap state density the density of states (DOS) is measured. The DOS of NiO was obtained from cyclic voltammetry (CV) by the equation

$$DOS=C/[(1-p)*q*L] \quad (4.1)$$

where p is porosity, q is the elementary charge and L is the film thickness. C , capacitance, was calculated from the current density/scan rate. For both 450-NiO and 600-NiO (**Figure 4.1 B**) there are two main peaks at ~ 0.2 V vs Ag/AgCl, ~1.1 V vs Ag/AgCl and an exponential rise in the DOS at 2.0 V vs Ag/AgCl. The first peak is consistent with the reported large trap state density of NiO.^{54,57} Analysis of the UPS data shows a peak at 29.6 eV, which has been previously shown to be a surface defect state.¹²⁴ An exponential rise in DOS is indicative of a band edge for

TiO₂-like metal oxide semiconductors.¹²¹ There is a significant decrease in intensity of the two DOS peaks upon annealing, but still a clear exponential onset of the peak at 2.0 V vs Ag/AgCl. Thus, we can confidently say that the peaks are all due to various trap states in NiO and the VBE is unmoved. Spectroelectrochemistry was used to measure a VBE value through probing the change in optical absorption under applied bias, which resulted in a VBE of 1.51 V vs Ag/AgCl (Figure 4.1 C, Figure 4.2).^{122,123} We note that the VBE is likely ≥ 1.5 V vs Ag/AgCl as the true value is convoluted by factors such as increased faradaic current and the electrochemical solvent window (Figure 4.3).

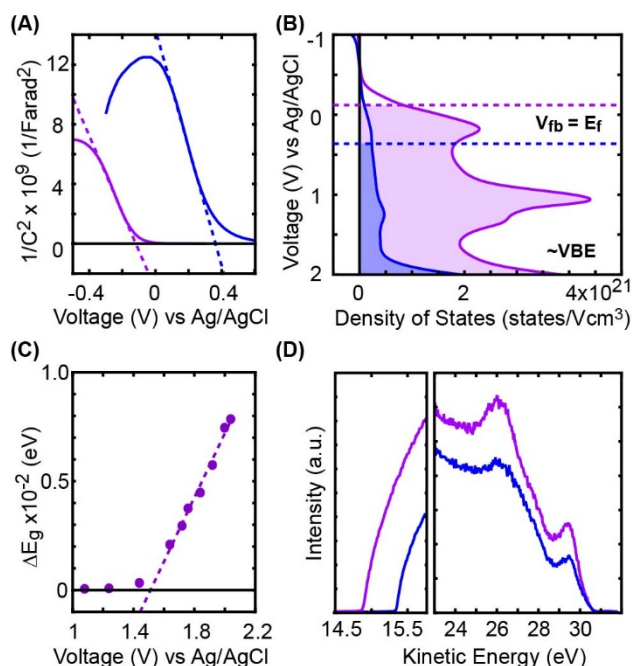


Figure 4.1: NiO V_{fb} measured by Mott-Schottky and compared to DOS map. A) Representative Mott-Schottky curve at 100 Hz with the fitted area denoted by the dashed line. B) DOS map of NiO where the dashed line corresponds to the V_{fb} and the shaded region denotes filled states. C) The change in optical absorption (ΔE_g) between subsequent applied biases versus applied bias where the x-intercept is the VBE. D) Left, UPS spectra secondary electron cutoff and right, UPS spectra of the valence band edge. For all graphs 450-NiO traces are purple and 600-NiO traces are blue.

The V_{fb} values are due to the onset of trap states as opposed to the VBE as Mott-Schottky is sensitive to an abrupt change in the density of states, i.e. the E_f , but not the type of state. Consequently, the doping level values obtained for NiO from Mott-Schottky also corresponds to the trap state onset and therefore are not rigorously correct. From a combination of the V_{fb} , the DOS spectra and an approximate VBE of 1.5 V vs Ag/AgCl, we determined the trap state density of 450-NiO as 5.04×10^{21} states/cm³ and 600-NiO as 5.90×10^{20} states/cm³.

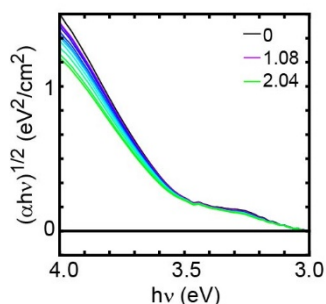


Figure 4.2. Change in 450-NiO bandgap with applied bias (V vs Ag/AgCl).

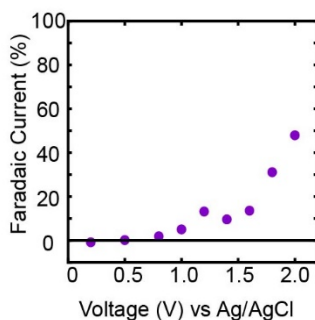


Figure 4.3. Percent of total current arising from faradaic current for 450-NiO.

To determine the chemical identity of these trap states, multiple material characterization techniques were used. We see that the black 450-NiO changes to light grey for 600-NiO (**Figure 4.4 A**), representative of a decrease in trap states. This color change supports the assertion that the typically prepared NiO is not pure and/or contains significant defect states.^{54,55}

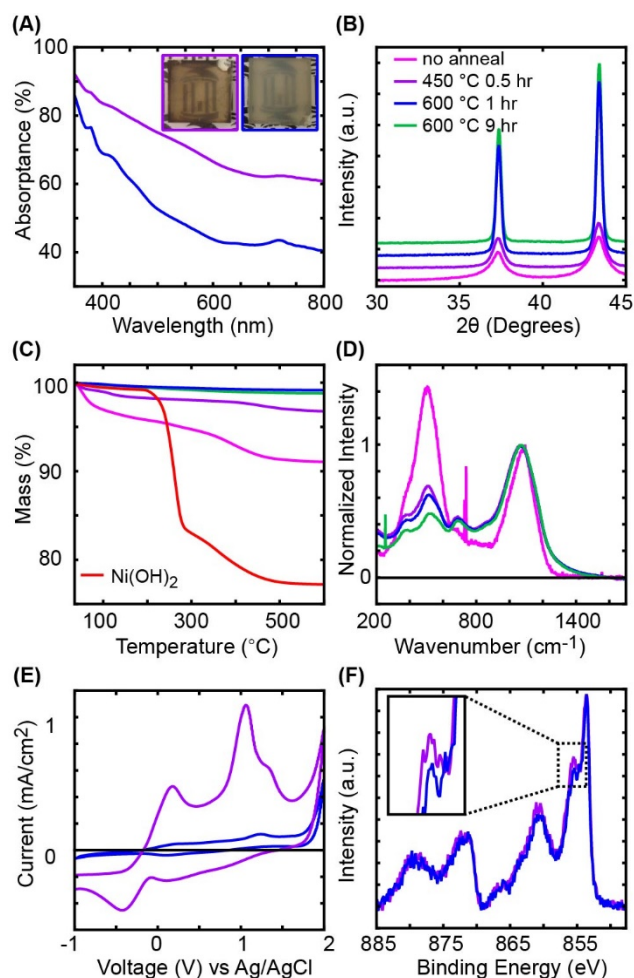


Figure 4.4. Characterization of NiO. A) UV-Visible spectra with inset of 450-NiO nanoparticle film (left) and 600-NiO film (right). B) XRD of different annealing conditions of inframat NiO. C) Thermogravimetric analysis of Ni(OH)₂ and different annealing conditions of inframat NiO. D) Raman spectroscopy. E) Cyclic Voltammetry in 1.0M LiClO₄ MeCN. F) XPS spectra of Ni peaks with inset of Ni³⁺ peak. All have the same colors corresponding to annealing conditions as follows: Ni(OH)₂ (red) and NiO inframat (pink), 450-NiO (purple), 600-NiO (blue), and 600 °C for 9 hr (green)

To see if there are any other residual crystalline phases in the black NiO, X-ray diffraction (XRD) was done (**Figure 4.4 B**). Although there is a significant change in the peak height and full-width half-maximum with annealing temperature conditions there is no Ni⁰ or Ni(OH)₂ peaks in the NiO XRD. 450-NiO has a crystallite grain size of 10 nm as calculated through the Debye-Scherrer analysis, which increases to 21-24 nm for 600-NiO, where the

average nanoparticle size is ~ 20 nm. Thermogravimetric analysis (TGA) was subsequently done to determine if the decrease in trap DOS was due to removal of a chemical species, or improved crystallinity. Ni(OH)₂ is a possible candidate for defects because it is a common NiO precursor, and therefore was used as a comparison for NiO TGA. As seen in **Figure 4.4 C**, there is a quick decrease in mass percent for Ni(OH)₂ at ~280 °C where the majority of Ni(OH)₂ conversion to NiO and H₂O takes place, but there is still considerable mass loss between 300 °C and 500 °C.¹²⁵ A similar mass loss profile between 300-500 °C is seen for both the as-bought Inframat and the 450-NiO, suggesting that there is H₂O being lost from amorphous residual Ni(OH)₂ whereas the mass loss for 600-NiO is negligible at < 1%. Raman spectroscopy (**Figure 4.4 D**) was then done, where there is a significant decrease in the peak height at ~500 cm⁻¹ with increase in annealing, which has been reported as a state that arises due to defects.¹²⁶ The cyclic voltammetry peak for 450-NiO at 0.18 V vs Ag/AgCl is a redox active peak as characterized by two, almost equal in area peaks where the peak maximum is slightly offset from each other (**Figure 4.4 E**). This peak is in a similar potential range of the Ni(II)/Ni(III) redox peak from



where the existence of Ni(OH)₂ is corroborated by the mass lost shown in TGA the (**Figure 4.4 C**) as well as the disappearance of the redox peak in the CV for 600-NiO.^{9,117,127}

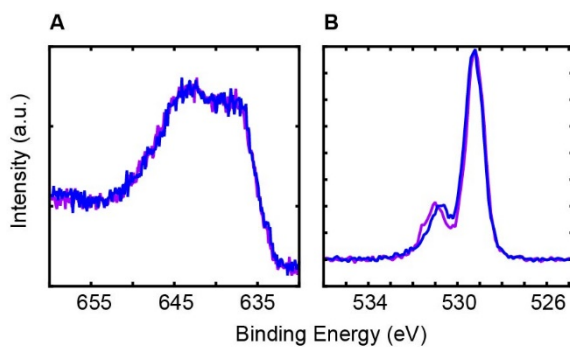


Figure 4.5. XPS of NiO, A) Auger peaks and B) Oxygen peaks of 450-NiO (purple) and 600-NiO (blue)

Finally, there are slight changes in the Ni XPS that correspond to a decrease in intensity at the Ni³⁺ peak (~855.5 eV) with annealing (**Figure 4.4 F**, **Figure 4.5**).¹¹⁷ The existence of a Ni³⁺ peak in correlation with a decrease in mass loss and the redox active peak strongly suggests that there is residual amorphous Ni(OH)₂ like defects left in NiO. The small decrease in XPS peak intensity could be due the minimal amount of Ni(OH)₂ like regions, at most ~10 wt. % Ni(OH)₂ as expected based on TGA. However, we note that the Ni and O XPS peaks for NiO are quite complex, where there are 7 Gaussian peaks that must be fit for pure NiO and 7 Gaussian peaks for Ni(OH)₂.¹¹⁷ We emphasize that since XRD is not sensitive to amorphous regions or single-site defects and the Ni XPS spectra is particularly complicated, TGA and Raman spectroscopy are more sensitive at probing for any residual Ni(OH)₂ left in NiO.

To probe the identity of this peak more extensively, we turn to density functional theory (DFT) calculations with Hubbard correction to model the change in density of states with various defects in NiO. Based on our assertion that there are amorphous Ni(OH)₂ like regions left in NiO there are two different possible defect types: a OH⁻ in the Ni vacancy, reminiscent of a NiOOH character, and a H₂O in the Ni vacancy, reminiscent of Ni(OH)₂ character. Additionally, it is possible there are Ni vacancies, as that is often how binary metal oxides become p-type doped. In

all of these simulations any charge is allowed to be delocalized across the entire crystal, but for simplicity we will refer to the defects as noted above.

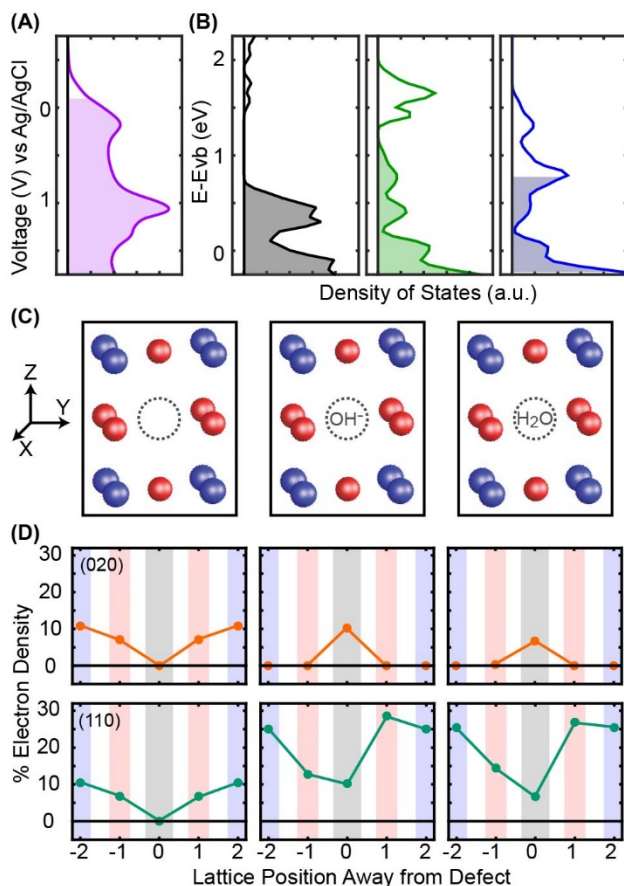


Figure 4.6: Identification of the trap state character. A) DOS map of 450-NiO annealed B) DOS calculated from DFT+U calculation of NiO with a Ni vacancy (left), Ni vacancy with an OH⁻ in it (center) and Ni vacancy with an H₂O in it (right), where the shaded part is the filled states and unshaded is unfilled as determined by the calculated Fermi level. C) Schematic of the atomistic structure of Ni (blue), O (red) and defect state (grey dashed circle) corresponding to a Ni vacancy (left), Ni vacancy with an OH⁻ in it (center) and Ni vacancy with an H₂O in it (right). D) Percent of total electron density per atom in the (020) (orange, top panel) and (110) (teal, bottom panel) planes intersecting with the defect for a crystal with a Ni vacancy (left), Ni vacancy with an OH⁻ in it (center) and Ni vacancy with an H₂O in it (right). Ni atoms are denoted by blue shading, O as red, and the respective defect as grey.

The introduction of a Ni vacancy creates a single shallow peak above the band edge with a breadth of ~0.5 V (**Figure 4.6 B**, left). The experimental DOS has 2 main peaks above the band edge and the filled states extend over 1.5 V above the VBE (**Figure 4.6 A**), indicating that Ni

vacancy cannot be the only defect present. The introduction of OH^- into a Ni vacancy creates two peaks above the band edge, where the filled states extend to ~ 1.25 V above the VBE (**Figure 4.6 B**, center). Introduction of H_2O into a Ni vacancy creates two peaks, however only 1 peak has filled states which extend to ~ 0.75 V above the VBE (**Figure 4.6 B**, right). The trap state density resulting from a combination of the three different trap states matches well with the experimentally determined DOS (**Figure 4.6 A**), where the experimental DOS peak at ~ 0.2 V vs Ag/AgCl is primarily $\text{OH}^-/\text{H}_2\text{O}$ defect character and the peak at ~ 1.1 V vs Ag/AgCl is primarily Ni vacancy character.

By mapping out the residual electron density caused by the defect we can see how the electron density shifts to stabilize the defects (**Figure 4.6 C, D**). Specifically, the electron density maps on the left shows a pictorial representation of the displaced electron density and on the right, the top graph shows the percent electron density through the defect in the y direction and the bottom graph shows the same but in the z direction. For the Ni vacancy (**Figure 4.6 C, D** left) there is some electron density localized on the vacancy nearest neighbor Ni, which is generally stabilized by the surrounding O. For the OH^- (**Figure 4.6 C, D** center) and H_2O defect (**Figure 4.6 C, D** right) this is true, but even more highly localized close to the vacancy. Interestingly, there is electron density at the defect site for both OH^- and H_2O defects, which could help to explain defect passivation via the reactivity of the defect site to various acid and ALD-like treatments.^{54,55} We also note that there is non-negligible electron density on a given Ni immediately in the vicinity of the defect, reaching 11% for the Ni vacancy and 29% and 27% for the OH^- and H_2O defect, respectively.

There is currently an argument about the existence of Ni^{3+} in NiO, where it has been recently reported that NiO cannot have any Ni^{3+} states because the VBE is made up of almost

exclusively O character, although other papers have characterized Ni³⁺ in NiO through XPS.^{54,117} The VBE is exclusively O character only in pure NiO, and we have shown here that typically used NiO is not pure. Upon introduction of a defect, such as a Ni vacancy, OH⁻ or H₂O, the Ni character in the VBE increases to 37%, 27% and 28%, respectively, suggesting that it is possible to have a Ni³⁺ in the as-typically used defect NiO. Our DFT+U calculations also show that it is unlikely that a true Ni³⁺ is present, and the Ni character is more similar to a Ni^{2.3+}, or alternatively can be thought of as an increased probability of a true Ni³⁺ existing. We note that we also see the XPS signature of Ni³⁺ but again contend that the Ni XPS is very complicated and the changes are small and we cannot rely on the simple XPS analysis done here to determine the existence of Ni³⁺. We believe it is most likely that there is delocalized Ni³⁺ like character around the defect and that the specific charge on a defect adjacent Ni is between 2+ and 3+, and therefore has weak characteristics of Ni³⁺. This charged Ni occurs to stabilize the OH⁻ or H₂O defects.

The character of the trap states is well explained by the Anderson localization theory in non-crystalline solids, which is appropriate given the polycrystalline nature of NiO.¹¹⁹ In this theory, the states closest to the ‘true’ band edge occur from random variations in local potential. In the NiO case, this corresponds to a Ni vacancy where the resulting electron density is unevenly delocalized across neighboring oxygen and Ni atoms. The trap states towards the center of the band gap are attributed to energetic broadening from bonding defects, such as dangling bonds or occupied (D⁻) or unoccupied (D⁺) states. The Cohen, Fritzsche and Ovshinsky (C.F.O.) model states that these dangling bonds can act as donors or acceptors, which parallels the OH⁻/H₂O reminiscent of Ni(OH)₂/NiOOH redox peak seen towards the center of the band gap.¹¹⁹ The C.F.O model predicts that the E_f should be near to where filled and unfilled states overlap,

usually towards the center of the band gap for highly disordered materials. This was experimentally verified through V_{fb} measurements which measure the E_f to be ~ 1.5 V above the VBE.

The C.F.O. model goes further to predict that if there are large enough trap state density the charge transport can occur either through polaron hopping between localized neighboring trap states or via hopping from the trap states to the band edge.¹¹⁹ Conductivity measurements at different temperatures were taken (**Figure 4.7 A**) to determine the charge transport mechanism. First, the room temperature conductivity of 450-NiO is 3.6×10^{-6} S/cm whereas the conductivity of 600-NiO is nearly an order of magnitude lower at 2.2×10^{-7} S/cm. The 450-NiO value is comparable to typically reported values of $\sim 6 \times 10^{-6}$ S/cm.⁷⁴ Using the defect density as a proxy for doping level we see that the mobility is similar for 450-NiO and 600-NiO at 3.8×10^{-9} cm²/Vs and 2.0×10^{-9} cm²/Vs respectively. Although the mobility seems exceptionally low, it is within a reasonable range given that the literature conductivity values and the higher defect density, or doping level, calculated here. For example, a conductivity of 5×10^{-5} S/cm and doping level of 10^{20} states/cm³ would give rise to a mobility of 3×10^{-7} cm²/Vs, but using a defect density as the doping level of 10^{21} , gives a mobility of 3×10^{-8} cm²/Vs.⁷⁴ Because of the linear relationship between $\ln(\sigma)$ and $1/T$, the charge transport mechanism cannot be through band transport.¹¹⁹ In order to determine the charge transport mechanism, the conductivity data was fit to the two below equations correspond to defect only hopping and defect to band hopping behavior, respectively.

$$\sigma = \sigma_b \exp \left[-\frac{(E_f - E_b + \Delta W_{hd})}{k_B T} \right] \quad (4.3)$$

$$\sigma = \sigma_b \exp \left[-\frac{\Delta W_{hd}}{k_B T} \right] \quad (4.4)$$

Where σ_b is the bulk conductivity, E_b is the band edge energy, $\Delta W_{h,db}$ is the defect to band hopping barrier and $\Delta W_{h,d}$ is the defect only hopping barrier. From these equations we see that the defect to band hopping barrier ($\Delta W_{h,db}$) is 1.3 eV for the 450-NiO and 1.1 eV for the 600-NiO, whereas the defect only hopping barrier ($\Delta W_{h,d}$) is 0.2 eV for the 450-NiO and 0.4 eV for the 600-NiO. We also note that the ‘bulk conductivity’ (σ_b) for 600-NiO is 2.4 S/cm, close to single crystalline values and a bulk mobility of 0.02 cm²/Vs. This is in contrast to the 450-NiO σ_b of 0.0095 S/cm and a bulk mobility of 1.4 x 10⁻⁵ cm²/Vs. Previous reports have suggested that charge transport occurs through polaron hopping between localized trap states.⁵⁶ It is possible that both of these charge transport methods can occur, although all barriers are much higher than $k_B T$. If the defect to band hopping mechanism occurred that would likely mean that the Ni vacancy trap state is responsible for charge transport. However, if the defect only hopping mechanism was correct, it would likely mean that the OH⁻/H₂O trap state is responsible for charge transport.

To determine which hopping mechanism is most likely to occur, it must first be determined which trap states can conduct. The conductance of the trap states was measured (**Figure 4.7 B**) by measuring the conductance at different applied bias.¹²⁸ Each trap state has some conductance, however the OH⁻/H₂O character trap state is approximately 4 times less conductive than the Ni vacancy trap state. Because both trap states have conductance, it is possible that either charge transport mechanism is possible and therefore depends on the energy of the injected charge and the local concentration of defects. Based on the trap state density and assuming an equal distribution of defects, the distance between OH⁻/H₂O defects would be ~2 nm for 450-NiO and ~20 nm for 600-NiO.

Next, the effect of the trap states on charge injection is probed through measuring the change in photocurrent with applied bias in a three-electrode electrochemical cell. Here one of the standard p-type DSSC chromophores, P1 was used. We see in **Figure 4.7 C** that at the low applied bias (V_{app}) of -0.4 to -0.2 V vs Ag/AgCl, the photocurrent is 0.35 mA/cm² and 0.25 mA/cm² for 450-NiO and 600-NiO, respectively. At V_{app} of ~ 0 V vs Ag/AgCl the photocurrent precipitously drops approximately 2 orders of magnitude for both 450-NiO and 600-NiO. Based on recent transient absorbance (TA) spectroscopy work on NiO at various applied potentials, we know that the decrease in photocurrent is due to recombination from NiO with the chromophore.¹¹⁴ This drop in photocurrent occurs close to the onset of empty trap states, suggesting that it is the OH⁻/H₂O DOS peak that is primarily responsible for recombination and also possibly the state charges are preferentially injected into. Within a p-DSSC we would expect that the short circuit current (J_{SC}) would be proportional to the measured photocurrent at the E_f . Although the photocurrent at different V_{app} are similar for 450-NiO and 600-NiO, the E_f is quite different, suggesting that the measured J_{SC} should be up to 2 orders of magnitude lower for 600-NiO as compared to 450-NiO.

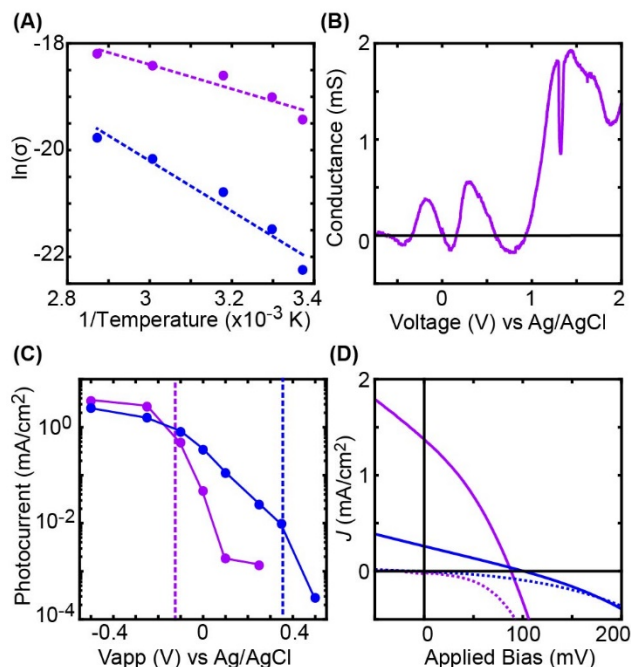


Figure 4.7: NiO DOS and DSSC performance and analysis. A) $\ln(\text{conductivity})$ versus $1/\text{temperature}$ used to fit for hopping and tunneling barriers. B) Conductance versus applied bias mapped against the DOS for 450-NiO. C) Photocurrent for the chromophore P1 versus applied bias with the dashed line marking the E_f . D) Champion JV curves where the dark curve is denoted by a dashed line. In all graphs the colors denote purple for 450-NiO and blue for 600-NiO.

To explicitly understand how these trap states affect p-DSSC performance, devices were fabricated and tested (**Figure 4.7 D**). The 450-NiO performance consistent with the standard device performance using the P1 chromophore and an iodide/triiodide in acetonitrile electrolyte.^{52,54} The average performance metrics for 450-NiO are a J_{SC} of $1.54 \pm 0.24 \text{ mA/cm}^2$, a V_{OC} of $87 \pm 2 \text{ mV}$ and a fill factor of $31.9 \pm 0.7 \%$. These device performance metrics are indicative of the problems plagued by NiO p-DSSCs: low V_{OC} , low short circuit density (J_{SC}) and particularly low fill factors, when compared to TiO_2 n-DSSCs.^{52,54} We see a slight improvement in V_{OC} for 600-NiO at $93 \pm 11 \text{ mV}$, although a significantly lower J_{SC} of $0.24 \pm 0.3 \text{ mA/cm}^2$ and a lower fill factor of $25.8 \pm 0.04 \%$. The lower J_{SC} for 600-NiO is as predicted from the photocurrent measurements. The slight increase in V_{OC} is also expected because of the shift

of the E_f , but is counteracted by the increase in recombination through some mechanism as evidenced by the lower fill factor. However, we see a four-fold increase in shunt resistance from $94 \pm 20 \text{ } \Omega\text{cm}^2$ for 450-NiO to $404 \pm 7 \text{ } \Omega\text{cm}^2$ for 600-NiO indicative of a decrease in alternate shunt pathways, or trap states.

More generally, using the DOS map in conjunction with the understanding of where charges inject and the transport mechanism can succinctly explain NiO DSSC results that previously were unclear. The low photocurrent is typically explained by a combination of fast charge recombination between holes in NiO and the reduced dye, exacerbated by a high doping level, and a resulting low charge collection efficiency.³⁹ The low V_{OC} is attributed to the close energetic placement of V_{fb} relative to the Nernst potential. However, a combination of literature reports and our results suggest that these arguments are inconsistent. First, many of the chromophores designed to physically separate the reduced dye moiety from the NiO surface still have fast charge recombination, suggesting that the recombination is not limited to surface defects.

When re-examining all of these problems with the DOS map in mind, the magnitude and energetic position of the trap state density can succinctly explain all of these problems. First, the excited state oxidative potential of P1 (1.28 V vs Ag/AgCl), and all other p-type chromophores, are such that it is energetically unfavorable to inject into the VBE and instead it is energetically favorable to inject into trap states.⁴³ Once injected, charge transport via a hopping mechanism is inefficient, particularly where ΔW_h is 0.2 eV or 1.3 eV, which is ~ 10 or ~ 100 times larger than $k_B T$ at room temperature. Additionally, the existence of OH^- species in Ni vacancies likely act as recombination centers. Both the presence of charge defects and tunneling contributes to high recombination rates and consequently low charge collection efficiencies and low photocurrents.

The Nernst potential of the I^-/I_3^- electrolyte is 0.12 V vs Ag/AgCl, meaning that there are occupied states that can directly interact with the electrolyte. This, in addition to the previously stated recombination pathways decrease the V_{OC} .

4.4 Conclusion

Here we have shown the E_f is poor approximation for the VBE in NiO due to its significant defect density which is known to move the E_f away from the band edge. Based on this reassessment, we reassigned the NiO E_f to -0.12 V vs Ag/AgCl and the VBE to ≥ 1.5 V vs Ag/AgCl, with ~ 1.5 V of filled trap states above the VBE. The trap state density is made of up two peaks, one primarily due to a Ni vacancy containing an OH^- or H_2O and the second primarily due to a Ni vacancy. The introduction of defects, particularly OH^- and H_2O increases the charge on neighboring Ni atoms to $\sim Ni^{2.3+}$. From this information, we are able to better understand the charge injection, transport and recombination properties in NiO. Specifically we see that the OH^-/H_2O defect state controls the charge recombination and both defect states, but not the VBE, take part in the charge transport through polaron hopping. This is particularly important because any effort to minimize or passivate the defects will also negatively affecting charge injection and transport, as seen from DSSC performance of 600-NiO. To move forward with improving NiO p-DSSCs it is best that DOS map are consistently reported and taken into account. We expect that DOS maps and trap state analyses will prove fruitful for understanding the differences in performance with different NiO synthetic preparations or any defect passivation method. Redesigning chromophores to inject efficiently into the VBE, as opposed to the trap state density, will likely result in more efficient devices.

4.5 Acknowledgements

We acknowledge support from the UNC Energy Frontier Research Center (EFRC) “Center for Solar Fuels”, an EFRC funded by the U.S. Department of Energy, Office of Science, Office of Basic Energy Sciences, under Award DE-SC0001011. This research made use of instrumentation at the Chapel Hill Analytical and Nanofabrication Laboratory (CHANL), a member of the North Carolina Research Triangle Nanotechnology Network (RTNN), which is supported by the National Science Foundation (NSF) (ECCS-1542015) as part of the National Nanotechnology Coordinated Infrastructure (NNCI). Special thanks to the DeSimone lab for helping with TGA and the chemistry department x-ray facility for use of the XRD.

Chapter 5: MATERIAL INFORMATICS DRIVEN DESIGN AND EXPERIMENTAL VALIDATION OF LEAD TITANATE AS AN AQUEOUS SOLAR PHOTOCATHODE

Reprinted with permission from Moot, T.; Isayev, O.; Call, R.W.; McCullough, S. M.; Zemaitis, M.; Lopez, R.; Cahoon, F. J.; Tropsha, A.; *Materials Discovery*, **2016**, (6), 9-16. Copyright Elsevier 2016

5.1 Introduction

The discovery of new materials with previously unknown or unexpected properties often leads to paradigm shifts in well-established research fields. Examples include the discovery of high-temperature superconductivity, organo-lead halide perovskite solar cells, and antibiotics^{129–131}. Historically, such discoveries have often been serendipitous, involving a combination of intuition and the Edisonian approach, because of difficulties with predicting a material's properties or reverse engineering materials with desired properties. The Edisonian approach is inefficient for exploring a broad landscape of cross-correlated parameters, and therefore, it fails to spot many unexplored materials with potentially unique properties¹³². Given the large number of feasible candidate materials, it is impossible to synthesize and evaluate all possible experimental conditions or device configurations. An analogous problem is faced by the drug industry, where computational medicinal chemistry and cheminformatics approaches rely on virtual screening of chemical libraries for rational discovery of novel bioactive compounds^{133–137}. Thus, emerging materials-informatics approaches offer an opportunity to leverage available databases and transform the serendipitous discovery process into a data- and knowledge-driven

rational design and synthesis strategy, which can accelerate the identification of materials with desired properties^{92,138–147}.

The development of solar-energy materials is an example of a challenge where a particularly stringent set of materials properties must be satisfied to achieve high solar-to-electric power-conversion efficiencies (PCEs). For the dye sensitized solar cell (DSSC) research community, a long-standing problem has been the low performance of the p-type solar cells and photocathode materials, which are needed for tandem devices^{109,148}. Typically p-type DSSCs use NiO as the photocathode, but there has not been a sustained rise in PCE above 4% since the initial report in 1999 in part due to the consistently low fill factor^{39,42,45,46,52,149}. Newer photocathodes have focused on a relatively small subset of potential semiconductors chosen primarily by their similarity in crystal structure (*e.g.* delafossites) or elemental composition (*e.g.* Cu(I))^{47–49,59,150,151}. Despite significant effort to replace NiO, thus far no candidate material has surpassed NiO in overall performance metrics.

Here, we have applied materials informatics to this problem and employed a virtual screening of ~50,000 materials representing a majority of known stoichiometric inorganic compounds. This unique computational exercise was enabled by the use of novel materials descriptors reported in our recent publication⁹⁰. We have identified PbTiO₃, which does not contain any typical features characteristic of a p-type DSSC, as the top computational “hit” material⁹⁰. Experimentally fabricated p-type DSSC devices demonstrated record fill factors when PbTiO₃ was used with an aqueous electrolyte. The success of this proof of concept study opens the door for the expansive use of materials informatics, relying on materials descriptors, for designing novel compounds with improved physical chemical properties for a wide range of applications⁹⁰.

5.2 Experimental

Details for material fingerprints and similarity search are discussed in **Methods 2.16**. PbTiO₃ film fabrication and DSSC assembly are discussed in **Methods 2.6** and **2.9**, respectively. The electrolyte consists of 1.0 M LiI and both the solvent and the amount of I₂ was varied as noted in text. Film morphology, thickness, and crystal structure were measured with SEM, profilometer, and XRD. X-ray diffraction spectra were collected from 20°-60° 2θ at a scan rate of 2° 2θ/min. TEM, STEM and EDS elemental maps were taken of the PbTiO₃ nanoparticles. Optical properties of each film were measured with an integrating sphere. Dye desorption measurements and the absorption profile of dye-loaded films in solution were measured. Macroscale pictures were taken. Fluorescence measurements were performed on dye-loaded films. EIS and Mott-Schottky analysis were done, where Mott Schottky was taken at 10 Hz and 5 Hz. Cyclic voltammograms were collected at a scan rate of 100 mV/s with a glassy carbon working electrode. For more information see **Methods 2.1, 2.11 and 2.12** DSSC performance was investigated as noted in **Methods 2.9** on 7-10 devices for each parameter, where the average active area of the devices is 0.42 ± 0.06 cm². IPCE data was taken as explained in **Methods 2.10**. A comparison of the J_{SC} values calculated from IPCE spectra and collected during 1-sun illumination is provided in **Table 5.3**. Note that the key metrics discussed, V_{OC} and fill factor, are not substantially affected by minor changes in light absorption and J_{SC} . The photovoltaic performance has not been confirmed by an independent certification laboratory. All errors and error bars represent one standard deviation.

5.3 Results and Discussion

Tracing back to the ancient “like dissolves like” principle, the concept of similarity is one of the most common rational principles of deducing new knowledge based on existing knowledge. For pharmaceuticals, this concept is predicated on the basic idea of the Similar Property Principle, which states that molecules that are structurally similar are likely to have similar properties^{152–155}. When identifying new materials with the desired property, the knowledge-driven approach would entail searching for materials with crystal structures similar to that for a known material with the same property. For materials, however, this principle is not sufficient and additional characteristics, in particular the similarity of electronic band structures, are likely to be as or more important than crystal structure similarity. In addition, quantifying similarity is another non-trivial task requiring the definition of unique characteristics (descriptors) of individual materials and the design of specific similarity metrics.

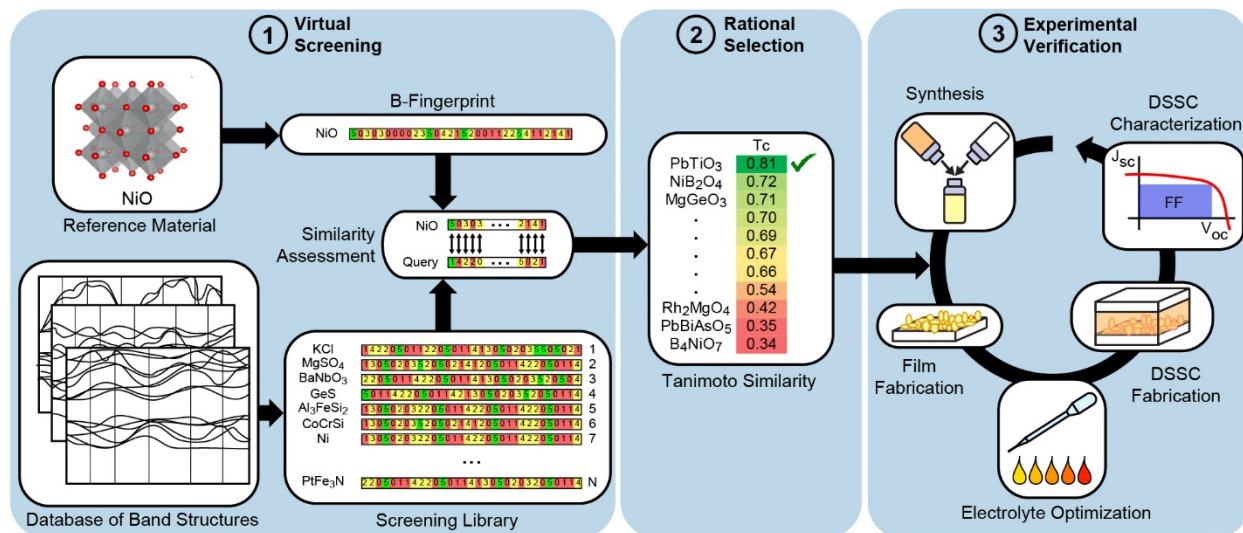


Figure 5.1. General knowledge-driven workflow. The process involves (1) virtual screening of materials using B-fingerprints for similarity assessment, (2) rational selection of top candidate materials, and (3) experimental verification through an iterative process of material synthesis, film fabrication, and electrolyte optimization to obtain the best DSSC performance characteristics.

As illustrated in Figure 5.1, we have developed a robust knowledge-driven approach for the discovery of novel p-DSSC materials using our recently-introduced materials descriptors that encode band structures (B-fingerprints)⁹⁰. In the B-fingerprint, a material's energy band diagram is discretized into 32-bit vector representations, where each Brillouin zone has a unique set of high-symmetry points that together give rise to a symmetry-dependent fingerprint (see Figure 5.2 and Methods for a detailed explanation). Known photocathodes, such as NiO or Cu₂O, were used as reference query materials; their band structures were calculated with the density functional theory (DFT) PBE functional and converted into B-fingerprints. We assume that multiple semiconductor properties that give rise to good p-type DSSC performance will be implicitly encoded within the B-fingerprint material descriptors^{156,157}. To identify new materials, we performed a virtual screening with the AFLOWLIB database of ~50,000 inorganic compounds to

identify the top three “hit” materials for each reference query (see **Appendix Table 0.1**)^{92,158}.

The similarity was assessed with the Tanimoto coefficient, T_c as described in Methods.

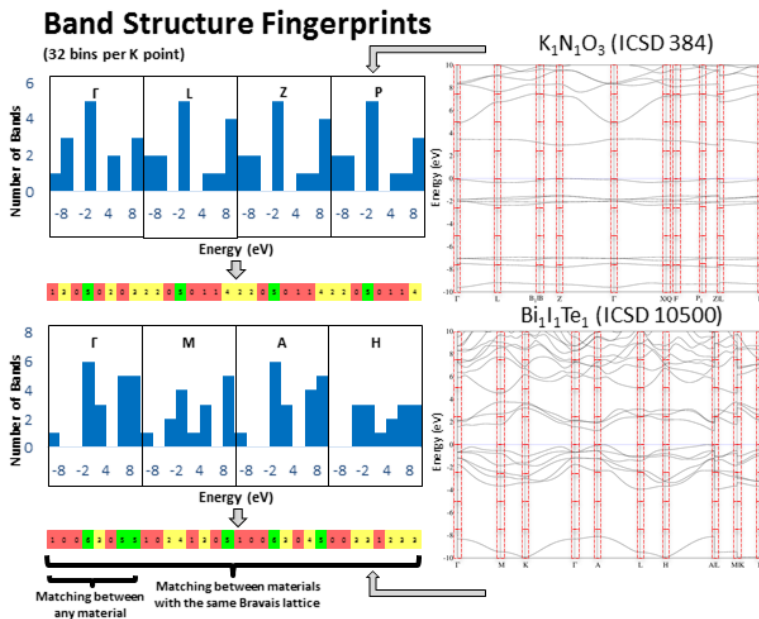


Figure 5.2. Construction of materials fingerprints from the band structure (B-fingerprints). At every high-symmetry point of the Brillouin zone (BZ), the energy band diagram (shown on the right for KNO₃ and BiTe) is discretized into 32 bins. Each bin contains a value of the number of bands that fall within its range, as shown schematically on the left. Each BZ has a unique set of high-symmetry points that combine to create the B-fingerprint. Image is adapted from ref. 4⁹⁰.

Out of the ca. 50,000 materials in the database, about 3,400 are in the acceptable range of band gap and over 1,900 have a compatible valence band edge position. Therefore, simple filtering criteria are not sufficiently selective to prioritize a single material for experimental validation. Among the twenty materials with the highest T_c values, two perovskite (BaMnO₃ and PbTiO₃) and two spinel (MnFe₂O₄ and NiCr₂O₄) materials exhibited a high degree of B-fingerprint similarity to several of the query materials. The four selected material candidates were further ranked according to the properties typically used to vet potential photocathodes: stability, synthetic feasibility, and transparent color (band gap >3 eV).

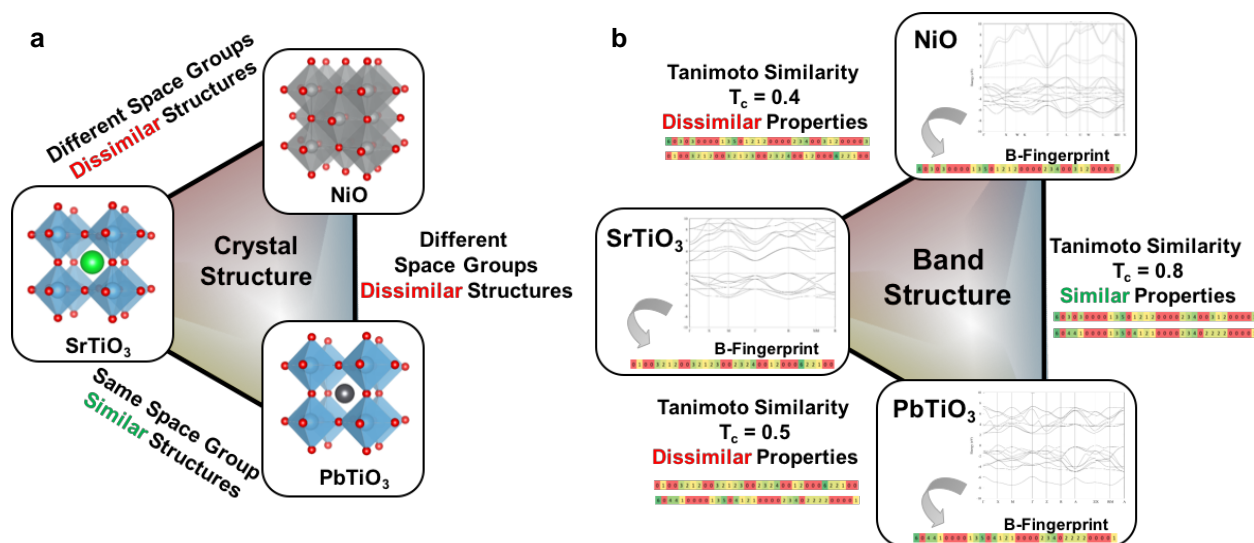


Figure 5.3. Assessment of similarity between NiO, PbTiO₃ and SrTiO₃. The comparison is based on **a**, structural geometry and **b**, electronic band structure using B-fingerprints.

As expected, the materials identified through virtual screening are similar in terms of their electronic band structure but not similar in terms of either geometric structure or elemental composition, *i.e.*, most commonly considered materials properties, as illustrated by the examples in **Figure 5.3**. For instance, PbTiO₃ and SrTiO₃ are structural analogues (**Figure 5.3 a**) with a perovskite structure; however, their electronic structure properties are dissimilar, yielding a relatively low T_c of 0.5 (**Figure 5.3 b**). In contrast, NiO and PbTiO₃ do not appear similar based on their elemental composition or crystal structure (**Figure 5.3 a**). However, they are similar by their band structure (**Figure 5.3 b**), as reflected by their relatively high T_c of 0.8.

PbTiO₃ was selected as a top choice because it was identified as the most similar to NiO among all screened materials based on B-fingerprint representation with a T_c of 0.8. No other candidates were chosen for experimental validation. Based on the DFT calculations, the valence band position of PbTiO₃ is similar to NiO (−5.02 eV vs vacuum), with a large band gap (3.96

eV). This allows for efficient hole injection from standard p-DSSC chromophores and minimal deleterious semiconductor absorption, respectively. Lead titanate is known to be a ferroelectric and have a high dielectric constant ($\epsilon \sim 200$); both of these properties have been noted as potentially beneficial for photovoltaics¹⁵⁹. In addition, the perovskite crystal structure is analogous to SrTiO₃, a well-known photoanode material, as well as the organolead materials reaching record PCEs of over 20%¹⁶⁰. Other computational studies show a high calculated hole mobility for PbTiO₃¹⁴⁶.

However, the choice of PbTiO₃ is not particularly obvious when considering all 1,900 potential candidates. Traditionally, scientists looked into materials analogous to NiO, such as 3d transition metal oxides, but with a property that is clearly advantageous. For instance, a deeper valence band position could produce a larger open-circuit voltage (V_{oc}) in DSSCs^{39,47}. Cu delafossites have recently been highlighted because they have a hybrid metal-oxygen valence band character which is favorable to hole transport⁵⁹. Finally, any new material to be used as a photocathode also requires a nanoparticle synthesis method with a low sintering temperature that will maintain a high surface area electrode for high chromophore loading and therefore a high short-circuit current density (J_{sc}).

There are no obvious markers that indicate PbTiO₃ would outperform NiO. The oxidation states of Pb and Ti make it ambiguous which metal vacancy will act as a dopant, and literature suggests a nearly intrinsic doping level, lending uncertainty as to p- or n-type behavior¹⁶¹. A comparison of crystal structures points to the well-known photoanode SrTiO₃, which requires aggressive synthetic conditions to introduce dopants¹⁶². PbTiO₃ has a similar DFT-calculated valence band edge to NiO, so there would be no improvement in V_{oc} . Finally, a high sintering temperature would limit surface area and therefore J_{sc} ¹⁶³. The lack of clear advantageous

properties, coupled with the apparent synthetic difficulty of a highly-doped, high surface area material, PbTiO_3 would not be seen as a good candidate. Thus, PbTiO_3 represents a good test case to see how materials informatics can successfully identify a non-obvious but promising new material that is worthy of continuing study. As a critical component of this approach, the similarity search in the electronic structure space allows for unique hypothesis generation and prioritization of material candidates without the typical bias arising from known structural prototypes or specific emphasized parameters.

PbTiO_3 has been widely explored for its ferroelectric properties but has not been widely investigated for solar-energy applications¹⁶⁴. A modified sol-gel synthesis (see Methods) was used to prepare white, porous, and compositionally-uniform films of PbTiO_3 on conductive glass substrates, as shown by the optical and electron microscopy images in **Figure 5.4**^{163,165–167}. The porous films are ~700 nm thick (see profilometry measurements in **Figure 5.5**) and composed of grains ~30-300 nm in size, as shown by the scanning electron microscopy (SEM) image in **Figure 5.4 a**.

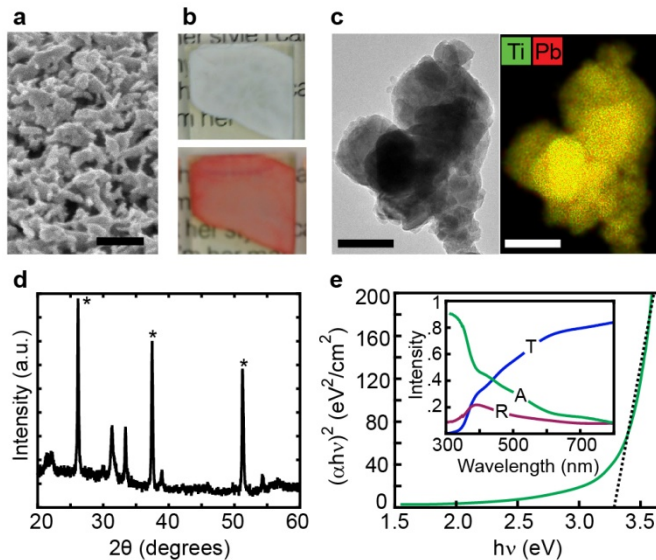


Figure 5.4. Characterization of porous PbTiO_3 films. **a**, SEM image of a PbTiO_3 film with grains 30-300 nm; scale bar: 200 nm. **b**, Photograph of a PbTiO_3 film ~ 700 nm thick on a glass slide before dye loading (upper) and after dye loading (lower) with the organic chromophore P1. **c**, TEM image (left) and EDS STEM map (right) of a nanoparticle aggregate from a PbTiO_3 film, showing Ti in green and Pb in red with a Pb:Ti ratio of 1.1:1.0; scale bar: 50 nm. **d**, XRD spectrum of PbTiO_3 on FTO glass. Peaks from FTO are denoted with *. **e**, Tauc plot for PbTiO_3 with a direct bandgap of ~ 3.3 eV. Dashed line represents a linear fit of the data. Inset: absorbance (green), reflectance (purple), and transmittance (blue) data of a PbTiO_3 film ~ 700 nm thick.

The as-deposited films visually appear white and opaque (upper image in **Figure 5.4 b**), which is consistent with scattering caused by the large size distribution of particles within the film. Transmission electron microscopy (TEM) imaging and energy dispersive x-ray spectroscopy (EDS) mapping of an agglomerate of particles (**Figure 5.4 c**) show that the material is compositionally uniform with a Pb:Ti ratio of 1.1:1.0. In addition, the x-ray diffraction (XRD) spectrum in **Figure 5.4 d** shows strong diffraction peaks consistent with perovskite crystal structure of phase-pure, crystalline PbTiO_3 ⁵⁵. Absorption data and a Tauc plot (**Figure 5.4 e**) confirm that the direct bandgap of the material is ~ 3.3 eV, similar to other literature reports⁵⁵. In order to examine the DSSC performance of PbTiO_3 , films were dye loaded

with the organic chromophore denoted P1⁶¹, yielding bright red films (lower image in **Figure 5.4 b**). A dye loading of $\sim 5 \text{ nmol/cm}^2$ (**Figure 5.6**) was measured, which is approximately one-third of that typically reported for P1 on NiO at similar film thicknesses^{43,168}.

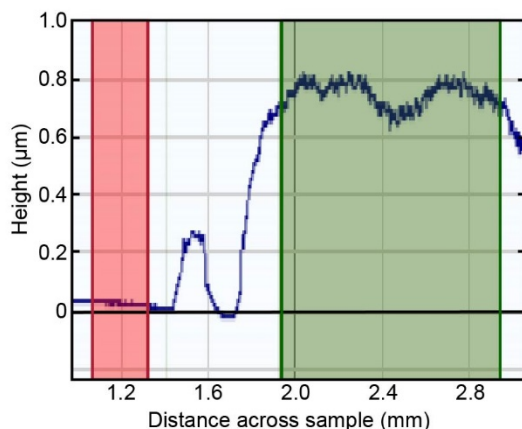


Figure 5.5. Profilometry of PbTiO_3 films. A representative profilometry cross section, where the red highlighted area denotes the clean FTO substrate and the green denotes the PbTiO_3 film edge. The height was calculated by taking the average height within the film (green highlighted region) and subtracting the average substrate height (red highlighted region).

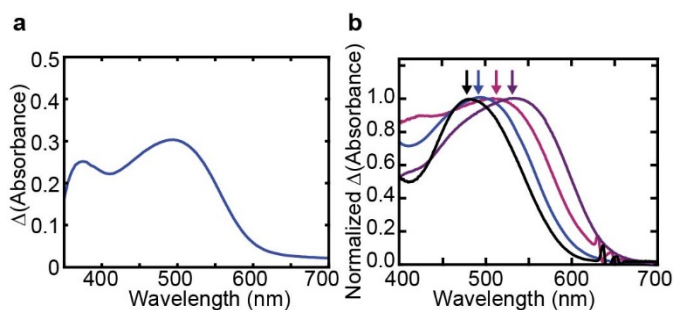


Figure 5.6. Absorbance spectra of PbTiO_3 films dye-loaded with the chromophore P1. **a.** A dye loading of 0.44 nmol/cm^2 for dense thin films and 5 nmol/cm^2 for porous films was determined, which corresponds to a dye loading 0.3Δ absorbance. **b.** Normalized difference spectra showing the absorbance profiles of P1 in acetonitrile (black), P1 loaded on film in air (blue), P1 loaded on film in water (pink), and P1 loaded on film in 100% water electrolyte solution (purple). Arrows correspond, by color, to the peak absorbance of each spectrum located at 486, 495, 508, and 532 nm.

Initial DSSC devices were fabricated with the I^-/I_3^- electrolyte in acetonitrile using 0.1 M

I₂ and 1.0 M LiI. However, the pure acetonitrile-based devices produced photoanodic current under 1-sun illumination, as shown by the current density-voltage (*J-V*) curve in **Figure 5.7 a**. This result is the opposite of our expectations based on valence band edge derived from DFT calculations. However, it is known that the semiconductor/electrolyte interface can substantially alter the effective band edge position, so we explored alternate electrolyte solutions. Acetonitrile is an aprotic solvent, but the introduction of protons can significantly shift the band edge position through protonation/deprotonation equilibrium at the interface^{65,66,169}. Thus, we introduced water into the electrolyte solution to probe the effect on device performance. Note that films in acetonitrile exhibited some desorption of dye but did not in aqueous solution, which is consistent with the limited solubility of P1 in water (**Figure 5.8**).

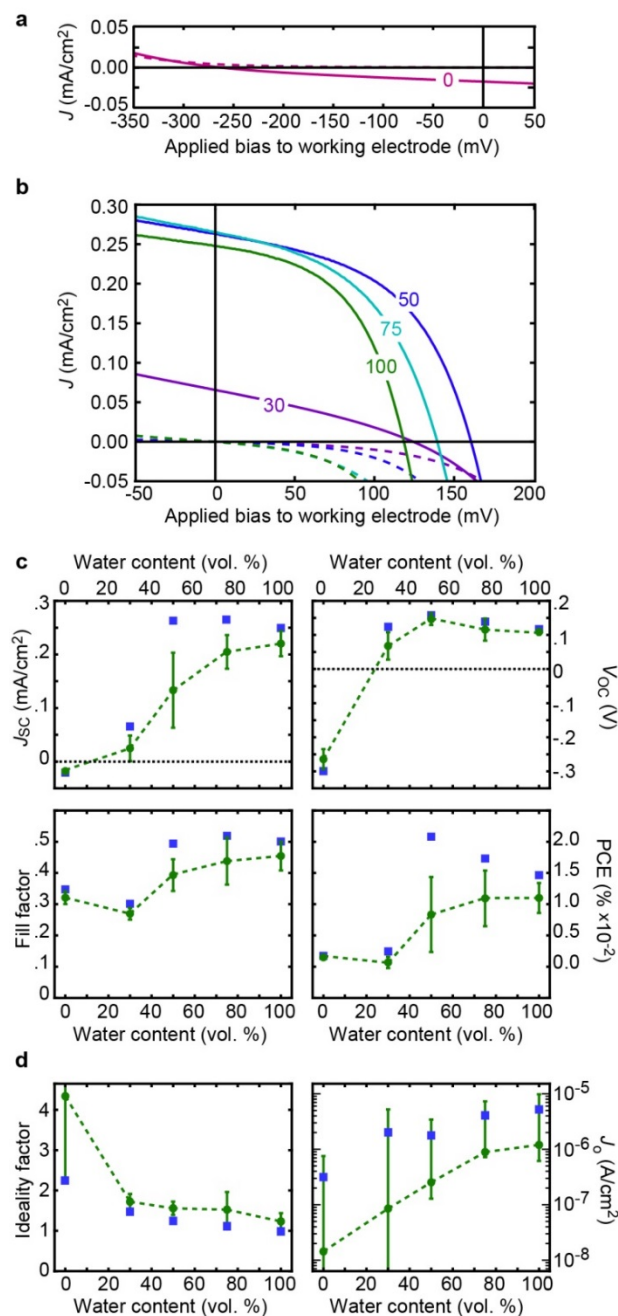


Figure 5.7. Photovoltaic characteristics of PbTiO_3 in water/acetonitrile solutions. **a**, Photoanodic J - V curves for the champion PbTiO_3 DSSC devices in an acetonitrile electrolyte solution under 1-sun illumination (solid line) and in the dark (dashed line). **b**, Photocathodic J - V curves for champion PbTiO_3 DSSC devices under 1-sun illumination (solid lines) and in the dark (dashed lines) where labels denote the volume percent water. Pink, purple, dark blue, light blue, and green curves represent 30, 50, 75, and 100 volume percent water, respectively. In panels a and b, negative J_{SC} values represent photoanodic current whereas positive J_{SC} values represent photocathodic current. **c**, Photovoltaic metrics of DSSC devices as a function of the water

content, showing the J_{SC} (upper left), V_{OC} , (upper right), fill factor (lower left), and PCE (lower right). Blue squares denote champion devices and green circles denote average values. **d**, Dark photovoltaic metrics of DSSC devices as a function of the water content, showing the ideality factor (left) and J_0 , dark saturation current, (right).

Table 5.1. Average and champion^a photovoltaic characteristics for different electrolyte water percentages. ^achampion photovoltaic characteristics correspond to the highest value for each metric, independent of device, under 1-sun illumination.

| Water % | n_0 | | J_{SC} (mA/cm ²) | V_{OC} (mV) | FF (%) | PCE (%) |
|---------|-------|----------|--------------------------------|---------------|--------------|---------------------|
| 0 | 8 | Average | -0.018 ± 0.002 | 263 ± 30 | 32.1 ± 2 | 0.0015 ± 0.0002 |
| | | Champion | -0.021 | 298 | 34.8 | 0.0019 |
| 30 | 7 | Average | 0.025 ± 0.024 | 68 ± 40 | 26.9 ± 2 | 0.0007 ± 0.0009 |
| | | Champion | 0.066 | 124 | 30.2 | 0.0025 |
| 50 | 9 | Average | 0.133 ± 0.069 | 146 ± 17 | 39.3 ± 5 | 0.0083 ± 0.0060 |
| | | Champion | 0.263 | 160 | 49.4 | 0.0208 |
| 75 | 9 | Average | 0.205 ± 0.031 | 116 ± 32 | 43.8 ± 7 | 0.0109 ± 0.0044 |
| | | Champion | 0.265 | 139 | 51.7 | 0.0174 |
| 100 | 10 | Average | 0.220 ± 0.021 | 109 ± 8 | 45.5 ± 5 | 0.0110 ± 0.0024 |
| | | Champion | 0.251 | 118 | 50.2 | 0.0146 |

Table 5.2. Average and champion^a dark curve characteristics for different electrolyte water percentages. ^a champion photovoltaic characteristics correspond to the highest value for each metric, independent of device, under 1-sun illumination.

| Water % | n_0 | | Dark Saturation Current (A/cm ²) | Ideality Factor |
|---------|-------|----------|--|-----------------|
| 0 | 8 | Average | $(3.15 \pm 4.34) \times 10^{-7}$ | 4.34 ± 2.10 |
| | | Champion | 1.44×10^{-8} | 2.10 |
| 30 | 7 | Average | $(2.02 \pm 3.21) \times 10^{-6}$ | 1.72 ± 0.19 |
| | | Champion | 8.52×10^{-8} | 1.48 |
| 50 | 9 | Average | $(1.78 \pm 1.65) \times 10^{-6}$ | 1.56 ± 0.16 |
| | | Champion | 2.54×10^{-7} | 1.25 |
| 75 | 9 | Average | $(4.03 \pm 3.31) \times 10^{-6}$ | 1.52 ± 0.44 |
| | | Champion | 8.90×10^{-7} | 1.08 |
| 100 | 10 | Average | $(5.22 \pm 4.61) \times 10^{-6}$ | 1.23 ± 0.21 |
| | | Champion | 1.20×10^{-6} | 0.99 |

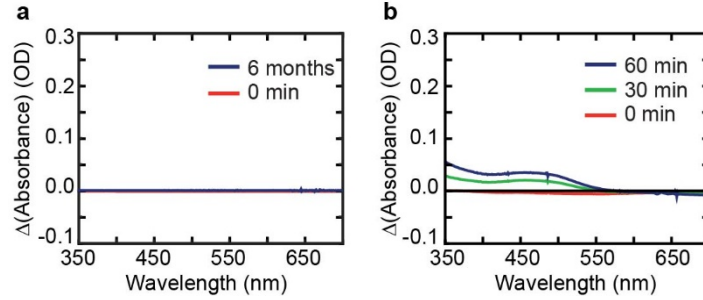


Figure 5.8. P1 chromophore desorption. **a**, Desorption spectra of P1 on PbTiO₃ in water after 0, 60 minutes, and 62 days. **b**, Desorption spectra of P1 on PbTiO₃ in acetonitrile after 0, 30, 60 minutes. Spectra were collected by placing a P1 loaded PbTiO₃ film at the bottom of a cuvette with the respective solvent and measuring the desorbed chromophore absorbance of the solution.

J-V characteristics of champion PbTiO₃ DSSC devices in the dark and under 1-sun illumination are shown in **Figure 5.7 b**, and trends in photovoltaic metrics for various ratios of acetonitrile and water are shown in **Figure 5.7 c**. All metrics are tabulated in **Tables 5.1 and 5.2**. **Figure 5.9** displays *J-V* curves characteristic of average performance, and minimal hysteresis was observed in the *J-V* curves (**Figure 5.10**). Notably, the J_{SC} changes sign between 0 and 30% water and then plateaus at 0.2-0.3 mA/cm² for 75% water and above. The V_{OC} of photocathodic devices reaches a maximum of 146 mV in 50% water and then decreases to a maximum of 109 mV in 100% water. The fill factor increases with water content, and a champion fill factor above 50% is measured for both 75% and 100% water. Finally, the increase in fill factor, coupled with the increase in J_{SC} , improves the PCE tenfold when changing from a pure acetonitrile to pure water solution.

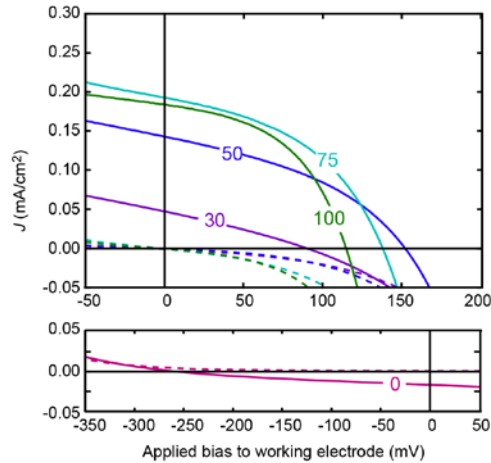


Figure 5.9. Average performance J - V curves of PbTiO_3 devices. Labels denote the vol. % water, where 0% (pure acetonitrile) is pink, 30% is purple, 50% is dark blue, 75% is light blue and 100% (pure water) is green. The average J - V curve is a single J - V curve that is most representative of the average photovoltaic metrics.

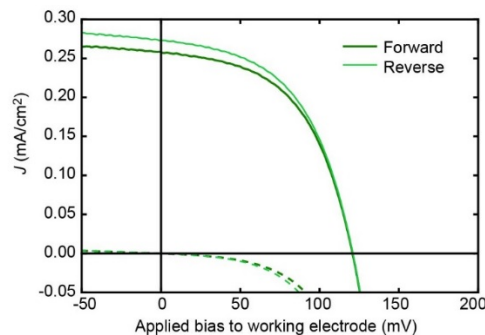


Figure 5.10. Representative J - V curve hysteresis for 100% PbTiO_3 devices. The forward bias (dark green) device performance metrics are a J_{SC} of 0.258 mA/cm^2 , V_{OC} of 121 mV , a fill factor of 53%, and a power conversion efficiency of 0.016 %. The reverse bias (light green) device performance metrics are a J_{SC} of 0.273 mA/cm^2 , V_{OC} of 121 mV , a fill factor of 51%, and a power conversion efficiency of 0.017 %. Hysteresis device metrics were not included in the average or champion performance metrics.

The change in the sign of J_{SC} upon the addition of 30% water to acetonitrile indicates shift from photoanodic to photocathodic behavior, where the cathodic behavior was maintained with increasing water percentages. Contrary to observations with TiO_2 aqueous DSSCs, PbTiO_3

devices have a higher PCE in an aqueous environment compared to acetonitrile, which is advantageous for future development of humidity-stable DSSCs and water-splitting solar fuel devices^{170,171}.

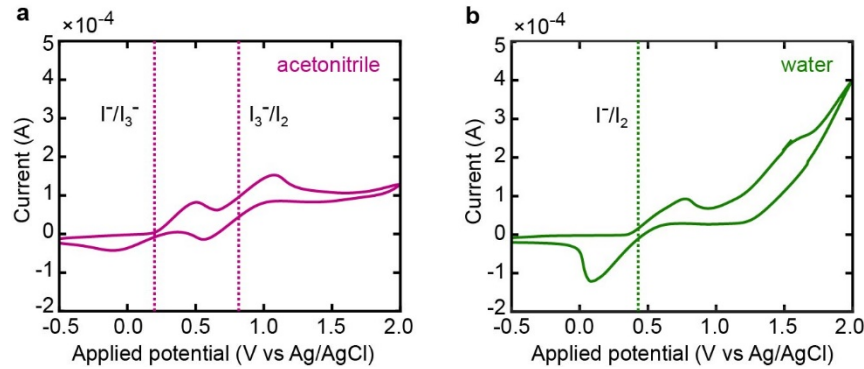


Figure 5.11. Cyclic voltammetry of the acetonitrile and water electrolyte solutions. 0.1 M I_2 and 1.0 M LiI in **a**, acetonitrile and **b**, water. The $E_{1/2}$ values (denoted by the vertical dashed lines) are 0.20 V vs Ag/AgCl (-4.89 eV) and 0.82 V vs Ag/AgCl (-5.51 eV) for acetonitrile, corresponding to the I^-/I_3^- and I_3^-/I_2 redox couples, respectively. In contrast, the single $E_{1/2}$ value is 0.43 V vs Ag/AgCl (-5.13 eV) in water and can potentially correspond to a variety of redox couples, including I^-/I_2 , I_3^-/I_2 , and I^-/I_3^- . Measured values vs Ag/AgCl were converted to values relative to vacuum by $V(eV \text{ vs vacuum}) = -((V(V \text{ vs Ag/AgCl}) + 0.197) - 4.5)$.

The V_{OC} values obtained from $PbTiO_3$ with 50% water or higher are comparable to those obtained from NiO^{149,168}. The slight decrease in V_{OC} above 50% water is correlated with an increase in the dark saturation current density J_0 (**Figure 5.7 d, right**) which is likely due to a change in the I_2/I_3^- equilibrium constant, which shifts the electrolyte Nernst potential more positive on the electrochemical scale by ~0.2 V from 0% to 100% water (**Figure 5.11**). In addition, the average ideality factor of the devices (**Figure 5.7 d, left**) decreases from 1.56 to 1.23 when moving from 50% to 100% water, which may also contribute to a decrease in V_{OC} ¹⁷¹. The high fill factors of the devices, with a champion value of 52% in 75% water, is ~50% larger than the values typically measured from NiO and is a record for p-type DSSC devices using P1

and an iodide-based electrolyte^{52,149}. The maximum theoretical fill factor, based on a V_{OC} of ~150 mV, is estimated to be ~58% (**Figure 5.12**), indicating that ~90% of the potential power is generated given the available photocurrent and photovoltage.

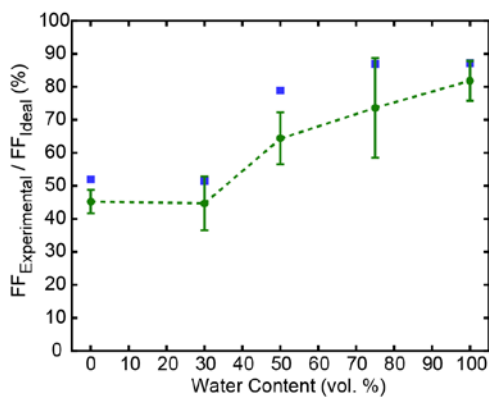


Figure 5.12. Percent of ideal fill factor. Percent of the ideal fill factor obtained at each water electrolyte concentration with champion values (blue) and average values (green; with error bars).

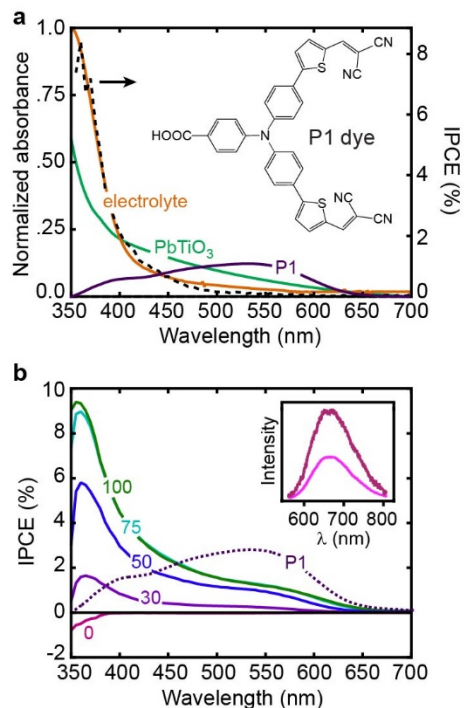


Figure 5.13. Photoresponse of dye-loaded PbTiO₃ films and devices. **a**, Left-hand axis: absorbance spectra of the PbTiO₃ film (green), the 100% water electrolyte solution (orange), and the P1 chromophore on the PbTiO₃ surface in 100% water electrolyte solution (purple). The P1 peak red shifts from 495 to 508 to 532 nm when changing between the dry state, pure water, and electrolyte solution, respectively. Values are normalized to the maximum intensity across all spectra. Right-hand axis: IPCE spectrum (dashed black line) of a solar cell device without dye in 100% water electrolyte solution. Inset: molecular structure of the P1 chromophore. **b**, IPCE spectra of DSSC devices with 0 (pink), 30 (purple), 50 (dark blue), 75 (light blue), and 100 (green) volume percent water. Dashed black line is the absorption spectrum of the P1 chromophore as shown in panel a. Inset: fluorescence signal from the P1 chromophore on glass (red) and on the PbTiO₃ film (black). The intensity is normalized to the peak absorption value of the P1 chromophore in the visible range.

The origin of the J_{SC} values and changes in J_{SC} with water content were investigated by measuring the wavelength-dependent photoresponse of the PbTiO₃ films and devices. Absorption spectra of the PbTiO₃ film, electrolyte solution, and the P1 chromophore loaded onto PbTiO₃ films are shown in **Figure 5.13 a**. An incident photon to current efficiency (IPCE) spectrum of a device without a dye in 100% water is shown as the dashed black line in **Figure**

5.13 a. The device without dye produces a J_{SC} of 0.06 mA/cm² (**Figure 5.14**) and exhibits an abruptly increasing IPCE spectrum below 400 nm that matches the absorption profile of the electrolyte. The generation of photocurrent from the electrolyte was confirmed by varying the I₂ concentration in devices, showing an increase in photocurrent with increasing I₂ concentration (**Figure 5.15**), a result that is consistent with other p-type devices^{39,149,150}.

Table 5.3. Current density values calculated from incident photon to current efficiency spectra. J_{SC} values were calculated from the reference AM1.5G spectrum and the IPCE spectra (Figure 4b) at each electrolyte water percentage. These values are compared to the J_{SC} measured under 1-sun illumination using a solar simulator equipped with an AM1.5G filter. Qualitatively, both values are in good agreement.

| Water % | J_{SC} from IPCE (mA/cm ²) | J_{SC} (mA/cm ²) |
|-----------------|--|--------------------------------|
| 0 | -0.005 | -0.018 |
| 30 | 0.050 | 0.011 |
| 50 | 0.197 | 0.140 |
| 75 | 0.292 | 0.219 |
| 100 | 0.294 | 0.251 |
| 100 (no dye) | 0.096 | 0.063 |

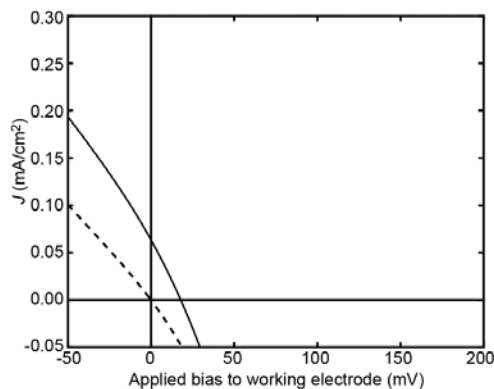


Figure 5.14. Photovoltaic characteristic of PbTiO₃ in 100% water without any chromophore.

The device performance metrics are a J_{SC} of 0.063 mA/cm^2 , V_{OC} of 18 mV , a fill factor of 27% , and a power conversion efficiency of $3.0 \times 10^{-4} \%$.

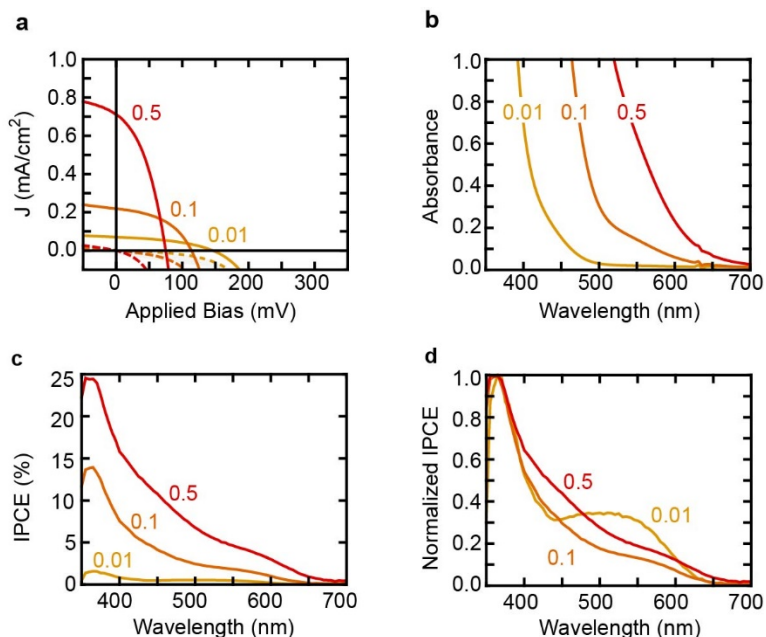


Figure 5.15. Photoactive species analysis for water electrolyte solutions with 1.0 M LiI and with 0.01 M I_2 (yellow), 0.10 M I_2 (orange), and 0.50 M I_2 (red). **a**, J - V curves for the electrolyte solutions. **b**, Absorbance spectra of the electrolyte solutions. **c**, IPCE spectra of DSSCs with each electrolyte solution. **d**, Normalized IPCE spectra of DSSCs with each electrolyte solution.

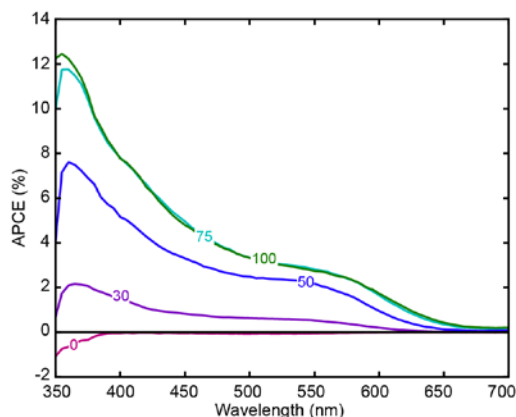


Figure 5.16. Absorbed photon to current efficiency (APCE) spectra. Labels denote the vol. % water in acetonitrile, where 0% (pure acetonitrile) is pink, 30% is purple, 50% is dark blue, 75% is light blue, and 100% (pure water) is green. Absorbance spectra of a P1 chromophore loaded onto a PbTiO_3 film in electrolyte was used for the APCE calculation.

IPCE spectra of dye-loaded films at each water percent (**Figure 5.13 b**) show substantial additional intensity in the visible range, which is consistent with the absorption profile of the P1 chromophore. We estimate that absorption by the P1 chromophore produces ~50% of the measured J_{SC} in the devices. Absorbed photon to current efficiency (APCE) spectra (**Figure 5.16**) were also calculated, with an APCE of ~4% at the P1 absorption peak of 532 nm for 100% water. To understand the origin of the low APCE values, fluorescence measurements (inset of **Figure 5.13 b**) were used to determine if the photoexcited P1 chromophore either injects holes or relaxes back to the ground state via fluorescence. On $PbTiO_3$ films, the fluorescence signal is quenched by only ~50%, which indicates that a large fraction of the photoexcited P1 dye does not inject into the valence band of $PbTiO_3$.

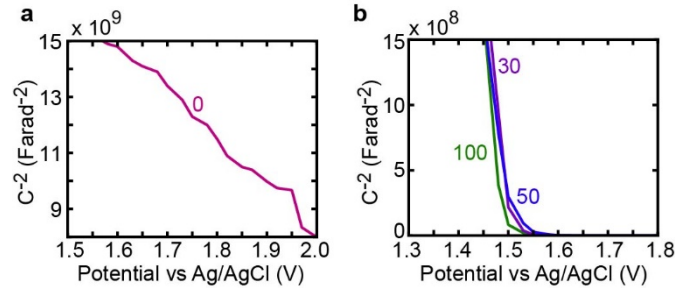


Figure 5.17. Mott-Schottky analysis of $PbTiO_3$ with various solvents in 0.1 M $LiClO_4$ solution at 5 Hz. Labels denote the vol. % water in acetonitrile, where **a**, 0% (pure acetonitrile) is pink, and **b**, 30% is purple, 50% is dark blue, and 100% (pure water) is green V_{fb} values were determined by fits to the linear regime, and measured values vs $Ag/AgCl$ were converted to values relative to vacuum by $V_{fb}(eV \text{ vs vacuum}) = -((V_{fb}(V \text{ vs } Ag/AgCl) + 0.197) - 4.5)$. We note that the solvent window of acetonitrile prohibited the exact V_{fb} from being measured for 0%. The average doping level was calculated to be $2 \pm 2 \times 10^{20} \text{ cm}^{-3}$.

To understand the low injection yield into $PbTiO_3$, we measured the flatband potential (V_{fb}) in various solvent ratios by Mott-Schottky analysis (**Figure 5.17**). The V_{fb} was used to estimate the conduction and valence band edges, as shown in **Figure 5.18 a**. A significant shift

of V_{fb} by more than 0.5 eV, from >2 V in pure acetonitrile to 1.51 ± 0.01 V vs Ag/AgCl in 30% water, is observed, after which the further addition of water has little impact on V_{fb} . As expected, the more positive electrochemical potential in pure acetonitrile is favorable for electron injection whereas the more negative V_{fb} upon addition of water is more favorable for hole injection. However, the oxidative potential of the P1 excited state still has relatively minimal overlap with the valence band of $PbTiO_3$ even in pure water. Thus, we would expect the rate of hole transfer to the valence band to be slow, which is consistent with the observed fluorescence of P1 and the low J_{SC} and APCE values¹⁷².

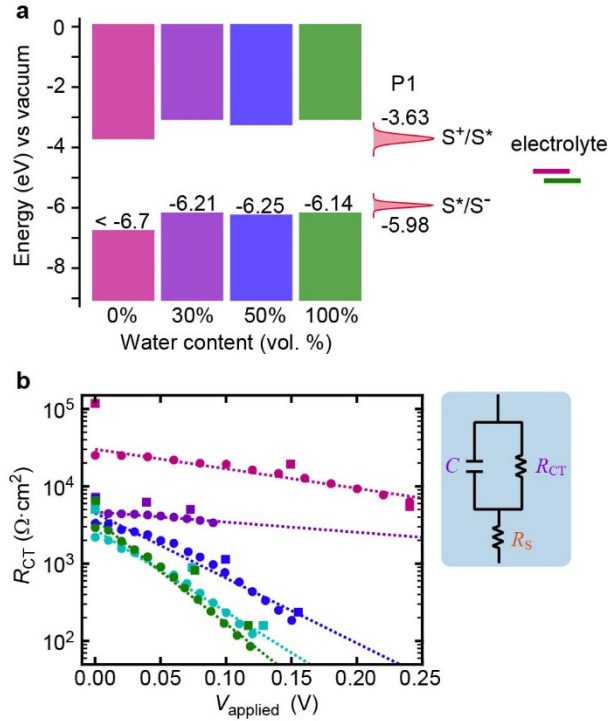


Figure 5.18. Analysis of the PbTiO₃ DSSC performance. **a**, Left: schematic of the conduction and valence band edges of PbTiO₃ as a function of water content as estimated by averaging 10 Hz and 5 Hz V_{fb} from Mott-Schottky analysis, which is approximated as the valence band edge. Middle: oxidation and reduction potentials, with Gaussian linewidths, of the P1 chromophore as measured in acetonitrile solution⁴³. Right: Nernstian potential for the redox couple in acetonitrile (pink) and water (green). All values are reported relative to the vacuum level. **b**, Charge-transfer resistance, R_{CT} , as a function of applied potential as determined by EIS (squares) and by the differential resistance of J - V curves (circles) for 0 (pink), 30 (purple), 50 (dark blue), 75 (light blue), and 100 (green) volume percent water. The simplified Randles circuit used to model EIS data is shown on the right, including R_{CT} , interfacial capacitance C , and series resistance R_s .

Similarly large shifts in the V_{fb} of TiO₂ in water have been observed and explained by the protonation/deprotonation equilibrium at the semiconductor surface^{66,169}. Consequently, the addition of water affects the protonation/deprotonation equilibrium on the surface of PbTiO₃ and shifts the V_{fb} . Previous reports on Pb(Zr,Ti)O₃ solid-state devices have reported a shift from anodic to cathodic performance, which was postulated to be a result of the ferroelectric surface¹⁶¹. It should be noted that the theoretical maximum V_{OC} from these V_{fb} is ~ 1 V, despite

the experimental V_{OC} of ~ 150 mV. This difference cannot be explained by the dark saturation currents (**Figure 5.7 d**), which are reasonably low at $\sim 5 \times 10^{-6}$ A/cm² (**Table 5.2**) in all solvents¹⁴⁹. We suspect that the low photocurrent as well as the large difference between the work function of the metallic back contact and the V_{fb} of PbTiO₃ may play a role in diminishing the V_{OC} , as is commonly seen in organic photovoltaic devices¹⁷³.

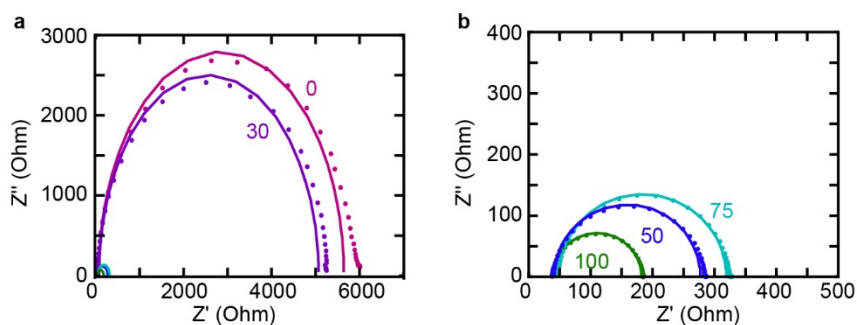


Figure 5.19. Electrochemical impedance spectroscopy (EIS) measurements of DSSC devices at V_{OC} under 1-sun illumination. Marker symbols correspond to raw data and solid lines correspond to a fit to the simplified Randles circuit for **a**, 0% (pink) and 30% (purple) water **b**, 50 % (dark blue), 75 % (light blue) and 100% (green) water electrolyte solutions.

Table 5.4. Electrochemical impedance spectroscopy extracted parameters using a simplified Randles model. Measurements were taken at the noted bias voltage under one sun illumination.

| Water % | Applied Bias (V) | R_{CT} (Ω cm ²) | R_S (Ω cm ²) | Capacitance (F) |
|---------|------------------|---------------------------------------|------------------------------------|-----------------------------------|
| 0 | 0 | $(4.23 \pm 0.452) \times 10^4$ | 191 ± 43 | $(2.77 \pm 0.021) \times 10^{-6}$ |
| | 0.150 | $(7.06 \pm 0.074) \times 10^3$ | 41 ± 6 | $(2.51 \pm 0.018) \times 10^{-6}$ |
| | 0.240 | $(2.01 \pm 0.017) \times 10^3$ | 25 ± 2 | $(2.39 \pm 0.018) \times 10^{-6}$ |
| 30 | 0 | $(2.96 \pm 0.025) \times 10^3$ | 25 ± 2 | $(3.18 \pm 0.021) \times 10^{-6}$ |
| | 0.040 | $(2.49 \pm 0.025) \times 10^3$ | 51 ± 7 | $(3.29 \pm 0.034) \times 10^{-6}$ |
| | 0.073 | $(1.99 \pm 0.016) \times 10^3$ | 30 ± 3 | $(3.13 \pm 0.025) \times 10^{-6}$ |
| 50 | 0 | $(2.29 \pm 0.025) \times 10^3$ | 39 ± 3 | $(2.42 \pm 0.019) \times 10^{-6}$ |
| | 0.100 | $(3.64 \pm 0.034) \times 10^2$ | 17 ± 1 | $(2.10 \pm 0.018) \times 10^{-6}$ |
| | 0.155 | $(7.52 \pm 0.070) \times 10^1$ | 13 ± 0.1 | $(1.87 \pm 0.020) \times 10^{-6}$ |
| 75 | 0 | $(1.71 \pm 0.017) \times 10^3$ | 28 ± 3 | $(2.26 \pm 0.019) \times 10^{-6}$ |
| | 0.075 | $(3.82 \pm 0.036) \times 10^2$ | 19 ± 1 | $(2.07 \pm 0.018) \times 10^{-6}$ |
| | 0.130 | $(7.68 \pm 0.079) \times 10^1$ | 18 ± 0.2 | $(1.97 \pm 0.027) \times 10^{-6}$ |
| 100 | 0 | $(2.14 \pm 0.022) \times 10^3$ | 27 ± 2 | $(2.28 \pm 0.017) \times 10^{-6}$ |
| | 0.075 | $(2.55 \pm 0.022) \times 10^2$ | 17 ± 0.4 | $(2.09 \pm 0.018) \times 10^{-6}$ |
| | 0.122 | $(5.11 \pm 0.054) \times 10^1$ | 16 ± 0.2 | $(2.06 \pm 0.030) \times 10^{-6}$ |

Table 5.5. Beta values calculated from differential resistance values versus applied bias. Differential resistance values were calculated from JV curves that were representative of average performance at each electrolyte water percentages.

| Water % | β |
|---------|-----------------|
| 0 | 0.15 ± 0.01 |
| 30 | 0.08 ± 0.01 |
| 50 | 0.50 ± 0.03 |
| 75 | 0.63 ± 0.02 |
| 100 | 0.80 ± 0.02 |

The change in V_{fb} explains the shift from anodic to cathodic performance but does not fully explain the improved overall performance in water over acetonitrile. We hypothesize that large changes in the diffuse double layer and dynamics at the semiconductor/electrolyte interface

are likely the main causes of increased performance. To further explore this interface, we performed electrochemical impedance spectroscopy (EIS) of DSSC devices (**Figure 5.19**). If interpreted using a simplified Randles circuit (**Figure 5.18 b**), the EIS data indicates there is no substantial change in the series resistance, R_S , but a large change in charge-transfer resistance, R_{CT} , at the semiconductor-solution interface upon the addition of water (see **Table 5.4**). The recombination differential resistance, R_{rec} , of the devices, calculated as $(dJ/dV)^{-1}$, is in good agreement with R_{CT} , as shown by the similarity of the data in **Figure 5.18 b**, indicating $R_{rec} \approx R_{CT}$. R_{rec} shows an exponential dependence on applied voltage and can be fit as¹⁷⁴:

$$R_{rec} = R_o \exp(-q\beta V/k_B T) \quad (5.1)$$

where β is the recombination coefficient, R_o is a pre-exponential term related to J_o , k_B is the Boltzmann constant, q is elementary charge, and T is temperature. β increases from 0.15 at 0% water to 0.80 in 100% water (**Table 5.5**), which corresponds well to the previously measured ideality factors, where $\beta = 1/n$ ¹⁷⁴. The increase in β with increasing water concentration suggests a substantial change in the mechanism of recombination at the semiconductor-solution interface and could indicate a decreased role of trap states above the valence band edge¹⁷⁴. The results highlight the significant role of the interface in determining device performance, and additional investigation will be necessary to elucidate the details of the novel PbTiO₃-water system for high-performance DSSC devices¹⁷⁵.

5.4 Conclusions

The unique performance features of PbTiO₃ p-type DSSCs give rise to many interesting questions about the role of solvent and the semiconductor-electrolyte interface as well as the role of a high dielectric constant, and related ferroelectricity, as an important material property. The

results also point to the need for design and synthesis of chromophores with higher oxidative potentials than P1, which would likely dramatically improve the J_{SC} of $PbTiO_3$ devices and thus the overall PCE. Beyond these specific questions, this work highlights the utility of material informatics approaches to both identify important semiconductor properties and prioritize previously unexplored materials for experimental studies. This proof-of-concept discovery of a novel DSSC material illustrates the power of materials descriptors that enable the application of the virtual screening approach for rapid and effective identification of diverse materials in large databases with properties similar to those of a query. Potentially, the same approach can be used for different DSSC components, such as the chromophore, to ultimately, design each component of the device. In sum, this approach could allow for expedited design of each device component for a highly optimized DSSC. We hope that this investigation will help establishing materials informatics as a common tool to accelerate the design and discovery of novel functional materials with the desired performance characteristics.

5.5 Acknowledgements

A.T. acknowledges support from DOD-ONR (N00014-16-1-2311) for the computational studies reported in this paper. Development of the web service (O.I.) was supported by the Russian Scientific Foundation (No. 14-43-00024). T.M., R.W.C, S.M.M, M.E.Z., C.J.F., R.L. and J.F.C. acknowledge support for all of the experimental studies on $PbTiO_3$ by the UNC Energy Frontier Research Center (EFRC) “Center for Solar Fuels,” an EFRC funded by the U.S. Department of Energy, Office of Science, Office of Basic Energy Sciences, under Award DE-SC0001011. This research made use of instrumentation at the Chapel Hill Analytical and Nanofabrication Laboratory (CHANL), a member of the North Carolina Research Triangle Nanotechnology Network (RTNN), which is supported by the National Science Foundation

(NSF) (ECCS-1542015) as part of the National Nanotechnology Coordinated Infrastructure (NNCI). We thank J. R. McBride for TEM imaging using instrumentation supported by NSF grant EPS-1004083 (TN-SCORE). We acknowledge the UNC ITS Research Computing Center for access to the KillDevil cluster for computational studies. O.I. also acknowledges computational resources provided by Extreme Science and Engineering Discovery Environment (XSEDE) program, which is supported by NSF grant number ACI-1053575.

Chapter 6: THE BENEFICIAL ROLE OF IODINE ON INTERFACE RECOMBINATION IN P-TYPE DYE SENSITIZED SOLAR CELLS AND ITS IMPLICATIONS FOR AQUEOUS ELECTROLYTES

To be submitted by: Moot, T.; McCullough, S. M.; Taggart, Lopez, R.; Cahoon, J. F.

6.1 Introduction

Despite extensive research into improving the efficiencies of p-type dye sensitized solar cells (DSSCs), the power conversion efficiencies (PCE) still lag significantly behind the n-type DSSC counterparts by nearly an order of magnitude.^{46,50,51} This is important for solar energy production in general, but is of particular relevance due to the necessity of a high performance photocathode side to realize any tandem device for solar fuel production such as a dye sensitized photoelectrosynthesis cell (DSPEC).³⁴ There are three main components to the dye sensitized solar cell: the semiconductor, the chromophore and the electrolyte, which all must work efficiently in concert.⁴⁰ The chromophore must absorb visible light and quickly transfer a hole into the semiconductor and then transfer the electron to the electrolyte. The semiconductor and electrolyte must be able to efficiently transport charges away from the interface to the back contacts to complete the circuit. Additionally, the semiconductor and electrolyte should not have other recombination pathways that complicate the expected charge transfer processes.⁴⁰ In reality, these additional recombination pathways prove to be a significant problem in p-DSSCs.^{52,115}

Standard p-DSSC devices typically have fill factors of $\leq 40\%$ as compared to $\sim 60\%$ for n-DSSCs and achieve photocurrents $\sim 1/10^{\text{th}}$ of those reached in n-DSSCs.^{51,52,74} The low photocurrent and fill factor in p-DSSCs is due to various recombination pathways, either

between the semiconductor and chromophore or electrolyte.⁵² To minimize these recombination pathways, the majority of research efforts have been focused on designing novel photocathodes and novel chromophores.^{49,60} Many promising materials, such as the delafossites, have been studied, however nearly all devices result in similarly low fill factors and low photocurrents.^{44,49,150,176} Chromophores designed to physically separate the electron and hole to minimize recombination have shown improvements over more conventional chromophores, but the hole lifetime is still an order of magnitude less than that of electrons in n-DSSCs.^{38,45,114} This suggests that there is another component to the DSSC that is affecting the recombination rates more than either the semiconductor or the chromophore and is obfuscating much of the expected improvements.

The electrolyte comprises of a cation, such as Li^+ , iodine species, I^- , I_3^- and I_2 , which result in 7 separate redox couples, and possibly various additives.⁶⁷ The role of each electrolyte component has been intensely studied in the context of n-DSSCs. Different cations from the iodine salt have been shown to control the band edge position, affecting recombination kinetics and injection efficiencies.^{66,177} The solvent affects the I^-/I_3^- equilibrium constant which affects the equilibrium concentrations within solution, affecting recombination.⁶⁵ It is generally accepted that in n-DSSCs I^- regenerates the oxidized chromophore via hole scavenging.⁶⁷ Recent work in n-DSSCs demonstrates that the main recombination pathway is through the electron scavenger I_2 , although it was previously believed to be I_3^- .⁶⁸ Within the n-DSSC the equilibrium concentrations of a standard 1.0 M/0.1 M iodide/triiodide electrolyte are 0.9 M I^- , 0.1 M I_3^- and 10^{-8} M I_2 , minimizing opportunity for electron scavenging from I_2 and thus recombination. Importantly, any electrolyte additives, such as guanidinium thiocyanate (GuSCN), minimize recombination pathways between the chromophore and the electrolyte.⁷⁰ In fact, an in depth

analysis of n-DSSC performance suggests that the largest improvements in PCE come from changes in the electrolyte, particularly inclusion of the additives.^{178,179}

Despite this impact, there has been little to no analysis of the electrolyte with respect to the p-DSSC. In an ideal electrolyte for p-DSSCs, there would be ample opportunity for electron scavenging and minimal opportunity for hole scavenging. Designing the appropriate electrolyte to realize this ideal would likely affect the recombination rates significantly and thus improve device performance. We hypothesize that the electrolyte, specifically I₂, significantly affects recombination in p-DSSCs. To begin to understand the effect of electrolyte on p-DSSC performance, we probe the role of I₂ on device performance. We hypothesize that by increasing concentrations of I₂ will enable efficient dye regeneration, thereby turning off major recombination pathways from the chromophore to the semiconductor or the electrolyte and increase p-DSSC device PCE. This also suggests that an aqueous electrolyte would be advantageous for p-DSSCs because the I⁻/I₃⁻ equilibrium constant (K_{eq}) for I⁻ + I₂ → I₃⁻ is 7.5 x 10² M⁻¹ in water (H₂O) whereas K_{eq} is 5 x 10⁶ M⁻¹ in acetonitrile (MeCN), favoring a larger equilibrium concentration of I₂ (I₂]_{eq}) in water.

6.2 Experimental

PbTiO₃, NiO and TAD Al NiO film fabrication and DSSC assembly are discussed in **Methods 2.6, 2.7 and 2.9**, respectively. For experimental details on *J-V* curves, IPCE, EIS and Cyclic voltammograms, see **Methods 2.9, 2.10, 2.11 and 2.12**.

6.3 Results and Discussion

To probe the effect of the electrolyte on device performance, lead titanate (PbTiO₃) was chosen because of its previously reported ideal diode like behavior and minimal recombination pathways culminating in a record fill factor of 48%.¹⁷⁶ Three different electrolytes were used to

probe the effect of I_2 on p-DSSC performance. The first electrolyte (standard) is comprised of 1.0 M LiI and 0.1 M I_2 which results in an $[I_2]_{eq}$ of 4×10^{-8} . To modulate $[I_2]_{eq}$ two different methods were used: modifying the starting LiI: I_2 ratio and modifying the solvent. The second electrolyte (high $[I_2]_{eq}$) modulates the starting LiI: I_2 ratio to 0.55 M LiI, 0.55 I_2 which produces an $[I_2]_{eq}$ of 4×10^{-4} . The third electrolyte (aqueous) modulates the solvent to an aqueous 1.0 M LiI and 0.1 M I_2 electrolyte, which results in an $[I_2]_{eq}$ of 4×10^{-4} . All of the starting and equilibrium concentrations are summarized in **Table 6.1**. For the standard and high $[I_2]_{eq}$ electrolytes a solvent system of 1:1 MeCN:H₂O was used to appropriately shift the flatband potential (V_{fb}) of PbTiO₃ to allow for hole injection from the chromophore P1.¹⁷⁶

Table 6.1. Electrolyte compositions in the initial concentrations and the calculated concentrations at equilibrium (equilib.).

| | Standard | High $[I_2]_{eq}$ | Aqueous |
|------------------------|--------------------|--------------------|--------------------|
| Initial [LiI] (M) | 1.0 | 0.55 | 1.0 |
| Initial $[I_2]$ (M) | 0.1 | 0.55 | 0.1 |
| Equilib. $[I^-]$ (M) | 0.9 | 5×10^{-4} | 0.9 |
| Equilib. $[I_3^-]$ (M) | 0.1 | 0.55 | 0.1 |
| Equilib. $[I_2]$ (M) | 2×10^{-8} | 5×10^{-5} | 2×10^{-4} |

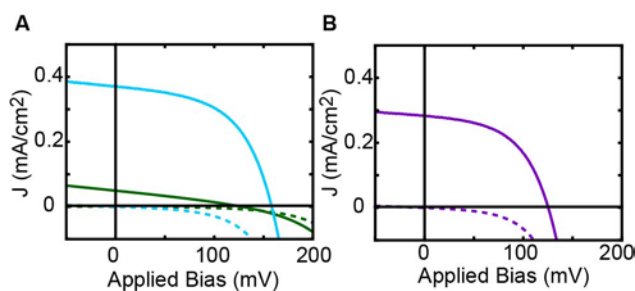


Figure 6.1: Average p-DSSC J - V curves of PbTiO₃ under one-sun illumination (solid) and in the dark (dashed) using an **A**) standard (green), high $[I_2]_{eq}$ (blue), and **B**) aqueous (purple) electrolyte.

The average current density-voltage (J - V) curves in the three electrolyte systems are shown in **Figure 6.1** and the device parameters are summarized in **Table 6.2**. Upon increasing the $[I_2]_{eq}$, either by using the aqueous or high $[I_2]_{eq}$ electrolyte, the fill factor increases from an average of 28.2 % to 51.3 – 52.2 %. The short circuit current density (J_{SC}) increases with an increase in $[I_2]_{eq}$, where the high $[I_2]_{eq}$ electrolyte device has a J_{SC} of 0.38 mA/cm² and the aqueous electrolyte has a J_{SC} of 0.28 mA/cm², two orders of magnitude higher than the average J_{SC} of 0.05 mA/cm² obtained in the standard electrolyte . The open circuit voltage (V_{OC}) varied by approximately 20 mV, although it is likely due to the shift the Nernst potential.^{67,176} The Nernst potential for the standard electrolyte is 0.12 V vs Ag/AgCl whereas the Nernst potential for the high $[I_2]_{eq}$ and aqueous electrolyte are at 0.21 V vs Ag/AgCl and 0.4 V vs Ag/AgCl, respectively. There is an increase in the power conversion efficiency (PCE) of 10.6 – 16.7 x upon increasing the $[I_2]_{eq}$, driven by the improvement in the fill factor and J_{SC} .

Table 6.2: Average PbTiO₃ p-DSSC device performance metrics

| | Standard | High $[I_2]_{eq}$ | Aqueous |
|---|-------------|-------------------|-------------|
| J_{SC} (no dye) (mA/cm ²) | 0.10 ± 0.02 | 0.21 ± 0.06 | 0.14 ± 0.02 |
| J_{SC} (mA/cm ²) | 0.05 ± 0.01 | 0.38 ± 0.04 | 0.28 ± 0.03 |
| V_{OC} (mV) | 120 ± 12 | 145 ± 9 | 128 ± 2 |
| FF (%) | 28.2 ± 1.1 | 52.2 ± 1.2 | 51.3 ± 2.3 |
| PCE x 10 ⁻² (%) | 0.17 ± 0.05 | 2.89 ± 0.03 | 1.84 ± 0.02 |
| R_{sh} (Ω•cm ²) | 2920 ± 322 | 2506 ± 674 | 3275 ± 567 |
| R_s (Ω•cm ²) | 1763 ± 390 | 78 ± 5 | 104 ± 17 |

To understand the origin of the differences in J_{SC} , incident photon to current efficiencies (IPCE) were measured for each electrolyte system (**Figure 6.2 A,B**) where the IPCE of the P1

chromophore was monitored at the absorption maximum at 535 nm. All of the chromophore IPCE values are low, due to the energetic misalignment between PbTiO_3 V_{fb} and the chromophore which does not allow for efficient injection.^{43,176} Regardless, there is a 1.5 x increase in IPCE when switching from the standard to the high $[\text{I}_2]_{\text{eq}}$ electrolyte and a 2.6 x increase in IPCE when comparing the standard to aqueous electrolyte. Since the chromophore loading is constant across all systems any increase in IPCE is due to an increase in the absorbed photon to current efficiency (APCE), suggesting that the chromophore is more efficiently injecting holes into the photocathode-achieved simply by modulating the $[\text{I}_2]_{\text{eq}}$. However, it should also be noted that in all electrolyte systems the electrolyte contributes significantly to the J_{SC} via hole injection from I_3^- , as is commonly noted for p-DSSCs.^{40,63,74,150,176} To quantify the contribution of the electrolyte to the J_{SC} , devices without any chromophore were fabricated using each of the three electrolyte systems and the resulting J - V and IPCE curves were measured (**Figure 6.3**). In each case, the electrolyte injection accounted for approximately half of the total J_{SC} , indicating that the increase in J_{SC} obtained with the high $[\text{I}_2]_{\text{eq}}$ electrolyte was ~ 45 – 51 % due to an increase in chromophore IPCE.

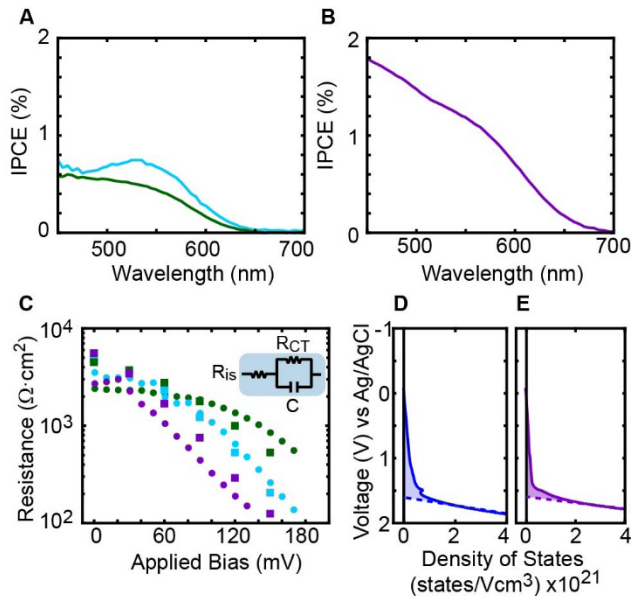


Figure 6.2. PbTiO_3 p-DSSC performance mechanism. IPCE spectra of the chromophore for an average device with an **A**) standard (green), high $[\text{I}_2]_{\text{eq}}$ (blue), and **B**) aqueous (purple) electrolyte. The IPCE spectra is obtained by measuring the IPCE of a device with and without P1 and subtracting the contribution from the electrolyte. **C**) Device resistance (circles) and charge transfer resistances (squares) of an average device with a standard (green), high $[\text{I}_2]_{\text{eq}}$ (blue), and aqueous (purple) electrolyte. Density of states of PbTiO_3 in **D**) 1:1 MeCN: H_2O and **E**) NiO water where the dashed line is an approximation of the valence band edge and the shaded area denotes the trap state density.

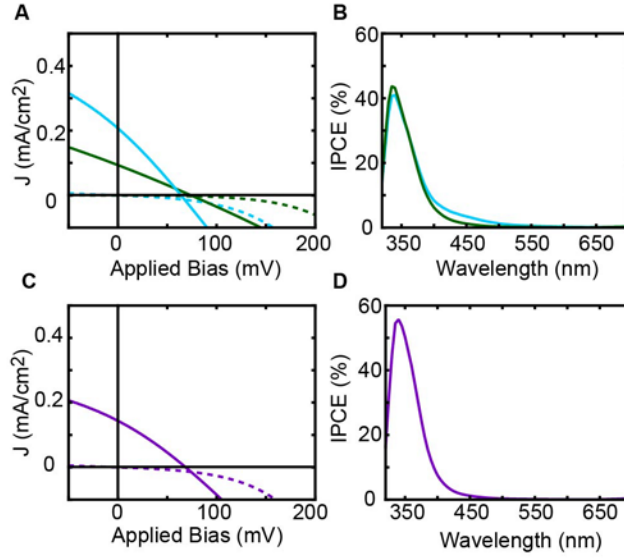


Figure 6.3: Average PbTiO₃ p-DSSCs fabricated without any chromophore. **A, C**) J - V curves under one-sun illumination (solid) and in the dark (dashed) **B, D**) IPCE curves, all using either a standard (green), high $[I_2]_{eq}$ (blue), and aqueous (purple) electrolyte.

The fill factor had the largest improvement in any device performance metric upon increasing the $[I_2]_{eq}$. The fill factor for any photovoltaic is affected by the series resistance (R_s) and the shunt resistance (R_{sh}). Upon increasing the $[I_2]_{eq}$, R_{sh} does not change with any trend, and all values are reasonably high at around $2000 \Omega \cdot cm^2$. However, R_s consistently decreases with increasing $[I_2]_{eq}$ from $1763 \Omega \cdot cm^2$ to $73 \Omega \cdot cm^2$ and $103 \Omega \cdot cm^2$ for the standard, high $[I_2]_{eq}$ and aqueous electrolyte, respectively. R_s can decrease the fill factor by:

$$FF_s = FF_0(1 - 1.1r_s) + \frac{r_s^2}{5.4} \quad (6.1)$$

where FF_0 is the fill factor without any shunt resistance and r_s is the normalized series resistance, which are equal to R_s divided by the characteristic resistance of the photovoltaic device. The drop in R_s accounts for 60-75% of the fill factor improvement between the standard and high $[I_2]_{eq}$ electrolyte.

Any device resistance (R_{dc}) can be further separated into an interfacial series resistance (R_{is}) and a charge transfer resistance (R_{CT}) (**Figure 6.2 C**) using electrochemical impedance spectroscopy (EIS).^{52,174} R_{CT} at V_{OC} is an approximation of the R_{CT} of device R_s and decreases significantly from $535 \Omega \cdot \text{cm}^2$ to $204 \Omega \cdot \text{cm}^2$ and $125 \Omega \cdot \text{cm}^2$ for the standard, high $[I_2]_{eq}$ and aqueous electrolyte. This decrease in R_{CT} is the origin of the decrease in R_s . Additionally, a measure of the amount of states available for recombination, β , can be calculated from the slope of the resistance versus applied bias, where 1 is ideal.¹⁷⁴ β , is calculated to improve from 0.20 to 0.49 to 0.64 for the standard, high $[I_2]_{eq}$ and aqueous electrolyte, respectively. Typically, β is discussed in terms of semiconductor trap states, thus the density of states of PbTiO_3 was measured in both 1:1 MeCN:H₂O and in water to determine if the change in solvent is affecting the trap state density. Although there are slight changes in the shape of the trap states (**Figure 6.2 D,E**), the trap state density is approximately constant at 3.26×10^{20} states/cm³ and 3.83×10^{20} states/cm³. This suggests that the number states available for recombination is not based on the semiconductor trap state density and is likely due to electrolyte-chromophore recombination pathways.

Mechanistically, improvement in fill factor and any improvement in J_{SC} upon increasing $[I_2]_{eq}$ both stem from a decrease in R_s , which is primarily due to a decrease in R_{CT} . The decrease in R_{CT} likely allows for increased electron transfer from the reduced chromophore to the electrolyte, catalyzed by the higher $[I_2]_{eq}$, which is a potent electron scavenger.⁶⁸ This allows for faster chromophore regeneration which improves the IPCE, and consequently the J_{SC} , and minimizes alternate recombination pathways between the excited state chromophore and the electrolyte or semiconductor. This is further supported by the increase in β which suggests that the increase in $[I_2]_{eq}$ minimizes the efficacy of other potential interface recombination sites.

We expect that the improvement in J_{SC} and fill factor resulting from an increased $[I_2]_{eq}$, or more generally an increase in the concentration of the given electron scavenger, would be applicable to any photocathode system. To probe the generality of this electrolyte design, two photocathode systems were used: the standard NiO and targeted atomic deposition of aluminum (TAD Al) NiO, which has a lower defect density.⁵⁴ The solvent for the standard and high $[I_2]_{eq}$ electrolyte is pure MeCN. To compare to literature performance of TAD Al NiO, a device with the same electrolyte was fabricated (**Figure 6.6**). We expect that TAD Al NiO will act as an intermediate between $PbTiO_3$ and NiO, in terms of ideal-like behavior due to the intermediate amount of trap state density. Additionally, the chromophore P1 can easily inject into both photocathode systems thus the effects on the J_{SC} and IPCE may be clearer than in the $PbTiO_3$ devices.^{43,54}

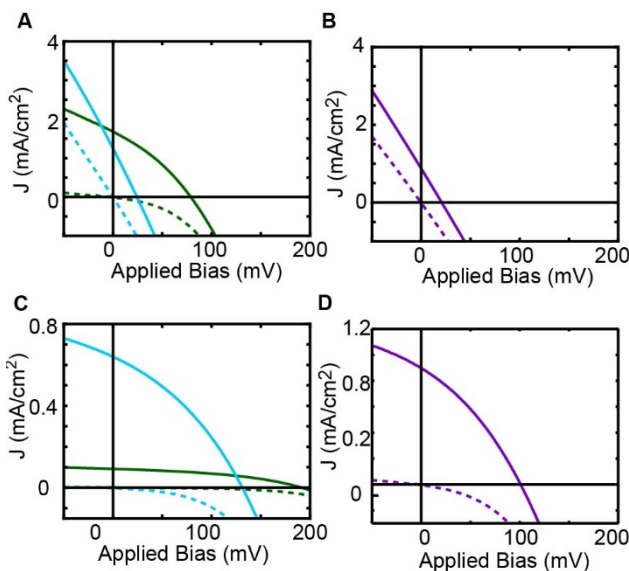


Figure 6.4: Average p-DSSC J - V curves of **A, B**) NiO and **C, D**) TAD Al NiO under one-sun illumination (solid) and in the dark (dashed) using a standard (green), high $[I_2]_{eq}$ (blue), and aqueous (purple) electrolyte.

In **Figure 6.4**, the device performance for NiO and TAD Al NiO are shown where an increase in $[I_2]_{eq}$ decreases device performance for NiO and increases device performance for

TAD Al NiO. The device performance metrics are summarized in **Table 6.3** and **6.4**. The NiO device (**Figure 6.4 A, B**) appears to be entirely shunted upon an increase in $[I_2]_{eq}$, either by using the high $[I_2]_{eq}$ or aqueous electrolyte, where the fill factor drops to ~25 %. Conversely, the TAD Al NiO devices (**Figure 6.4 C, D**) show an approximately constant fill factor of 39.7 % to ~ 33 % upon increasing $[I_2]_{eq}$. Most notably in the TAD Al NiO devices, the J_{SC} increases by an order of magnitude from 0.09 mA/cm² to 0.66 - 0.82 mA/cm² upon increasing the $[I_2]_{eq}$. There is a decrease in the V_{OC} in TAD Al NiO, upon increasing the $[I_2]_{eq}$, although it is likely due to the positive shift the Nernst potential towards the valence band edge and possibly exacerbated by some recombination mechanism that also slightly lowers the fill factor. Overall, the PCE increases 3.8 – 4.2x upon increasing $[I_2]_{eq}$, mostly due to the increase in J_{SC} . We note that the TAD Al NiO performance is lower than that previously reported, but is mostly due to the use of a different electrolyte and the deposition of 5 cycles.⁵⁴

Table 6.3: Average NiO p-DSSC device performance metrics

| | Standard | High $[I_2]_{eq}$ | Aqueous |
|---|--------------|-------------------|-------------|
| J_{sc} (no dye) (mA/cm ²) | 0.04 ± 0.006 | 0.84 ± 0.10 | 0.45 ± 0.06 |
| J_{sc} (mA/cm ²) | 1.65 ± 0.22 | 0.99 ± 0.58 | 0.90 ± 0.14 |
| V_{oc} (mV) | 85 ± 7 | 31 ± 5 | 18 ± 2 |
| FF (%) | 31.9 ± 0.6 | 25.6 ± 0.3 | 25.1 ± 0.1 |
| PCE x 10 ⁻² (%) | 4.42 ± 0.49 | 0.79 ± 0.52 | 0.41 ± 0.07 |
| R_{sh} ($\Omega \cdot cm^2$) | 86 ± 19 | 46 ± 32 | 21 ± 4 |
| R_s ($\Omega \cdot cm^2$) | 33 ± 5 | 43 ± 31 | 20 ± 4 |

Table 6.4: Average TAD Al NiO p-DSSC device performance metrics

| | Standard | High $[I_2]_{eq}$ | Aqueous |
|---|------------------|-------------------|-----------------|
| J_{sc} (no dye) (mA/cm ²) | 0.04 ± 0.006 | 0.84 ± 0.10 | 0.45 ± 0.06 |
| J_{sc} (mA/cm ²) | 0.09 ± 0.03 | 0.66 ± 0.04 | 0.82 ± 0.18 |
| V_{oc} (mV) | 186 ± 9 | 128 ± 19 | 95 ± 5 |
| FF (%) | 39.7 ± 1.5 | 33.2 ± 3.4 | 33.0 ± 0.7 |
| PCE x 10 ⁻² (%) | 0.67 ± 0.24 | 2.83 ± 0.74 | 2.57 ± 0.57 |
| R_{sh} ($\Omega \cdot cm^2$) | 6170 ± 1049 | 387 ± 132 | 235 ± 67 |
| R_s ($\Omega \cdot cm^2$) | 837 ± 268 | 110 ± 10 | 70 ± 13 |

IPCE spectra of TAD Al NiO in each electrolyte was measured. The increase in photocurrent results from a 4.7% - 8.7x increase in the chromophore IPCE when increasing the $[I_2]_{eq}$ (**Figure 6.5 A**). The impact of electrolyte injection on the JSC was further investigated by fabricating devices without any loaded chromophore and measuring the resulting J - V and IPCE curves (**Figure 6.6**). The electrolyte contribution to the IPCE increased 3-7x upon increasing the $[I_2]_{eq}$ where it is estimated that the increase in chromophore injection made up ~35 % of the total increase in J_{sc} for TAD Al NiO. This increase in both the chromophore and electrolyte injection is much larger than was seen in the PbTiO₃ devices, likely due to the available states for efficient injection in TAD Al NiO.

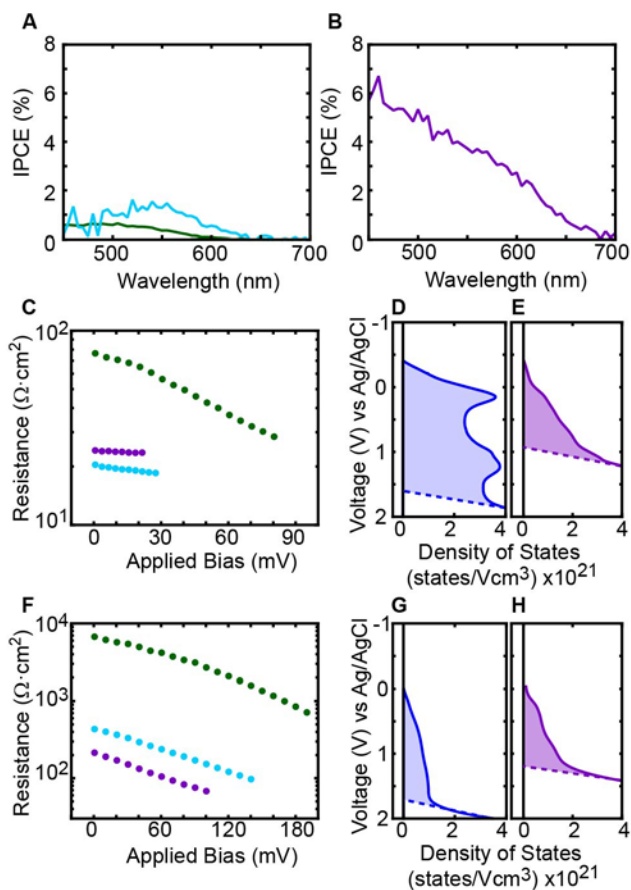


Figure 6.5. IPCE spectra of an average TAD Al NiO device with an **A**) standard (green), high $[I_2]_{eq}$ (blue), and **B**) aqueous (purple) electrolyte. The IPCE spectra is obtained by measuring the IPCE of a device with and without PI and subtracting the contribution from the electrolyte. **C**) Device resistance (circles) of an average NiO device with a standard (green), high $[I_2]_{eq}$ (blue), and aqueous (purple) electrolyte. Density of states of NiO in **D**) MeCN and **E**) H_2O where the dashed line is an approximation of the valence band edge and the shaded area denotes the trap state density. **F**) Device resistance (circles) of an average TAD Al NiO device with a standard (green), high $[I_2]_{eq}$ (blue), and aqueous (purple) electrolyte. Density of states of TAD Al NiO in **D**) MeCN and **E**) H_2O where the dashed line is an approximation of the valence band edge and the shaded area denotes the trap state density.

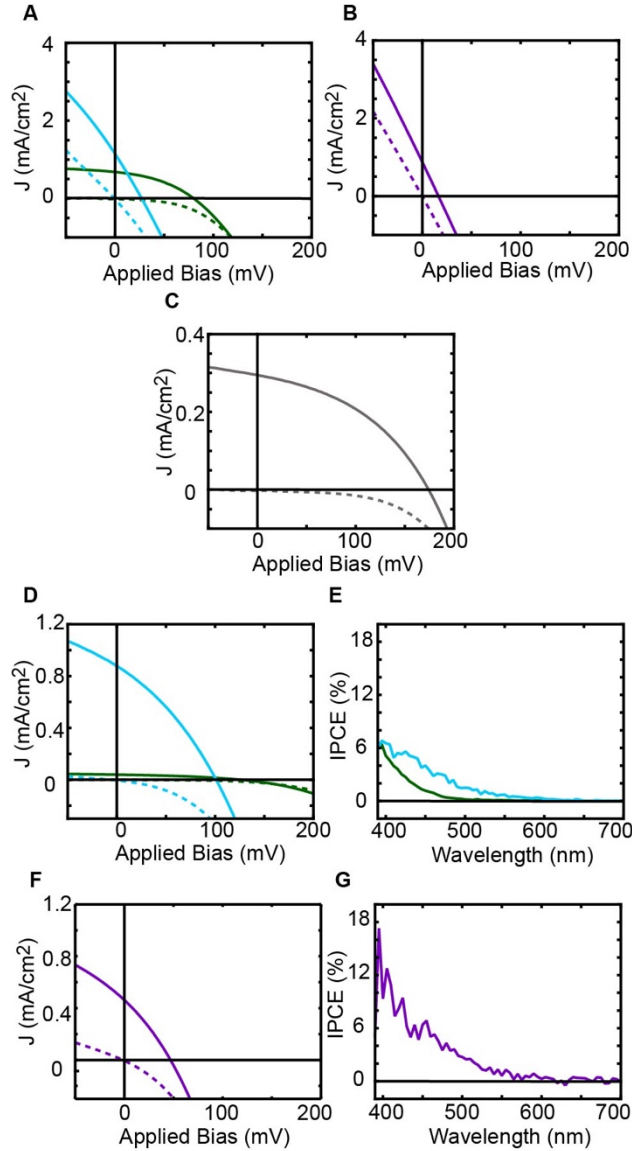


Figure 6.6: Average p-DSSCs fabricated without any chromophore. **A, B**) NiO J - V curves. **C**) TAD Al NiO with 1 cycle J - V curve in Z960 electrolyte **D, F**) TAD Al NiO J - V curves and **E, G**) TAD Al NiO IPCE curves. All J - V curves were taken under one-sun illumination (solid) and in the dark (dashed). All devices were made using either a standard (green), high $[I_2]_{eq}$ (blue), and aqueous (purple) electrolyte, except for the specific Z960 electrolyte (grey).

The changes in R_{sh} and R_s for both NiO and TAD Al NiO were calculated to aid in understanding both their impact on any fill factor changes and also to understand the semiconductor dependent change in device performance. In the high $[I_2]_{eq}$ and aqueous electrolytes both NiO and TAD Al NiO have a low R_s , similar to $PbTiO_3$. However, unlike

PbTiO₃, in either electrolyte with an increased [I₂]_{eq} R_{sh} is significantly lower at 387-234 Ω·cm² for TAD Al NiO and 46 - 20 Ω·cm² for NiO. There is a significant change in R_{sh} upon the increase of [I₂]_{eq} for TAD Al NiO and to a lesser extent, NiO, suggesting that there are specific I₂-photocathode recombination pathways present. Additionally, the improvement in β observed for PbTiO₃ p-DSSCs is not consistent with the NiO or TAD Al NiO systems. Upon increasing [I₂]_{eq} β decreased from 0.33 to 0.09 for NiO and stays approximately constant at ~0.29 for TAD Al NiO, which is similar to the trend in fill factor. There is minimal change in the trap DOS in either photocathode upon switching solvents (**Figure 6.5 D, E, G, H**).

Although there are significant differences in p-DSSC performance for each photocathode, in each photocathode system the R_s decreased to a similar value upon increasing the [I₂]_{eq}. This suggests that the electrolyte consistently affects the R_s, regardless of the photocathode system. The differences in R_{sh} and β for each photocathode suggest that each photocathode system can have unique interactions with the electrolyte that can increase the likelihood of recombination. The photocathode dependent differences in R_{sh} and β likely stem from the disparities in trap state density since, by definition, R_{sh} is the resistance to alternate pathways through the device. Upon increasing the [I₂]_{eq}, NiO has the lowest R_{sh} and has the largest trap state density of ~4 x 10²¹ states/cm³ whereas PbTiO₃ has the highest R_{sh} and the lowest trap state density of 3.26 x 10²⁰ states/cm³. TAD Al NiO has an intermediate trap state density of 1.54 x 10²¹ states/cm³ and similarly has an intermediate R_{sh}, although it is closer to that of NiO because the trap state density is closer to that of NiO. This similarly explains the disparities in fill factor and in turn the PCE.

6.4 Conclusion

p-DSSCs PCEs have long trailed those of n-DSSCs likely due to, in part, a low efficiency electrolyte. By determining that I_2 is a potent electron scavenger, and increasing the $[I_2]_{eq}$ in the electrolyte, the PCE increased 4-16x, depending on the photocathode used. This improvement in PCE was driven by an increase in both the J_{SC} and fill factor which can be explained by a decrease in R_s , or more specifically R_{CT} . An increase in $[I_2]_{eq}$ decreased the resistance of electron transfer from the excited state chromophore to the electrolyte, which increased the efficiency of chromophore regeneration and minimized the potency of alternate recombination pathways. However, simply increasing the concentration of the electron scavenger in the electrolyte does not guarantee an increase in overall PCE. The density of trap states of the photocathode significantly affects device performance, where a high trap state density will decrease R_{sh} .

We have demonstrated that tuning the electrolyte is a simple and effectively way to increase performance improvement and we expect that this is applicable to any photocathode system. Separating out the effects of the semiconductor and the electrolyte on device performance to specific device parameters (R_{sh} and R_s) will aid in understanding the cause of device performance in future studies. Further studies into the electrolyte for p-DSSCs are likely to continue to increase PCE. For example, these findings, and the importance of a high concentration of electron scavenger, likely can aid in understanding the mechanism behind the high performance of p-DSSCs using a Co or Fe based electrolyte.

6.5 Acknowledgements

T.M., S.M.M, A.D.T., R.L. and J.F.C. acknowledge support from the UNC Energy Frontier Research Center (EFRC) “Center for Solar Fuels,” an EFRC funded by the U.S.

Department of Energy, Office of Science, Office of Basic Energy Sciences, under Award DE-SC0001011.

Chapter 8: CONCLUSIONS

To combat the increased energy usage, electricity must be used efficiently and made from sustainable resources, different approaches are required. Here, thermochromic windows and p-type dye sensitized solar cells are investigated as potential technologies for increased energy sustainability. Although these approaches seem different, the same overarching viewpoint can be used to efficiently combat both issues. By focusing on the local environment of the relevant metal oxide, improvements in device efficiency were achieved as well as a better understanding of the fundamental metal oxide properties for the given application.

By taking advantage of the tunability of plasmon resonance of the metallic phase of vanadium dioxide, through either nanoparticle size or the refractive index of the surrounding matrix, we calculate that fabricating VO₂ nanoparticle-polymer composite thermochromic films has the potential to reach 50 % IR mod and 50 % visible transmittance. Experimentally, performances were ranged from an 0.97 % IR modulation at 85.8% visible transmittance to an 11.9 % IR modulation at 50.7 % visible transmittance by tuning the film thickness.

By focusing on the electrochemical environment of the metal oxide photocathode for p-type dye sensitized solar cells, a detailed understanding of the trap state density in NiO was determined. In NiO there is ~1.5 V of trap states, where the trap states exclusively control charge injection, transport and recombination. Utilizing the semiconductor-electrolyte interface in conjunction with a material informatics approach, the novel photocathode PbTiO₃ was identified and experimentally tested, where in an aqueous electrolyte achieved record p-DSSC fill factors

of 48%. Finally, by focusing on the recombination kinetics at the semiconductor electrolyte interface, the electrolyte was redesigned to increase the concentration of the electron scavenger, I_2 . By increasing the equilibrium concentration of I_2 by four orders of magnitude, the fill factor and photocurrent approximately doubled, causing the overall power conversion efficiency to increase by nearly four times. Continued emphasis on the local environment, specifically in the p-DSSC field is likely to lead to significant breakthroughs in understanding of device performance, recombination pathways and in turn, the efficiency.

This work suggests that more in depth studies into the effect of the electrolyte on p-DSSC performance is integral to understanding both the current poor device performance and how to improve the PCE. This includes, but is not limited to, the effect of the cation on device performance and the design and implementation of p-DSSC specific additives. Through these studies, using an ideal like photocathode, it is estimated that p-DSSCs can reach an equivalent PCE to that of their n-DSSC counterparts, allowing for the tandem solar fuel devices such as the DSPEC to be realized.

APPENDIX

Table 0.1. Top materials retrieved by the similarity search screening

| | | | | | | | | | |
|------------------------------------|-------|-------|------|-------|--------------|-------|------|---|---|
| Al1B1O4Pb1 ICSD_98572 | -4.36 | 0.66 | 5.02 | -7.18 | orthorhombic | Co3O4 | 0.71 | 0 | 0 |
| Al1Cu1O2 ICSD_188313 | -5.75 | -2.11 | 3.65 | -6.07 | rhombohedral | NiO | 0.52 | 0 | 0 |
| Al1O4Ta1 ICSD_67676 | -3.77 | 1.85 | 5.63 | -8.57 | orthorhombic | Co3O4 | 0.74 | 1 | 0 |
| Al2Co1O4 ICSD_290133 | -4.55 | 1.7 | 6.26 | -7.08 | cubic | Co3O4 | 0.75 | 0 | 0 |
| Al4B2Co1O10 ICSD_1975 | -5.4 | 0.54 | 5.94 | -7.49 | monoclinic | Co3O4 | 0.71 | 0 | 1 |
| As1Bi1O5Pb1 ICSD_419124 | -3.72 | 0.35 | 4.07 | -5.94 | monoclinic | Co3O4 | 0.73 | 0 | 0 |
| B2Cu1O6Pb2 ICSD_155317 | -3.73 | -0.62 | 3.11 | -6.49 | monoclinic | Co3O4 | 0.75 | 0 | 0 |
| B2Ni1O4 ICSD_418385 | -4.48 | 0.8 | 5.28 | -7.19 | monoclinic | Co3O4 | 0.76 | 0 | 0 |
| B4Fe1O7 ICSD_420401 | -4.92 | 0.67 | 5.59 | -7.84 | orthorhombic | Co3O4 | 0.77 | 0 | 0 |
| B4Ni1O7 ICSD_391407 | -4.55 | 0.34 | 4.89 | -7.54 | orthorhombic | Co3O4 | 0.85 | 0 | 0 |
| Bi1C12Cu1S1 ICSD_413289 | -4.57 | -2.41 | 2.16 | -3.44 | orthorhombic | Cu2O | 0.71 | 0 | 0 |
| Bi2Hg1S4 ICSD_14189 | -3.58 | -0.94 | 2.64 | -3.86 | monoclinic | Co3O4 | 0.75 | 1 | 0 |
| Bi2Nb2O9Pb1 ICSD_20668 | -4.51 | -1.53 | 2.97 | -7.26 | orthorhombic | Cu2O | 0.75 | 0 | 0 |
| Bi2O6W1 ICSD_23584 | -4.15 | -0.43 | 3.72 | -7.09 | orthorhombic | Co3O4 | 0.71 | 1 | 0 |
| Ca1O8Te3 ICSD_100661 | -4.46 | -0.79 | 3.68 | -5.69 | monoclinic | Co3O4 | 0.7 | 0 | 0 |
| Cl1Cu1 ICSD_78273 | -4.52 | -1.99 | 2.53 | -2.43 | cubic | NiO | 0.6 | 0 | 1 |
| Cl1Cu3S3Te1 ICSD_85789 | -4.25 | -1.94 | 2.32 | -3.27 | rhombohedral | Cu2O | 0.82 | 0 | 0 |
| Cl1O2Pb1Sb1 ICSD_86229 | -4.52 | -0.94 | 3.59 | -5.23 | orthorhombic | Cu2O | 0.72 | 0 | 0 |
| Cl1Rh1Te1 ICSD_405714 | -3.61 | -0.95 | 2.66 | -3.64 | monoclinic | Cu2O | 0.72 | 1 | 0 |
| Co1O3Te1 ICSD_500 | -5.12 | -0.68 | 4.44 | -5.58 | orthorhombic | Co3O4 | 0.75 | 0 | 1 |
| Co1O4U1 ICSD_26939 | -3.89 | 0.19 | 4.09 | -7.77 | orthorhombic | Co3O4 | 0.73 | 1 | 0 |

| | | | | | | | | | |
|--|-------|-------|------|-------|--------------|-------|------|---|---|
| Co2O4Si1 ICSD_859 | -4.16 | -1.32 | 2.85 | -6.71 | cubic | Co3O4 | 0.8 | 0 | 1 |
| Cr1Cu1O2 ICSD_402289 | -3.72 | -0.57 | 3.15 | -6.41 | hexagonal | Cu2O | 0.77 | 0 | 0 |
| Cr2Ni1O4 ICSD_280062 | -3.71 | -0.26 | 3.45 | -7.12 | tetragonal | Co3O4 | 0.77 | 0 | 1 |
| Cr2O6Te1 ICSD_24794 | -4.59 | -1.93 | 2.66 | -6.91 | tetragonal | Co3O4 | 0.81 | 0 | 0 |
| Cu1Hf1S3Ti1 ICSD_82562 | -4.61 | -2.37 | 2.24 | -5.5 | orthorhombic | Co3O4 | 0.71 | 1 | 0 |
| Cu1Nb1O3 ICSD_201899 | -3.63 | -0.73 | 2.9 | -7.16 | monoclinic | Co3O4 | 0.73 | 1 | 1 |
| Cu2Fe1Ge1S4 ICSD_47165 | -4.31 | -2.2 | 2.11 | -4.34 | tetragonal | Cu2O | 0.7 | 0 | 0 |
| Cu2Fe1S4Si1 ICSD_627355 | -4.37 | -1.49 | 2.89 | -4.56 | orthorhombic | Co3O4 | 0.72 | 0 | 0 |
| Cu2O2Pb1 ICSD_400657 | -4.49 | -2.41 | 2.08 | -4.36 | monoclinic | Cu2O | 0.72 | 0 | 0 |
| Cu4S4Ti1 ICSD_82558 | -4.03 | -0.82 | 3.21 | -3.99 | tetragonal | Cu2O | 0.72 | 0 | 0 |
| FIIn1O1 ICSD_2521 | -3.85 | -0.91 | 2.94 | -5.22 | orthorhombic | Cu2O | 0.78 | 0 | 0 |
| Fe1Nb1O4 ICSD_8128 | -4.04 | -0.23 | 3.82 | -7.92 | monoclinic | Co3O4 | 0.8 | 0 | 1 |
| Fe1O3Si1 ICSD_30675 | -3.63 | 0.71 | 4.34 | -7.47 | monoclinic | Co3O4 | 0.72 | 0 | 1 |
| Fe2O3 ICSD_189439 | -4.21 | -1.52 | 2.68 | -6.37 | orthorhombic | Co3O4 | 0.71 | 0 | 1 |
| Fe2O4Si1 ICSD_100552 | -4.59 | -0.46 | 4.13 | -7.26 | cubic | Co3O4 | 0.73 | 0 | 1 |
| Fe2O4Si1 ICSD_185523 | -5.37 | -0.54 | 4.82 | -6.71 | cubic | Co3O4 | 0.75 | 0 | 1 |
| Ge1Mg1O3 ICSD_160824 | -5.44 | -1.24 | 4.19 | -6.17 | orthorhombic | CuI | 0.7 | 0 | 1 |
| Ge1Mg1O3 ICSD_35534 | -3.56 | 0.79 | 4.36 | -6.32 | monoclinic | Co3O4 | 0.74 | 0 | 0 |
| Ge1Ni2O4 ICSD_69508 | -4.9 | -1.33 | 3.57 | -5.68 | cubic | Co3O4 | 0.85 | 0 | 0 |
| Ge1O5Pb3 ICSD_100275 | -3.97 | 0.04 | 4.01 | -5.82 | monoclinic | Co3O4 | 0.74 | 0 | 0 |
| In1Li1Mo3O8 ICSD_30579 | -4.53 | -1.19 | 3.33 | -7.17 | hexagonal | Co3O4 | 0.73 | 1 | 0 |
| In1Li1O2 ICSD_40665 | -3.95 | -0.31 | 3.64 | -5.38 | tetragonal | CuI | 0.76 | 1 | 0 |
| Li1O6Si2V1 ICSD_55164 | -3.64 | -0.36 | 3.28 | -7.57 | monoclinic | Co3O4 | 0.77 | 0 | 0 |
| Lu1O4V1 ICSD_162326 | -7 | -2.33 | 4.67 | -4.16 | tetragonal | Co3O4 | 0.82 | 1 | 0 |
| Lu1O4V1 ICSD_246685 | -4.33 | 1.12 | 5.44 | -6.34 | tetragonal | Co3O4 | 0.78 | 1 | 0 |

| | | | | | | | | | |
|---------------------------------------|-------|-------|------|-------|--------------|-------|------|---|---|
| Lu1O4V1 ICSD_419281 | -5.56 | -0.26 | 5.3 | -5.27 | tetragonal | Co3O4 | 0.78 | 1 | 0 |
| Lu1O4V1 ICSD_419285 | -5.6 | -0.84 | 4.77 | -5.43 | tetragonal | Co3O4 | 0.85 | 1 | 0 |
| Mg1O4Rh2 ICSD_109299 | -3.51 | 0.42 | 3.92 | -5.74 | cubic | Co3O4 | 0.73 | 1 | 0 |
| Mn1N2Si1 ICSD_172193 | -5.9 | -2.22 | 3.69 | -8.14 | orthorhombic | Co3O4 | 0.7 | 0 | 0 |
| Mn1O5Si2 ICSD_85554 | -4.88 | 0.91 | 5.79 | -7.82 | monoclinic | Cu2O | 0.75 | 0 | 0 |
| Mo1S2 ICSD_38401 | -4.69 | -2.06 | 2.62 | -6.28 | rhombohedral | NiO | 0.65 | 0 | 1 |
| Na1O2Ti1 ICSD_43439 | -4.74 | -0.96 | 3.78 | -6.64 | rhombohedral | NiO | 0.51 | 0 | 0 |
| Na1O2V1 ICSD_182323 | -4.21 | -1.6 | 2.61 | -6.71 | monoclinic | NiO | 0.54 | 0 | 1 |
| Nb2O6Sn1 ICSD_202827 | -4.63 | -0.85 | 3.78 | -8.02 | monoclinic | Co3O4 | 0.75 | 0 | 0 |
| Ni1O3Se1 ICSD_497 | -3.8 | 0.78 | 4.58 | -5.16 | orthorhombic | Co3O4 | 0.74 | 0 | 1 |
| Ni1P1S3 ICSD_602341 | -3.76 | -1.21 | 2.55 | -4.43 | monoclinic | Co3O4 | 0.71 | 0 | 0 |
| Ni2O4Si1 ICSD_100544 | -5.27 | -0.39 | 4.88 | -6.24 | cubic | Co3O4 | 0.83 | 0 | 1 |
| O2Sb1 ICSD_647389 | -5.41 | -1.95 | 3.46 | -6.05 | orthorhombic | Co3O4 | 0.75 | 0 | 0 |
| O3Pb1Ti1 ICSD_1610 | -5.02 | -1.06 | 3.96 | -7.03 | tetragonal | NiO | 0.8 | 0 | 1 |
| O4Pb3 ICSD_97282 | -4.6 | -2.28 | 2.32 | -5.44 | orthorhombic | Co3O4 | 0.77 | 0 | 1 |
| O4Sb2 ICSD_153156 | -5.57 | -2.41 | 3.16 | -6.05 | monoclinic | Cu2O | 0.72 | 0 | 1 |
| O4Sb2 ICSD_4109 | -5.54 | -2.11 | 3.44 | -6.05 | orthorhombic | Co3O4 | 0.78 | 0 | 1 |
| O5Pb2Te1 ICSD_407955 | -5.02 | -1.46 | 3.56 | -5.55 | monoclinic | Co3O4 | 0.75 | 0 | 0 |
| O6Pb1Sb2 ICSD_16852 | -4.04 | -0.46 | 3.58 | -6.07 | hexagonal | Cu2O | 0.72 | 0 | 0 |
| O6Sb2W1 ICSD_75595 | -3.67 | -0.68 | 2.99 | -7.11 | monoclinic | Co3O4 | 0.73 | 1 | 0 |
| O7Sn1Ta2 ICSD_15206 | -4.37 | -1.63 | 2.74 | -8.14 | monoclinic | Co3O4 | 0.83 | 1 | 0 |
| S2W1 ICSD_202367 | -4.93 | -2.14 | 2.78 | -7.07 | rhombohedral | NiO | 0.55 | 0 | 1 |

REFERENCES

1. International Energy Outlook 2017, <http://www.eia.gov/todayinenergy/detail.cfm?id=12251>, accessed: 10, 2017
2. Estimated U.S. Energy use in 2016, https://flowcharts.llnl.gov/content/assets/images/energy/us/Energy_US_2016.png, accessed: 10, 2017
3. Ozturk, I. Energy Dependency and Energy Security: The Role of Energy Efficiency and Renewable Energy Sources. *Int. Growth Cent.* 1–21 (2014).
4. Heating and cooling no longer majority of U.S. home energy use, <https://www.eia.gov/todayinenergy/detail.php?id=10271>, accessed: 10, 2017
5. Energy Efficient Windows, <https://energy.gov/energysaver/window-types> accessed: 10, 2017.
6. Improving the Energy Efficiency of Existing Windows accessed: <https://energy.gov/energysaver/energy-efficient-windows>, 10, 2017.
7. Granqvist, C. G. Electrochromics for smart windows: Oxide-based thin films and devices. *Thin Solid Films* **564**, 1–38 (2014).
8. Granqvist, C. G. Oxide-based chromogenic coatings and devices for energy efficient fenestration: Brief survey and update on thermochromics and electrochromics. *J. Vac. Sci. Technol. B, Nanotechnol. Microelectron. Mater. Process. Meas. Phenom.* **32**, 060801 (2014).
9. Xia, X. H. *et al.* Electrochromic properties of porous NiO thin films prepared by a chemical bath deposition. *Sol. Energy Mater. Sol. Cells* **92**, 628–633 (2008).
10. Gao, Y. *et al.* Nanoceramic VO₂ thermochromic smart glass: A review on progress in solution processing. *Nano Energy* **1**, 221–246 (2012).
11. Warwick, M. E. A. & Binions, R. Advances in thermochromic vanadium dioxide films. *J. Mater. Chem. A* **2**, 3275 (2014).
12. Long, L. & Ye, H. How to be smart and energy efficient: A general discussion on thermochromic windows. *Sci. Rep.* **4**, 6427 (2014).
13. Niklasson, G. a, Li, S.-Y. & Granqvist, C. G. Thermochromic vanadium oxide thin films: Electronic and optical properties. *J. Phys. Conf. Ser.* **559**, 012001 (2014).
14. Zhou, J. *et al.* Mg-doped VO₂ nanoparticles: hydrothermal synthesis, enhanced visible transmittance and decreased metal-insulator transition temperature. *Phys. Chem. Chem. Phys.* **15**, 7505–11 (2013).
15. Zhou, M. *et al.* Periodic porous thermochromic VO₂(M) films with enhanced visible transmittance. *Chem. Commun.* **49**, 6021–3 (2013).

16. Chen, Z. *et al.* VO₂-based double-layered films for smart windows: Optical design, all-solution preparation and improved properties. *Sol. Energy Mater. Sol. Cells* **95**, 2677–2684 (2011).
17. Cao, X. *et al.* Nanoporous thermochromic VO₂ (M) thin films: controlled porosity, largely enhanced luminous transmittance and solar modulating ability. *Langmuir* **30**, 1710–5 (2014).
18. Chen, Z. *et al.* VO₂-based double-layered films for smart windows: Optical design, all-solution preparation and improved properties. *Sol. Energy Mater. Sol. Cells* **95**, 2677–2684 (2011).
19. Gao, Y. *et al.* VO₂–Sb:SnO₂ composite thermochromic smart glass foil. *Energy Environ. Sci.* **5**, 8234 (2012).
20. Li, S.-Y., Niklasson, G. a. & Granqvist, C. G. Nanothermochromics: Calculations for VO₂ nanoparticles in dielectric hosts show much improved luminous transmittance and solar energy transmittance modulation. *J. Appl. Phys.* **108**, 063525 (2010).
21. Liu, C. *et al.* VO₂/Si-Al gel nanocomposite thermochromic smart foils: largely enhanced luminous transmittance and solar modulation. *J. Colloid Interface Sci.* **427**, 49–53 (2014).
22. Madida, I. G. *et al.* Submicronic VO₂–PVP composites coatings for smart windows applications and solar heat management. *Sol. Energy* **107**, 758–769 (2014).
23. Mlyuka, N. R., Niklasson, G. a. & Granqvist, C. G. Mg doping of thermochromic VO₂ films enhances the optical transmittance and decreases the metal-insulator transition temperature. *Appl. Phys. Lett.* **95**, 171909 (2009).
24. Qian, X. *et al.* Bioinspired multifunctional vanadium dioxide: improved thermochromism and hydrophobicity. *Langmuir* **30**, 10766–71 (2014).
25. Taylor, A. *et al.* A bioinspired solution for spectrally selective thermochromic VO₂ coated intelligent glazing. *Opt. Express* **21**, 750–764 (2013).
26. Xu, G., Jin, P., Tazawa, M. & Yoshimura, K. Tailoring of Luminous Transmittance upon Switching for Thermochromic VO₂ Films by Thickness Control. *Jpn. J. Appl. Phys.* **43**, 186–187 (2004).
27. Zhou, Y., Cai, Y., Hu, X. & Long, Y. Temperature-responsive hydrogel with ultra-large solar modulation and high luminous transmission for ‘smart window’ applications. *J. Mater. Chem. A* **2**, 13550 (2014).
28. Zhou, Y., Cai, Y., Hu, X. & Long, Y. VO₂/hydrogel hybrid nanothermochromic material with ultra-high solar modulation and luminous transmission. *J. Mater. Chem. A* **3**, 1121–1126 (2015).
29. Kang, L. *et al.* Nanoporous Thermochromic VO₂ Films with Low Optical Constants,

- Enhanced Luminous Transmittance and Thermo-chromic Properties. *ACS Appl. Mater. Interfaces* **3**, 135–138 (2011).
30. Huang, A. *et al.* Preparation of $V_xW_{1-x}O_2(M)@SiO_2$ ultrathin nanostructures with high optical performance and optimization for smart windows by etching. *J. Mater. Chem. A* **1**, 12545 (2013).
 31. Gao, Y. *et al.* Nanoceramic VO₂ thermo-chromic smart glass: A review on progress in solution processing. *Nano Energy* **1**, 221–246 (2012).
 32. Dai, L. *et al.* F-doped VO₂ nanoparticles for thermo-chromic energy-saving foils with modified color and enhanced solar-heat shielding ability. *Phys. Chem. Chem. Phys.* **15**, 11723–9 (2013).
 33. NREL Best Research-Cell Efficiencies. <https://www.nrel.gov/pv/assets/images/efficiency-chart.png>, accessed: 10, 2017.
 34. Ashford, D. L. *et al.* Molecular Chromophore – Catalyst Assemblies for Solar Fuel Applications. *Chem. Rev.* **115**, 13006–13049 (2015).
 35. Brennaman, M. K. *et al.* Finding the Way to Solar Fuels with Dye-Sensitized Photoelectrosynthesis Cells. *J. Am. Chem. Soc.* **128**, 13085–13102 (2016).
 36. Alibabaei, L. *et al.* Solar water splitting in a molecular photoelectrochemical cell. *Proc. Natl. Acad. Sci.* **110**, 20008–20013 (2013).
 37. Grätzel, M. Dye-sensitized solar cells. *J. Photochem. Photobiol. C Photochem. Rev.* **4**, 145–153 (2003).
 38. Hagfeldt, A., Boschloo, G., Sun, L., Kloo, L. & Pettersson, H. Dye-Sensitized Solar Cells. *Chem. Rev.* **110**, 6595–6663 (2010).
 39. Odobel, F. *et al.* Recent advances and future directions to optimize the performances of p-type dye-sensitized solar cells. *Coord. Chem. Rev.* **256**, 2414–2423 (2012).
 40. Odobel, F., Le Pleux, L., Pellegrin, Y. & Blart, E. New photovoltaic devices based on the sensitization of p-type semiconductors: Challenges and opportunities. *Acc. Chem. Res.* **43**, 1063–1071 (2010).
 41. O'Regan, B. & Grätzel, M. A low-cost, high-efficiency solar cell based on dye-sensitized colloidal TiO₂ films. *Nature* **353**, 737–740 (1991).
 42. He, J., Lindström, H., Hagfeldt, A. & Lindquist, S.-E. Dye-Sensitized Nanostructured p-Type Nickel Oxide Film as a Photocathode for a Solar Cell. *J. Phys. Chem. B* **103**, 8940–8943 (1999).
 43. Qin, P. *et al.* Design of an organic chromophore for P-type dye-sensitized solar cells. *J. Am. Chem. Soc.* **130**, 8570–8571 (2008).

44. Renaud, A. *et al.* CuGaO₂: a promising alternative for NiO in p-type dye solar cells. *J. Mater. Chem.* **22**, 14353 (2012).
45. Click, K. A. *et al.* A double-acceptor as a superior organic dye design for p-type DSSCs: high photocurrents and the observed light soaking effect. *Phys. Chem. Chem. Phys.* **16**, 26103–11 (2014).
46. Perera, I. R. *et al.* Application of the tris(acetylacetonato)iron(III)/(II) redox couple in p-type dye-sensitized solar cells. *Angew. Chemie - Int. Ed.* **54**, 3758–3762 (2015).
47. Sullivan, I. *et al.* Photoinjection of High Potential Holes into Cu₅Ta₁₁O₃₀ Nanoparticles by Porphyrin Dyes. *J. Phys. Chem. C* **119**, 21294–21303 (2015).
48. Jiang, T. *et al.* Copper borate as a photocathode in p-type dye-sensitized solar cells. *RSC Adv.* **6**, 1549–1553 (2016).
49. Xiong, D. *et al.* Use of delafossite oxides CuCr_{1-x}Ga_xO₂ nanocrystals in p-type dye-sensitized solar cell. *J. Alloys Compd.* **662**, 374–380 (2016).
50. Kakiage, K. *et al.* Highly-efficient dye-sensitized solar cells with collaborative sensitization by silyl-anchor and carboxy-anchor dyes. *Chem. Commun.* **51**, 15894–15897 (2015).
51. Mathew, S. *et al.* Dye-sensitized solar cells with 13% efficiency achieved through the molecular engineering of porphyrin sensitizers. *Nat. Chem.* **6**, 242–247 (2014).
52. Huang, Z. *et al.* Probing the Low Fill Factor of NiO p-Type Dye-Sensitized Solar Cells. *J. Phys. Chem. C* **116**, 26239–26246 (2012).
53. Chavillon, B. *et al.* Origin of the Black Color of NiO Used as Photocathode in p - Type Dye-Sensitized Solar Cells. *J. Phys. Chem. C* **117**, 22478–22483 (2013).
54. Flynn, C. J. *et al.* Site-Selective Passivation of Defects in NiO Solar Photocathodes by Targeted Atomic Deposition. *ACS Appl. Mater. Interfaces* **8**, 4754–4761 (2016).
55. D'Amario, L. *et al.* Chemical and Physical Reduction of High Valence Ni States in Mesoporous NiO Film for Solar Cell Application. *ACS Appl. Mater. Interfaces* **9**, 33490–33477 (2017).
56. Natu, G. *et al.* Valence band-edge engineering of nickel oxide nanoparticles via cobalt doping for application in p-type dye-sensitized solar cells. *ACS Appl. Mater. Interfaces* **4**, 5922–5929 (2012).
57. D'Amario, L., Boschloo, G., Hagfeldt, A. & Hammarström, L. Tuning of conductivity and density of states of NiO mesoporous films used in p-type DSSCs. *J. Phys. Chem. C* **118**, 19556–19564 (2014).
58. Natu, G., Huang, Z., Ji, Z. & Wu, Y. The Effect of an Atomically Deposited Layer of

- Alumina on NiO in P-type Dye-Sensitized Solar Cells. *Langmuir* **28**, 950–956 (2012).
59. Yu, M., Draskovic, T. I. & Wu, Y. Cu(I)-based delafossite compounds as photocathodes in p-type dye-sensitized solar cells. *Phys. Chem. Chem. Phys.* **16**, 5026–5033 (2014).
 60. Nikolaou, V., Charisiadis, A. & Charalambidis, G., Coutsolelos, A.G., Odobel, F. Recent advances and insights in dye-sensitized NiO photocathodes for photovoltaic devices. *J. Mater. Chem. A* **5**, 21077–21113 (2017).
 61. Ji, Z., Natu, G., Huang, Z. & Wu, Y. Linker effect in organic donor-acceptor dyes on p-type NiO dye sensitized solar cells. *Energy Environ. Sci.* **4**, 2818–2821 (2011).
 62. Click, K. A. *et al.* A double-acceptor as a superior organic dye design for p-type DSSCs : high photocurrents and the observed light soaking effect †. *Phys. Chem. Chem. Phys.* **16**, 26103–26111 (2014).
 63. Morandeira, A., Boschloo, G., Hagfeldt, A. & Hammarstro, L. Coumarin 343 - NiO Films as Nanostructured Photocathodes in Dye-Sensitized Solar Cells : Ultrafast Electron Transfer , Effect of the I³⁻ / I⁻ Redox Couple and Mechanism of Photocurrent Generation. *J. Phys. Chem. C* **112**, 9530–9537 (2008).
 64. Farnum, B. H. An Introduction to Solar Energy Conversion , Dye-Sensitized Solar Cells, and the Iodide / Triiodide Redox Mediator. (Johns Hopkins University, 2011).
 65. Redmond, G. & Fitzmaurice, D. Spectroscopic determination of flatband potentials for polycrystalline titania electrodes in nonaqueous solvents. *J. Phys. Chem.* **97**, 1426–1430 (1993).
 66. Watson, D. F. & Meyer, G. J. Cation effects in nanocrystalline solar cells. *Coord. Chem. Rev.* **248**, 1391–1406 (2004).
 67. Boschloo, G. & Hagfeldt, A. Characteristics of the Iodide / Triiodide Redox Mediator in Dye-Sensitized Solar Cells. *Acc. Chem. Res.* **42**, 1819–1826 (2009).
 68. Richards, C. E., Anderson, A. Y., Martiniani, S., Law, C. & Regan, B. C. O. The Mechanism of Iodine Reduction by TiO₂ Electrons and the Kinetics of Recombination in Dye-Sensitized Solar Cells. *J. Phys. Chem. Lett.* **3**, 1980–1984 (2012).
 69. Neale, N. R., Kopidakis, N., Lagemaat, J. Van De, Gra, M. & Frank, A. J. Effect of a Coadsorbent on the Performance of Dye-Sensitized TiO₂ Solar Cells : Shielding versus Band-Edge Movement. *J. Phys. Chem. B* **109**, 23183–23189 (2005).
 70. Jeanbourquin, X. A. *et al.* Rediscovering a Key Interface in Dye-Sensitized Solar Cells: Guanidinium and Iodine Competition for Binding Sites at the Dye/ Electrolyte Surface. *J. Am. Chem. Soc.* **136**, 7286–7294 (2014).
 71. Zou, J., Peng, Y. & Lin, H. A low-temperature synthesis of monoclinic VO₂ in an atmosphere of air. *J. Mater. Chem. A* **1**, 4250 (2013).

72. H. W. Verleur, J. A. S. Barker, C. N. Berglund, *Phys. Rev.* **1968**, 172, 788
73. I. Charamsinau, The Mie Theory Calculator, [http://lyle.smu.edu/ee/smuphotonics/Mie Theory Calculator/MieTheoryCalculator.htm](http://lyle.smu.edu/ee/smuphotonics/Mie%20Theory%20Calculator/MieTheoryCalculator.htm), accessed: 03, 2015
74. Flynn, C. J. *et al.* Hierarchically-structured NiO nanoplatelets as mesoscale p-type photocathodes for dye-sensitized solar cells. *J. Phys. Chem. C* **118**, 14177–14184 (2014).
75. Li, L. & Kanai, Y. Antiferromagnetic structures and electronic energy levels at reconstructed NiO (111) surfaces : A DFT + U study. *Phys. Rev. B* **91**, 235304 (2015).
76. Giannozzi, P. *et al.* QUANTUM ESPRESSO: a modular and open-source software project for quantum simulations of materials. *J. Phys. Condens. Matter* **21**, 395502 (2009).
77. Vanderbilt, D. Soft self-consistent pseudopotentials in a generalized eigenvalue formalism. *Phys. Rev. B* **41**, 7892–7895 (1990).
78. Monkhorst, H. J. & Pack, J. D. Special points for brillouin-zone integrations. *Phys. Rev. B* **13**, 5188–5192 (1976).
79. Anisimov, V. I., Zaanen, J. & Andersen, O. K. Band theory and Mott insulators: Hubbard U instaed of Stoner I. *Phys. Rev. B* **44**, 943–954 (1991).
80. Anisimov, V. I., Solovyev, I. V & Korotin, M. A. Density functional theory and NiO photoemission spectra. *Phys. Rev. B* **48**, 16923–16934 (1993).
81. Liechtenstein, A. I., Anisimov, V. I. & Zaanen, J. Density-functional theory and strong interactions: Orbital ordering in mott-hubbard insulators. *Phys. Rev. B* **52**, 5467–5471 (1995).
82. Cococcioni, M. & Gironcoli, S. De. Linear response approach to the calculation of the effective interaction parameters in the LDA+ U method. *Phys. Rev. B* **71**, 035105 (2005).
83. Perdew, J. P., Burke, K. & Ernzerhof, M. Generalized Gradient Approximation Made Simple. *Phys. Rev. Lett.* **77**, 3865–3868 (1996).
84. Dudarev, S. L., Botton, G. A., Savrasov, S. Y., Humphreys, C. J. & Sutton, A. P. Electron-energy-loss spectra and the structural stability of nickel oxide: an LSDA+U study. *Phys. Rev. B* **57**, 1505–1509 (1998).
85. Bengone, O., Alouani, M., Bloch, P. & Hugel, J. Implementation of the projector augmented-wave LDA+U method: Application to the electronic structure of NiO. *Phys. Rev. B* **62**, 392–401 (2000).
86. Rohrbach, A., Hafner, J. & Kresse, G. Molecular adsorption on the surface of strongly correlated transition-metal oxides : A case study for CO/NiO (100). *Phys. Rev. B* **69**, 075413 (2004).

87. Ebensperger, C. & Meyer, B. First-principles study of the reconstruction of hydroxylation of the polar NiO(111) surface. *Phys. Status Solidi B* **248**, 2229–2241 (2011).
88. Flynn, C. J. *et al.* Passivation of Nickel Vacancy Defects in Nickel Oxide Solar Cells by Targeted Atomic Deposition of Boron. *J. Phys. Chem. C* **120**, 16568–16576 (2016).
89. Zhang, W., Tang, B., Zhang, W. & Tang, B. Stability of the polar NiO (111) surface. *J. Chem. Phys.* **128**, 124703 (2008).
90. Isayev, O. *et al.* Materials Cartography: Representing and Mining Materials Space Using Structural and Electronic Fingerprints. *Chem. Mater.* **27**, 735–743 (2015).
91. Johnson, M. A. & Maggiora, G. M. *Concepts of Applications of Molecular Similarity*. (John Wiley & Sons, 1990).
92. Curtarolo, S. *et al.* AFLOWLIB.ORG: A distributed materials properties repository from high-throughput ab initio calculations. *Comput. Mater. Sci.* **58**, 227–235 (2012).
93. Balachandran, P. V. & Rajan, K. Structure Maps for A₃BO₄ apatites via data mining. *Acta Crystallogr. B* **68**, 24–33 (2012).
94. Calderon, C. E. *et al.* The AFLOW standard for high-throughput materials science calculations. *Comput. Mater. Sci.* **108**, 233–238 (2015).
95. International Energy Outlook 2013, <http://www.eia.gov/todayinenergy/detail.cfm?id=12251>, accessed: 08, 2015
96. Estimated U.S. Energy use in 2014, https://flowcharts.llnl.gov/content/assets/images/energy/us/Energy_US_2014.png, accessed: 08, 2015
97. F. J. Morin, Oxides Which Show a Metal-to-Insulator Transition at the Neel Temperature. *Phys. Rev. Lett.* **3**, 34 (1959)
98. Nag, J. & Haglund Jr, R. F. Synthesis of vanadium dioxide thin films and nanoparticles. *J. Phys. Condens. Matter* **20**, 264016 (2008).
99. Mlyuka, N. R., Niklasson, G. a. & Granqvist, C. G. Thermo-chromic multilayer films of VO₂ and TiO₂ with enhanced transmittance. *Sol. Energy Mater. Sol. Cells* **93**, 1685–1687 (2009).
100. Chen, S. *et al.* The visible transmittance and solar modulation ability of VO₂ flexible foils simultaneously improved by Ti doping: an optimization and first principle study. *Phys. Chem. Chem. Phys.* **15**, 17537–43 (2013).
101. Li, Y., Ji, S., Gao, Y., Luo, H. & Kanehira, M. Core-shell VO₂@TiO₂ nanorods that combine thermo-chromic and photocatalytic properties for application as energy-saving smart coatings. *Sci. Rep.* **3**, 1370 (2013).

102. Laaksonen, K. *et al.* Nanoparticles of TiO₂ and VO₂ in dielectric media: Conditions for low optical scattering, and comparison between effective medium and four-flux theories. *Sol. Energy Mater. Sol. Cells* **130**, 132–137 (2014).
103. Zhou, Y. *et al.* Surface plasmon resonance induced excellent solar control for VO₂@SiO₂ nanorods-based thermochromic foils. *Nanoscale* **5**, 9208–13 (2013).
104. Hulst, H. C. van de. *Light Scattering by Small Particles*. (1981).
105. Gao, Y. *et al.* Phase and shape controlled VO₂ nanostructures by antimony doping. *Energy Environ. Sci.* **5**, 8708 (2012).
106. Lopez, R., Haynes, T., Boatner, L., Feldman, L. & Haglund, R. Size effects in the structural phase transition of VO₂ nanoparticles. *Phys. Rev. B* **65**, 224113 (2002).
107. Lopez, R., Haynes, T. E., Boatner, L. a, Feldman, L. C. & Haglund, R. F. Temperature-controlled surface plasmon resonance in VO (2) nanorods. *Opt. Lett.* **27**, 1327–9 (2002).
108. Ge, D. *et al.* A robust smart window: reversibly switching from high transparency to angle-independent structural color display. *Adv. Mater.* **27**, 2489–95 (2015).
109. Hanna, M. C. & Nozik, A. J. Solar conversion efficiency of photovoltaic and photoelectrolysis cells with carrier multiplication absorbers. *J. Appl. Phys.* **100**, (2006).
110. Enright, B., Redmond, C. & Fitzmaurice, D. Spectroscopic Determination of Flatband Potentials for Polycrystalline TiO₂ Electrodes in Mixed Solvent Systems. *J. Phys. Chem.* **98**, 6195–6200 (1994).
111. Bard, A. J. & Faulkner, L. R. *Electrochemical Methods: Fundamentals and Applications*. (John Wiley & Sons, 2001).
112. Gelderman, K., Lee, L. & Donne, S. W. Flat-Band Potential of a Semiconductor: Using the Mott–Schottky Equation. *J. Chem. Educ.* **84**, 685 (2007).
113. Memming, R. *Semiconductor Electrochemistry*. (Wiley-VCH, 2015).
114. Dillon, R. J., Alibabaei, L., Meyer, T. J. & Papanikolas, J. M. Enabling Efficient Creation of Long-Lived Charge-Separation on Dye- Sensitized NiO Photocathodes. *ACS Appl. Mater. Interfaces* **9**, 26786–26796 (2017).
115. D’Amario, L., Antila, L. J., Rimgard, B. P., Boschloo, G. & Hammarstro, L. Kinetic Evidence of Two Pathways for Charge Recombination in NiO- Based Dye-Sensitized Solar Cells. *J. Phys. Chem. Lett.* **6**, 779–783 (2015).
116. Peiris, T. A. N., Sagu, J. S., Wijayantha, K. G. U. & García-Cañadas, J. Electrochemical determination of the density of states of nanostructured NiO films. *ACS Appl. Mater. Interfaces* **6**, 14988–14993 (2014).

117. Ratcliff, E. L. *et al.* Evidence for near-surface NiOOH species in solution-processed NiO x selective interlayer materials: Impact on energetics and the performance of polymer bulk heterojunction photovoltaics. *Chem. Mater.* **23**, 4988–5000 (2011).
118. Li, N. *et al.* Double-layered NiO photocathodes for p-Type DSSCs with record IPCE. *Adv. Mater.* **22**, 1759–1762 (2010).
119. Mirzayi, M. & Hekmat-Shoar, M. H. in *Solid State Electrochemistry* (ed. Willard, T. G.) 241–254 (Nova Science Publishers, 2010).
120. Nattestad, A., Ferguson, M., Kerr, R., Cheng, Y.-B. & Bach, U. Dye-sensitized nickel(II)oxide photocathodes for tandem solar cell applications. *Nanotechnology* **19**, 295304 (2008).
121. Fabregat-Santiago, F., Mora-Sero, I., Garcia-Belmonte, G. & Bisquert, J. Cyclic voltammetry studies of nanoporous semiconductors. Capacitive and reactive properties of nanocrystalline TiO₂ electrodes in aqueous electrolyte. *J. Phys. Chem. B* **107**, 758–768 (2003).
122. Mandal, D. & Hamann, T. W. Charge Distribution in Nanostructured TiO₂ Photoanode Determined by Quantitative Analysis of the Band Edge Unpinning. *ACS Appl. Mater. Interfaces* **8**, 419–424 (2016).
123. Mandal, D. & Hamann, T. W. Band energies of nanoparticle semiconductor electrodes determined by spectroelectrochemical measurements of free electrons. *Phys. Chem. Chem. Phys.* **17**, 11156–11160 (2015).
124. Kuhlbeck, H. *et al.* Molecular adsorption on oxide surfaces: Electronic structure and orientation of NO on NiO(100)/Ni(100) and NiO(100) as determined from electron spectroscopies and ab initio cluster calculations. *Phys. Rev. B* **43**, 1969–1986 (1991).
125. Wang, Y., Zhu, Q. & Zhang, H. Fabrication of β -Ni(OH)₂ and NiO Hollow Spheres by a Facile Template-free Process. *Chem. Commun.* **0**, 5231–5233 (2005).
126. Mironova-Ulmane, N. *et al.* Structural and Magnetic Properties of Nickel Oxide Nanopowders. *Solid State Phenom.* **168**, 341–344 (2011).
127. Jiao, Z., Wu, M., Qin, Z. & Xu, H. The electrochromic characteristics of sol gel-prepared NiO thin film. *Nanotechnology* **14**, 458–461 (2003).
128. Chen, M., Guyot-Sionnest, P. Reversible Electrochemistry of Mercury Chalcogenide Colloidal Quantum Dot Films. *ACS Nano* **11**, 4165–4173 (2017).
129. Park, N. G. Perovskite solar cells: An emerging photovoltaic technology. *Materials Today* **18**, 65–72 (2015).
130. Orenstein, J. Advances in the Physics of High-Temperature Superconductivity. *Science*. **288**, 468–474 (2000).

131. Donadio, S., Maffioli, S., Monciardini, P., Sosio, M. & Jabes, D. Antibiotic discovery in the twenty-first century: current trends and future perspectives. *J. Antibiot. (Tokyo)*. **63**, 423–430 (2010).
132. Walsh, A. Inorganic materials: The quest for new functionality. *Nat. Chem.* **7**, 274–275 (2015).
133. Gorse, A.-D. Diversity in medicinal chemistry space. *Curr. Top. Med. Chem.* **6**, 3–18 (2006).
134. Bajorath, J. Integration of virtual and high-throughput screening. *Nat. Rev. Drug Discov.* **1**, 882–94 (2002).
135. Kitchen, D. B., Decornez, H., Furr, J. R. & Bajorath, J. Docking and scoring in virtual screening for drug discovery: methods and applications. *Nat. Rev. Drug Discov.* **3**, 935–949 (2004).
136. Ain, Q. U., Aleksandrova, A., Roessler, F. D. & Ballester, P. J. Machine-learning scoring functions to improve structure-based binding affinity prediction and virtual screening. *Wiley Interdiscip. Rev. Comput. Mol. Sci.* **5**, 405–424 (2015).
137. Heikamp, K. & Bajorath, J. The future of virtual compound screening. *Chem. Biol. Drug Des.* **81**, 33–40 (2013).
138. Curtarolo, S. *et al.* The high-throughput highway to computational materials design. *Nat. Mater.* **12**, 191–201 (2013).
139. Hattrick-Simpers, J., Wen, C. & Lauterbach, J. The Materials Super Highway: Integrating High-Throughput Experimentation into Mapping the Catalysis Materials Genome. *Catal. Letters* **145**, 290–298 (2015).
140. Materials Genome Initiative.
141. Jain, A. *et al.* Commentary: The Materials Project: A materials genome approach to accelerating materials innovation. *APL Mater.* **1**, 011002 (2013).
142. Saal, J. E., Kirklin, S., Aykol, M., Meredig, B. & Wolverton, C. Materials Design and Discovery with High-Throughput Density Functional Theory: The Open Quantum Materials Database (OQMD). *Jom* **65**, 1501–1509 (2013).
143. Hachmann, J. *et al.* The Harvard Clean Energy Project: Large-Scale Computational Screening and Design of Organic Photovoltaics on the World Community Grid. *J. Phys. Chem. Lett.* **2**, 2241–2251 (2011).
144. Kalidindi, S. R. Data science and cyberinfrastructure: critical enablers for accelerated development of hierarchical materials. *Int. Mater. Rev.* **60**, 150–168 (2015).
145. Rajan, K. Materials Informatics: The Materials ‘Gene’ and Big Data. *Annu. Rev. Mater.*

- Res.* **45**, 153–169 (2015).
146. Hautier, G., Miglio, A., Ceder, G., Rignanese, G.-M. & Gonze, X. Identification and design principles of low hole effective mass p-type transparent conducting oxides. *Nat. Commun.* **4**, 2292 (2013).
 147. Raccuglia, P. *et al.* Machine-learning-assisted materials discovery using failed experiments. *Nature* **533**, 73–76 (2016).
 148. Snaith, H. J. Perovskites : The Emergence of a New Era for Low-Cost , High-Efficiency Solar Cells. *J. Phys. Chem. Lett* **4**, 3623–3630 (2013).
 149. Flynn, C. J. *et al.* Site-Selective Passivation of Defects in NiO Solar Photocathodes by Targeted Atomic Deposition. *ACS Appl. Mater. Interfaces* **8**, 4754–4761 (2016).
 150. McCullough, S. M., Flynn, C. J., Mercado, C. C., Nozik, A. J. & Cahoon, J. F. Compositionally-tunable mechanochemical synthesis of $Zn_xCo_{3-x}O_4$ nanoparticles for mesoporous p-type photocathodes. *J. Mater. Chem. A* **3**, 21990–21994 (2015).
 151. Sharma, G. *et al.* Electronic structure, photovoltage, and photocatalytic hydrogen evolution with p-CuBi₂O₄ nanocrystals. *J. Mater. Chem. A* (2015). doi:10.1039/C5TA07040F
 152. Bender, A. & Glen, R. C. Molecular similarity: a key technique in molecular informatics. *Org. Biomol. Chem.* **2**, 3204–18 (2004).
 153. Johnson, M. A. & Maggiora, G. M. *Concepts and Applications of Molecular Similarity*. (John Wiley & Sons, 1990).
 154. Stumpfe, D. & Bajorath, J. Similarity searching. *Wiley Interdiscip. Rev. Comput. Mol. Sci.* **1**, 260–282 (2011).
 155. Willett, P. The calculation of molecular structural similarity: Principles and practice. *Mol. Inform.* **33**, 403–413 (2014).
 156. Li, Z., Luo, W., Zhang, M., Feng, J. & Zou, Z. Photoelectrochemical cells for solar hydrogen production: current state of promising photoelectrodes, methods to improve their properties, and outlook. *Energy Environ. Sci.* **6**, 347–370 (2013).
 157. Hisatomi, T., Kubota, J. & Domen, K. Recent advances in semiconductors for photocatalytic and photoelectrochemical water splitting. *Chem. Soc. Rev.* **43**, (2014).
 158. Yang, K., Setyawan, W., Wang, S., Buongiorno Nardelli, M. & Curtarolo, S. A search model for topological insulators with high-throughput robustness descriptors. *Nat. Mater.* **11**, 614–9 (2012).
 159. Frederikse, H. P. R. Permittivity (dielectric constant) of inorganic solids. *CRC Handb. Chem. Physics, 90th Ed. (Internet Version 2010)* 12.44–12–54 (2010).

160. Saliba, M. *et al.* Cesium-containing Triple Cation Perovskite Solar Cells: Improved Stability, Reproducibility and High Efficiency. *Energy Environ. Sci.* **9**, 1989–1997 (2016).
161. Chen, F., Schafranek, R., Li, S., Wu, W. B. & Klein, a. Energy band alignment between Pb(Zr,Ti)O₃ and high and low work function conducting oxides—from hole to electron injection. *J. Phys. D. Appl. Phys.* **43**, 295301 (2010).
162. Call, R. W. *et al.* Growth and Post-Deposition Treatments of SrTiO₃ Films for Dye Sensitized Photoelectrosynthesis Cell Applications. *ACS Appl. Mater. Interfaces* **8**, 12282–12290 (2016).
163. Mansoor, M. A. *et al.* Perovskite-Structured PbTiO₃ Thin Films Grown from a Single-Source Precursor. *Inorg. Chem.* **652**, 5624–5626 (2013).
164. Bhide, V. G., Hegde, M. S. & Deshmukh, K. G. Ferroelectric Properties of Lead Titanate. *J. Am. Ceram. Soc.* **51**, 565–68 (1968).
165. Reitz, C., Leufke, P. M., Hahn, H. & Brezesinski, T. Ordered Mesoporous Thin Film Ferroelectrics of Biaxially Textured Lead Zirconate Titanate (PZT) by Chemical Solution Deposition. *Chem. Mater.* **26**, 2195–2202 (2014).
166. Varghese, J. *et al.* Fabrication of Arrays of Lead Zirconate Titanate (PZT) Nanodots via Block Copolymer Self-Assembly. *Chem. Mater.* **25**, 1458–1463 (2013).
167. Liu, W., Kong, L., Zhang, L. & Yao, X. Study of the surface layer of lead titanate thin film by X-ray diffraction. *Solid State Commun.* **93**, 653–657 (1995).
168. Qin, P. *et al.* Synthesis and Mechanistic Studies of Organic Chromophores with Different Energy Levels for p-Type Dye-Sensitized Solar Cells. *J. Phys. Chem. C* **114**, 4738–4748 (2010).
169. Won, D. II *et al.* Highly Robust Hybrid Photocatalyst for Carbon Dioxide Reduction: Tuning and Optimization of Catalytic Activities of Dye/TiO₂/Re(I) Organic-Inorganic Ternary Systems. *J. Am. Chem. Soc.* **137**, 13679–13690 (2015).
170. Bella, F. & Grätzel, M. Aqueous dye-sensitized solar cells. *Chem. Soc. Rev.* **44**, 3431–3473 (2015).
171. Law, C. *et al.* Water-based electrolytes for dye-sensitized solar cells. *Adv. Mater.* **22**, 4505–4509 (2010).
172. She, C. *et al.* pH-Dependent Electron Transfer from Re-bipyridyl Complexes to Metal Oxide Nanocrystalline Thin Films. *J. Phys. Chem. B* **109**, 19345–19355 (2005).
173. Cheng, J. *et al.* Efficient Hole Transport Layers with Widely Tunable Work Function for Deep HOMO Level Organic Solar Cells. *J. Mater. Chem. A* **3**, 23955–23963 (2015).
174. Bisquert, J. & Marcus, R. A. Device Modeling of Dye-Sensitized Solar Cells. *Top Curr.*

- Chem* **352**, 325–396 (2014).
175. Lagemaat, J. Van De, Park, N. G. & Frank, A. J. Influence of Electrical Potential Distribution, Charge Transport, and Recombination on the Photopotential and Photocurrent Conversion Efficiency of Dye-Sensitized Nanocrystalline TiO₂ Solar Cells : A Study by Electrical Impedance and Optical Modulation. *J. Phys. Chem. B* **104**, 2044–2052 (2000).
 176. Moot, T. *et al.* Material informatics driven design and experimental validation of lead titanate as an aqueous solar photocathode. *Mater. Discov.* **6**, 9–16 (2016).
 177. Wang, H. & Peter, L. M. Influence of electrolyte cations on electron transport and electron transfer in dye-sensitized solar cells. *J. Phys. Chem. C* **116**, 10468–10475 (2012).
 178. Wang, H., Bell, J., Desilvestro, J., Bertoz, M. & Evans, G. Effect of Inorganic Iodides on Performance of Dye-Sensitized Solar Cells. *J. Phys. Chem. C* **111**, 15125–15131 (2007).
 179. Nazeeruddin, M. K. *et al.* Conversion of light to electricity by cis-X₂bis(2,2'-bipyridyl-4,4'-dicarboxylate)ruthenium(II) charge-transfer sensitizers (X = Cl-, Br-, I-, CN-, and SCN-) on nanocrystalline titanium dioxide electrodes. *J. Am. Chem. Soc.* **115**, 6382–6390 (1993).